Universitat Politècnica de Catalunya
Programa de Doctorat en Anàlisi Estructural

Departament d'Enginyeria Civil i Ambiental

Numerical Modeling of the Underwater Acoustic Impact of Offshore Stations

by

Raúl Hospital-Bravo

Doctoral Thesis
Advisors: Josep Sarrate and Pedro Díez
Barcelona, May 2021

A mis padres, Andrés y Josefina, por alimentar en mí el instinto de curiosidad.
A Elisenda, por su aliento incondicional.
A Max y Gael, el futuro.

Abstract

Numerical Modeling of the Underwater Acoustic Impact of Offshore Stations

Raúl Hospital-Bravo

The design of offshore power stations (for wind, wave or tidal energy generation) requires assessing their environmental impact. In particular, it is of the major importance to predict the impact of the generated subsea noise on the marine fauna, especially sea mammals and fishes. Here, the noise propagation is modelled with the Helmholtz equation and numerically solved using a Partition of Unity Method (PUM). The aim is simulating the underwater sound propagation of multiple non-impulsive sources. The output of the simulations consists of spatial distributions of the sound pressure level.

The mathematical model at hand considers the most relevant aspects involved in environmental underwater acoustics. Specifically, Helmholtz equation allows accounting for the most important wave phenomena: absorption, interference, reflection, refraction and diffraction. For instance, the acoustic absorption produced by seawater is represented by the imaginary part of the wavenumber. In addition, a non-uniform wavenumber that depends on the salinity, temperature and depth is considered. The model is completed with a set of boundary conditions providing a specific treatment for the reflective properties of the sea bottom and surface. The input noise is also introduced as a boundary condition. Finally, Perfectly Matched Layers (PMLs) are placed at the lateral artificial boundaries of the domain to avoid spurious reflections.

The numerical strategy is based on a PUM enriched with plane waves. The plane wave functions are combined with the classical polynomial shape functions (hat functions, a partition of unity preserving the continuity of the approximation space among elements). The choice of plane waves provides two main advantages. On the one hand, since the enriching functions satisfy the governing equation and include a priori knowledge of the solution, they mitigate the pollution error that is intrinsic to the solutions obtained with standard polynomial approximations. On the other hand, they allow using coarser meshes with a larger element size. This leads to a drastic reduction in the number of degrees of freedom. Therefore, the method is well suited for solving the Helmholtz equation in large domains (from hundreds of meters to kilometers) compared to the characteristic wavelength (from centimeters

to meters).

However, since the plane waves are described by complex exponential functions, the computation of the elemental matrices entails the integral of highly-oscillatory functions. This increases the requirements involved in the integration step and makes the standard Gauss-Legendre rules lose their competitiveness. In the 2D version of the tool, we overcome this drawback by implementing an existing semi-analytical rule. In the 3D version, we develop a novel efficient rule to integrate highly oscillatory functions over tetrahedra. The integrand is expressed as the product of a non-oscillatory part and a complex exponential function. The rule is designed to be exact, except round-off errors, for integrals with a polynomial non-oscillatory part, which is the case of the Helmholtz equation solved with the PUM enriched with plane waves.

To conclude, we present several examples that assess and illustrate the capabilities of the tool, including sea water absorption, homogeneous or heterogeneous media, seabeds with non-uniform transmission coefficient, and single or multiple sources.

Acknowledgments

This work is partially supported by KIC InnoEnergy and European Institute of Innovation and Technology (EIT) through project Offshore Test Station (OTS; 03_2011_LH03 Industry Energy Efficiency).

This thesis would not have been possible without the contribution of many colleagues from LaCàN that delivered extremely interesting ideas and learning, and, especially, without the endeavor of my advisors.

Contents

List of Figures

List of Tables

Chapter 1

Introduction

1.1 Motivation

In order to reduce greenhouse gas emissions and to achieve the goals of the Kyoto Protocol Protocol (1997), there has been a global effort to invest in new and less polluting sources of energy. This has been reflected in the implementation of legislation to promote renewable energy, namely the Renewable Energy Directive 2009/28/EC in Europe The European Commission (2009), and the Energy Policy Act of 2005 in the USA United States Congress (2005). A part of the investment motivated by this new framework corresponds to research in offshore marine renewable energies and its implementation, as they benefit from the constant resource availability and low spatial constraints, when compared with inland harnessing. Since strong winds regularly blow over the open ocean, new offshore designs for deeper waters have to be considered.

These trends raise concern about the impact of engineering projects on the marine environment. For instance, one factor of concern is related to the potential impact of man-made noise on the aquatic biota. The acoustic pollution due to anthropogenic activities in the oceans, such as seismic exploration, military sonar operation, commercial shipping, construction, oil and gas extraction, and offshore energy generation, has a direct impact on marine ecosystems. Until recent decades, there was a lack of knowledge on the environmental impact of the underwater noise Williams et al. (2015), and even nowadays special efforts are focused on monitoring the underwater noise levels Nedwell et al. (2003); Ainslie et al. (2009), identifying and characterizing

the effects of noise on marine endangered species Thomsen et al. (2006); Thomsen (2009), and establishing quantitative criteria to assess this impact The European Commission (2010).

From a biological point of view, the presence of artificial subsea noise is particularly relevant for the marine animals that rely on sound detection to survive, especially the marine mammals. For instance, a high level of exposure produces behavioral changes, masking of sounds of interest, hearing losses, and temporary or permanent injuries over the marine fauna. Furthermore, low frequency sound can travel large distances due to the acoustic propagation properties of water, thus escalating the impact zone. As a consequence, a massive increase in the number of noise sources at low frequency has the potential to significantly change the soundscape of the ocean with negative consequences.

This growing concern is reflected in several national and international agreements and regulations. Three remarkable examples are: the Marine Mammals Protection Act of 1972 in the United States Marine Mammal Commission (2007), the OSPAR Convention in the North-East Atlantic OSPAR Commission and others (2005), and the Marine Strategy Framework Directive 2008/56/EC (MSFD) in the European Union The European Commission (2008). These regulations clearly identify anthropogenic noise as a specific type of pollution, and state that special attention must be focused on limiting its environmental impact on marine life. In particular, Descriptor 11 from the European Union Commission Decision 2010/477/EU The European Commission (2010) sets as a first priority the assessment and monitoring of underwater noise with frequencies ranging from 10 Hz to 10 kHz.

At present, many offshore players and developers, from different backgrounds and fields, are grappling with the current and upcoming legislation that requires an acoustic assessment of their activities. No matter the specific field of application (installation noises from piling at coastal constructions, the operation of offshore energy stations, sea shipping, etc.) the impact of any temporary or permanent noise source is becoming a major factor to determine its sustainability and environmental impact. The impact is particularly relevant if the noise occurs within a long time span (years in offshore energy deployments). In this case, the amount of potential damage is larger and can affect the sea ecosystem permanently.

In this context, the European Institute of Innovation & Technology (EIT) drove the creation of a Knowledge & Innovation Community, KIC InnoEnergy, an alliance

of players from education, research and industry involved in the sustainable energy sector. KIC InnoEnergy promoted a portfolio of projects, among which the Offshore Test Station (OTS). This project developed several products in the context of offshore power plants. One of these products comprises two tools for monitoring, assessing and predicting the acoustic impact of the stations.

On the one hand, the monitoring tool consists of a buoy carrying hydrophones and other environmental sensors, and a system of wireless data communication between the buoy and mainland, providing a near real-time data flow. The buoy design focuses on maximizing the autonomy of the tool, improving the reliability of the data stream and generating the information needed to optimize the frequency and success of maintenance operations at the energy station, therefore reducing the overall cost. The acoustic data can also be used to detect anomalies in the mechanical components of the energy devices, for example wind turbines in a wind farm, by identifying deviations in their acoustic signature.

On the other hand, the acoustic modeling tool consists of a numerical model for underwater noise propagation. The model generates 3D sound intensity maps of the region of interest, which provide crucial a priori knowledge for the elaboration of acoustic impact assessments Dekeling et al. (2013). This knowledge is of the major importance at the draft design phase of an offshore station, and contributes to the acoustic section of the Environmental Impact Assessment (EIA).

The development of the modeling tool required a considerable amount of scientific research, which motivated and fed the present thesis.

1.2 Goals and outline

The main goal of this work is to develop a 3D numerical tool for the simulation of underwater noise propagation generated by multiple non-impulsive sources. In particular, the tool has to perform in the context of the environmental impact of offshore stations on the marine fauna. That is, the outputs of the tool will be used to assess the potential disturbance to the marine fauna. Therefore, we pursue the following range of applicability: large domains (from hundreds of meters to several kilometers) and medium to high frequencies (from dozens of Hz to a few kHz).

Assuming time-harmonic behavior, methods based on the Helmholtz equation and derived formulations have been extensively used to model non-impulsive underwater

sound propagation Pierce (1965); Tappert (1977); Burdic (1983); Ihlenburg (1998). This equation allows including the most relevant wave phenomena into the model: absorption, interference, reflection, refraction and diffraction.

The Partition of the Unity Method (PUM) enriched with plane waves is especially suited to solve the Helmholtz equation. The introduction of plane waves in the basis of the approximation space takes into account a priori knowledge about the solution. This enables using coarser meshes and, therefore, reducing the computational cost. In addition, the pollution error is mitigated, increasing the accuracy of the simulations Melenk (1995); Melenk and Babuška (1996); Babuška and Melenk (1997); Mayer and Mandel (1997); Laghrouche and Bettess (2000); Ortiz and Sanchez (2001); Laghrouche et al. (2002, 2003); Bettess et al. (2003); Sugimoto et al. (2003); Perrey-Debain et al. (2004); Ortiz (2004); Laghrouche et al. (2005); Strouboulis and Hidajat (2006); Wang et al. (2012); Yang et al. (2018).

To fully exploit the advantages of the PUM, the characteristic length of the domain has to be significantly longer than the sound wavelength. Note that this is the case of off-shore wind farms or power stations, that are usually installed over smooth seabeds. It is important to point out that the range of applicability of the method greatly exceeds the marine environmental framework. However, the tool developed in this thesis focuses on this application.

In order to achieve the main target of this thesis, three partial goals have been considered:

- **Developing a 2D version of the tool for the simulation of undersea acoustic propagation**. Before addressing this goal, the most relevant aspects involved in the environmental underwater acoustics are collected in Chapter 2, including a description of the noise at the sea, a brief characterization of the most typical anthropogenic noise inputs, the subsequent environmental impact on marine fauna, and the agreements and regulations created by international organizations and administrations in order to limit noise pollution. Afterwards, Chapter 3 reviews several techniques currently available for simulating underwater noise propagation. From this analysis, we conclude that the Partition of Unity Method (PUM) is well suited for computing the acoustic impact on large domains when medium and high frequencies are considered. Finally, Chapter 4 presents how to incorporate the most relevant physical aspects of the subsea noise propagation into a 2D model, and details a numerical procedure to solve

the problem by means of the PUM enriched with plane waves.

- **Developing an efficient rule to integrate highly oscillatory functions over tetrahedra**. The PUM enriched with plane waves leads to the integration of highly oscillatory functions in order to obtain the coefficients of the finite element system matrix. This makes the standard Gauss-Legendre quadratures lose their competitiveness, especially in the 3D case. Thus, it is mandatory to develop specific and efficient quadratures for integrating this type of functions over 3D elements. Bettess et al. (2003) developed 2D semi-analytical integration rules for triangles and quadrilaterals. In Chapter 5, a similar approach is extended to 3D problems leading to a novel semi-analytical rule. In addition, we include implementation details and several numerical examples to assess the accuracy and computational efficiency of the proposed integration method, compared to high-order Gauss-Legendre quadratures.

- **Developing a 3D version of the tool for the simulation of undersea acoustic propagation**. Based on the 2D model and using the 3D semi-analytical rule, Chapter 6 presents the 3D underwater noise propagation model. It also details the two basic ingredients of the 3D tool: the distribution of the plane wave directions and the analytical expression of the coefficients of the resulting linear system of equations. Finally, it presents several examples that illustrate the capabilities and benefits of the developed tool.

Chapter 2

Overview of environmental underwater acoustics

This chapter outlines the main physical and environmental features that are relevant for the development of an underwater noise propagation simulation tool. The chapter is divided into four sections. Section 2.1 presents basic concepts on underwater acoustics. Section 2.2 characterizes the typology of anthropogenic noise sources, while Section 2.3 details the vulnerability of the marine fauna associated to underwater noise. Finally, Section 2.4 collects specific references to noise pollution included in current regulatory legislation, and international agreements regarding the protection of marine environments.

2.1 Basic concepts on underwater acoustics

Underwater sound propagation presents some particularities compared to the propagation through air. Sound speed is almost 5 times higher, making wavelengths be considerably longer for equivalent frequency levels. As a consequence, seawater is an efficient medium for sound propagation and, therefore, a noisy environment too, especially when uncontrolled anthropogenic sources are present.

The reader is referred to references Urick (1983); Burdic (1983) and (Kinsler et al., 1999, Chapter 15) for details of the underlying physics of the underwater acoustic propagation.

2.1.1 Sound measure

Sound propagates through mechanical waves generated by the vibration of the molecules. These waves produce oscillations in the static pressure field. Herein, *pressure*, p, refers to the deviation of the total pressure, p_{total}, from the hydrostatic pressure, p_{h},

$$p_{\text{total}} = p_{\text{h}} + p \ .$$

Sound pressure varies in several orders of magnitude and is frequently quantified using the sound pressure level (SPL), which is a logarithmic scale referenced to a standard value,

$$\text{SPL} = 10 \cdot \log_{10}\left(\frac{p_{\text{rms}}^2}{p_0^2}\right) = 20 \cdot \log_{10}\left(\frac{p_{\text{rms}}}{p_0}\right) \ , \tag{2.1}$$

where SPL is measured in decibels related to p_0 (dB re p_0), p_0 is the standard reference pressure (1 μPa in water, by convention), and p_{rms} is the time-averaged root mean square pressure at a certain point and during a period of time T_t,

$$p_{\text{rms}} = \sqrt{< p^2 >} = \sqrt{\frac{1}{T_t}\int_0^T p^2(t)\,\mathrm{d}t} \ ,$$

where the notation $< p^2 >$ is introduced to denote the time-average of p^2.

In the case of harmonic waves, $p_{\text{rms}} = p_{\text{max}}/\sqrt{2}$, where p_{max} is the maximum value of the sinusoidal pressure p.

To avoid confusion, it is important to point out that in air acoustics the reference pressure value is $p_0 = 20$ μPa. This difference produces a SPL 26.02 dB higher in water than in air, for the same value of pressure.

When the SPL is used to characterize the noise produced by a single point source, the distance from the point of interest to the source has to be referred.

The sound intensity I (typically in W/m^2) is the acoustic power (average rate of energy flow) per unit of area and is given by

$$I = \frac{< p^2 >}{Z} = \frac{< p^2 >}{\rho \cdot c} \ ,$$

where Z is the acoustic impedance, ρ is the density ($\rho = 1025$ kg/m^3 in average for seawater) and c is the sound speed.

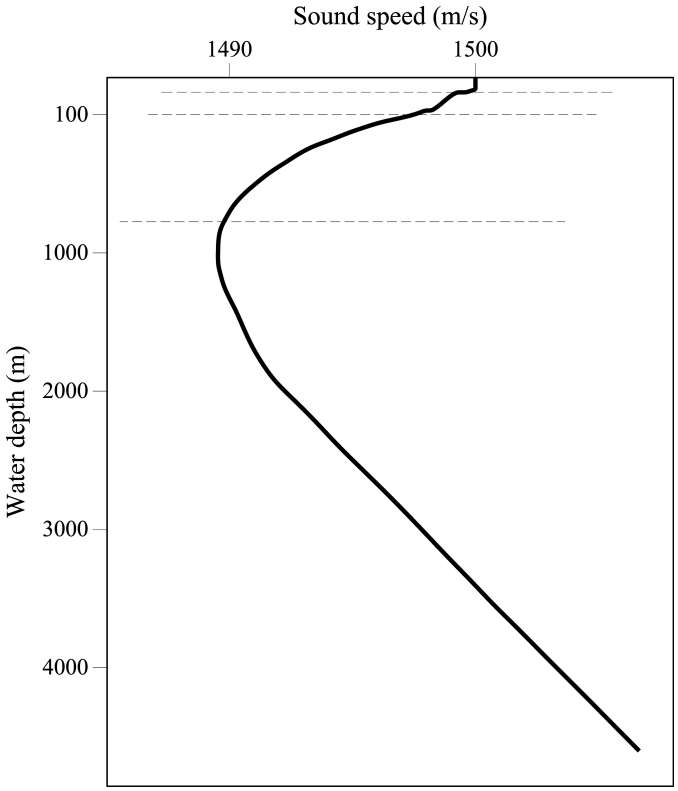

Figure 2.1: Typical vertical profile of the sound speed against water depth.

2.1.2 Speed of sound in seawater

The sound speed c is the fundamental physical parameter for the sound propagation. It determines the wavelength ($\lambda = 2\pi f/c$), where f is the wave frequency. The spatial variations of c produce the refraction and reflection phenomena. In the particular case of seawater, c depends on temperature, salinity and hydrostatic pressure. These magnitudes are generally horizontally stratified, except in areas located near river mouths or suffering intense ice melting, and they are well described by means of vertical profiles, see Figure 2.1 as an example. If the vertical gradient is strong enough, internal reflection and refraction effects can appear, see Section 2.1.3.

The sound speed reaches a local minimum at a depth of 800∼1000 meters. This local minimum, called *deep sound channel* or SOFAR channel, acts as a waveguide, as sound tends to bend towards it (ducting effect). The SOFAR channel is able to propagate low frequency sounds up to thousands of kilometers and it is interesting from the point of view of submarine warfare, more than from an environmental point of view.

The model presented in this thesis dissertation considers non-uniform sound speed distributions, although from a practical point of view, it is very common to consider vertically stratified sound speed profiles. The sound speed is estimated thanks to the UNESCO equation Wong and Zhu (1995), which is a standard based on the work proposed by Chen and Millero (1977). The hydrostatic pressure is estimated by following the corresponding equation in Leroy and Parthiot (1998), see Appendix A.

If the required salinity, temperature or depth data are not available, **a standard sound speed of 1512.8 m/s can be considered by default**. This value corresponds to the sound speed at the sea surface with seawater at 17°C and containing a salinity of 35 ppt (most common seawater conditions in practice). In the particular case of uniform sound speed, the model includes computational shortcuts and optimizations in order to increase its performance.

2.1.3 Physical phenomena related to underwater acoustics

Sound propagates through mechanical pressure waves and, therefore, it is subjected to wave theory and affected by the following wave phenomena: absorption, interference, reflection, refraction and diffraction. All of them are considered by the simulation tool.

2.1.3.1 Seawater absorption

Empirical evidence reveals that seawater is a damping medium, that is, waves propagating through it suffer an intensity decay, apart from that caused by purely geometrical spreading. This additional attenuation produced by physical-chemical reactions grouped into two types of processes that convert acoustic energy into heat: effects associated to shear and volume viscosities, and a series of ionic relaxation processes involving, mainly, magnesium sulfate $MgSO_4$ and boric acid $B(OH)_3$. The energy loss is modeled through the logarithmic seawater absorption coefficient α. The value of α, expressed in dB/km, strongly depends on the frequency, but also on temperature, salinity, hydrostatic pressure (depth) and acidity. Our model estimates this

coefficient according to the formula in Ainslie and McColm (1998):

$$\begin{aligned}\alpha &= 0.106\exp\big((\mathrm{pH}-8)/0.56\big)\frac{f_1 f^2}{f_1^2+f^2} \\ &+ 0.52\left(1+\frac{T}{43}\right)\left(\frac{S}{35}\right)\exp(-d/6)\frac{f_2 f^2}{f_2^2+f^2} \\ &+ 0.00049\exp\big(-(T/27+d/17)\big)f^2, \end{aligned} \tag{2.2}$$

where

$$f_1 = 0.78\left(\frac{S}{35}\right)^{1/2}\exp\left(T/26\right)$$

is the boron acid relaxation frequency in kHz,

$$f_2 = 42\exp\left(T/17\right)$$

is the magnesium sulfate relaxation frequency in kHz, f is the sound frequency in kHz, T is the seawater temperature in °C, S is the salinity in ppt, d is the depth in km, and pH is the measure of the acidity.

If part of data is missing, Equation (2.2) can be replaced by

$$\alpha = 0.159\frac{f^2}{2.25+f^2} + 30.5\frac{f^2}{1764+f^2} + 0.000261 f^2, \tag{2.3}$$

that considers the average conditions at the ocean surface: $T = 17$ °C, $S = 35$ ppt, d=0 km and pH = 8. Figure 2.2 shows the dependence of the absorption coefficient with the frequency according to Equation (2.3). Note that the absorption is specially significant for frequencies above a few kHz, while it can be neglected for short and mid-range propagations at low frequency.

2.1.3.2 Interference

Wave theory fulfills superposition principle. Therefore, the simulation tool should has to reproduce the contribution of different waves traveling with different directions. This contributions are also called interferences and they can be either constructive or destructive.

In the case of assessing the environmental impact of the noise on sea wildlife, interference becomes relevant if the wavelength is about meters. This occurs near the low frequency limit (i.e. $\lambda \approx 1$ m). That is, interference is crucial for simulations with multiple noise sources or strong reflections inside the domain, whenever low frequencies are considered.

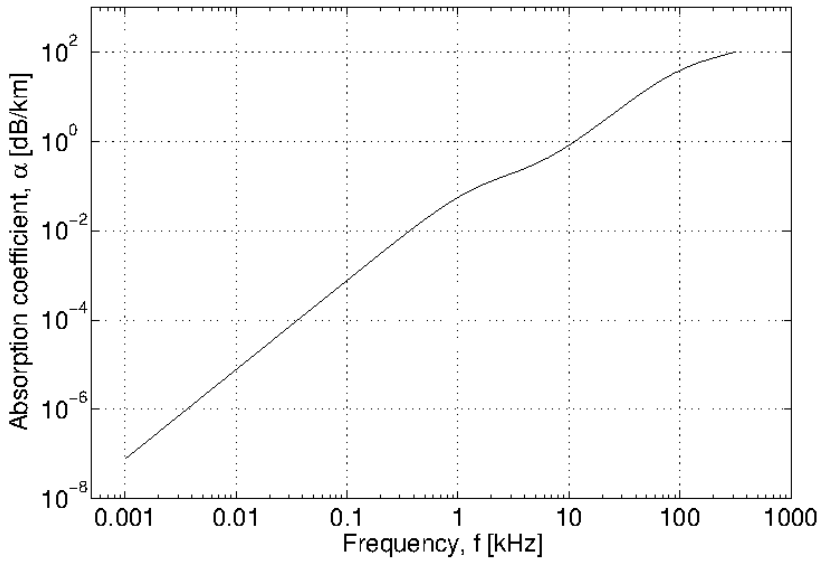

Figure 2.2: Absorption coefficient α under the following conditions: $S = 35$ ppt, $T = 17°C$, $d = 0$ km, pH = 8.

2.1.3.3 Reflection

When a wave front bounces off a medium discontinuity, part of the energy is transmitted to the outgoing medium and part of the energy is *reflected* back into the ingoing medium, due to the acoustic impedance mismatch. This occurs at the boundaries of the seawater domain, surface and sea bottom, and in regions where a strong spatial gradient of sound speed is present, see Section 2.1.2. Section 4.2.3 details the mathematical treatment considered in this work.

Even more, if the interface is not regularly defined, for example in the case of a rough sea surface or sea bottom, reflection becomes diffuse, generating a phenomenon called reverberation. This is especially relevant for signal transmission, while negligible for environmental purposes.

2.1.3.4 Refraction

In addition to reflection, spatial gradients of sound speed have additional effects on sound propagation. A sound speed gradient which is normal to the propagation direction makes it bend towards the region with lower speed of sound. Refraction is noticeable if a strong gradient is present or in the case of long range propagation.

2.1.3.5 Diffraction

The Huygen-Fresnel principle states that every point of a wave front becomes a source of a secondary spherical wave. According to this, and to some additional assumptions, when a wave encounters an obstacle with a size similar to the wavelength, a effect called diffraction introduces changes in the shape of the wave front.

Geometrical spreading can be understood as a consequence of the same principle. Every point of the wave front plays the role of a new wave source. This is the main physical mechanism producing sound intensity attenuation, together with seawater absorption.

2.2 Anthropogenic noise sources

Underwater noise is classified into natural and anthropogenic, depending on the type of source. On the one hand, waves, rain, earthquakes, thunders, ice-breaking, ocean fauna are considered natural noises. On the other hand, multiple human activities introduce undesirable levels of noise intensity into the ocean, such as seismic exploration, military and civil sonar operation, commercial shipping, explosions, inshore and offshore construction, oil and gas extraction or offshore energy generation Hildebrand (2004). Table 2.1 presents a non-exhaustive list of oceanic noise sources. The environmental impact of the noise generated by each type of source depends on frequency, intensity and time distribution. Figure 2.3 presents the Wenz curves, which approximate the noise spectra for each type of source, see details in Wenz (1962).

The tool developed in this thesis has been devised to simulate the underwater propagation of man-made acoustic pollution and, in particular, the operational noise generated by offshore renewable energy stations. These stations convert wind or wave energy into electricity. While wind energy technology has been developed during the last decades, wave energy converters devices are still at initial stages of technological refinement. Wave energy conversion is a relatively new technology with a wide variety of prototypes, based on different technologies. Therefore, we highlight that there is a severe lack of data related to the noise generated by wave energy devices.

Wind farms produce noise at a wide spectrum of frequencies. For instance, Figure 2.4 depicts the spectra measured near four turbines in the Baltic Sea. Although they are particular cases, the observed curves can be considered qualitatively representative of other offshore wind farms. Peaks can be clearly identified at 125 Hz, and non-

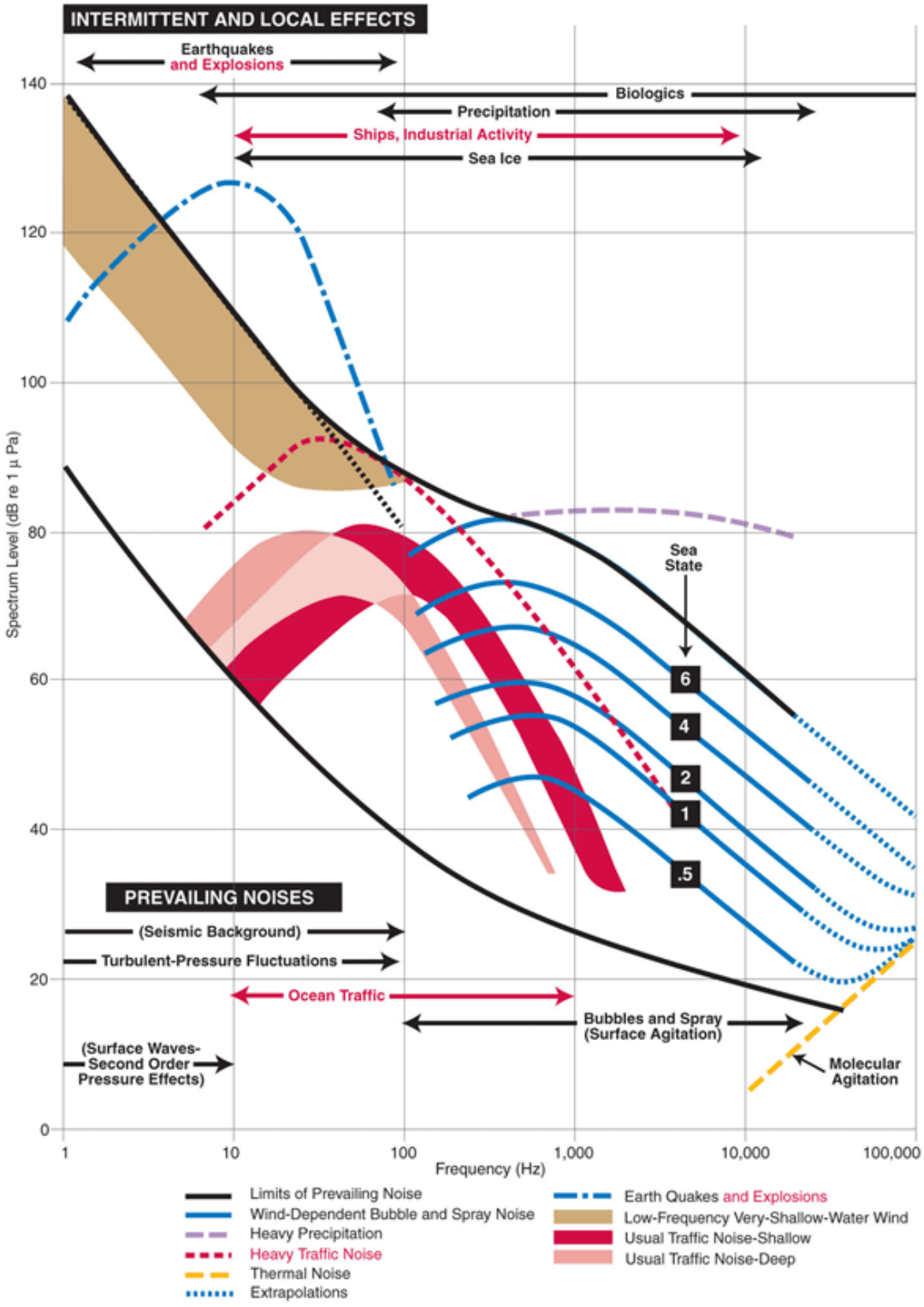

Figure 2.3: Wenz curves showing typical underwater noise spectra. From National Research Council (2003).

Natural noise sources	Anthropogenic noise sources	
	Intentional	Unintentional
• Wind • Rain • Precipitation other than rain • Lightning • Mammals • Fish • Crustaceans • Biota other than mammals, fish and crustaceans • Breaking gravity (surf) waves • Wave-wave interactions • Flow noise • Gravel noise • Thermal noise	• Seismic explorations • Normal-incidence echo sounder • Fish-finding sonar • Sub-bottom profiler • Military search sonar • Obstacle avoidance sonar • Sidescan sonar • Minesweeping equipment • Multibeam echo sounder • Doppler current profiler • Research sonar • Acoustic communications equipment • Acoustic transponders • Acoustic deterrent devices • Acoustic cameras	• Shipping: merchant, ferries, tankers (incl. supertankers), leisure craft • Fishing vessels • Dredging, pipelaying, cable laying • Explosives: mine & bomb clearance • Offshore industry – Platform construction (pile driving, alternative methods) – Platform operation (e.g. wind turbines) – Platform maintenance (supply, tugs) – Oil & gas platforms: pumping, drilling, associated supply & maintenance) – Flow noise (pipelines) – Wind farm decommissioning • Industrial/harbour noise • Ship shock trials

Table 2.1: Examples of natural and anthropogenic noise sources in the sea. From National Research Council (2003).

negligible values of SPL at low (16 Hz) and high (16 kHz) frequencies. This is the reason why some regulations focus on this frequency band, see Section 2.4.

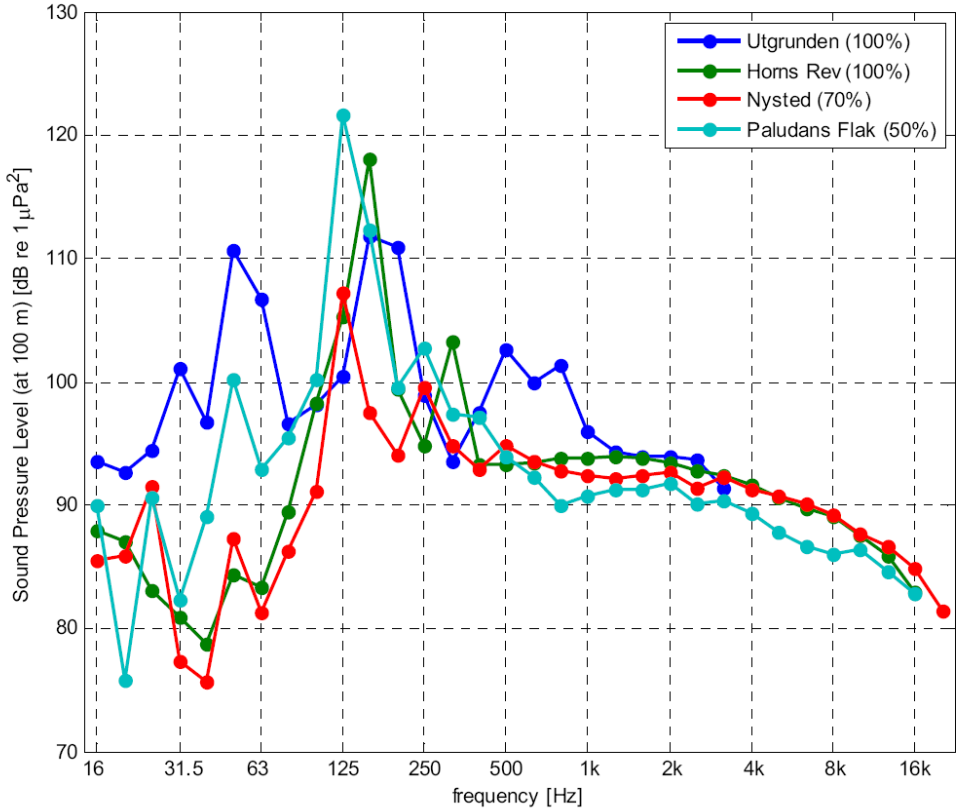

Figure 2.4: Example of 1/3-octave band spectra of the received underwater sound at about 100 m of operational wind turbines, recorded in four wind farms in the Baltic Sea, after the report of Institut für Statik und Dynamik of the Leibniz Universität Hannover (2007). The percentages in the legend refer to the produced electric power relative to the nominal power. From Ainslie et al. (2009).

2.3 Environmental impact of underwater noise

Until the last decades, few efforts were focused on assessing the environmental impact of underwater noise. As a consequence, there was a lack of knowledge on its impact on sea fauna. To overcome this lack of knowledge, special efforts are focused on monitoring the underwater noise levels Nedwell et al. (2003); Ainslie et al. (2009), identifying and characterizing the effects of the noise on the marine endangered species Dufault (2005); Thomsen et al. (2006); Thomsen (2009), and establishing criteria to assess its impact Southall et al. (2007). For instance, nowadays it is well-known that a high level of exposure produces behavioral changes, masking of sounds of interest, hearing losses and temporary or permanent injuries over the marine fauna.

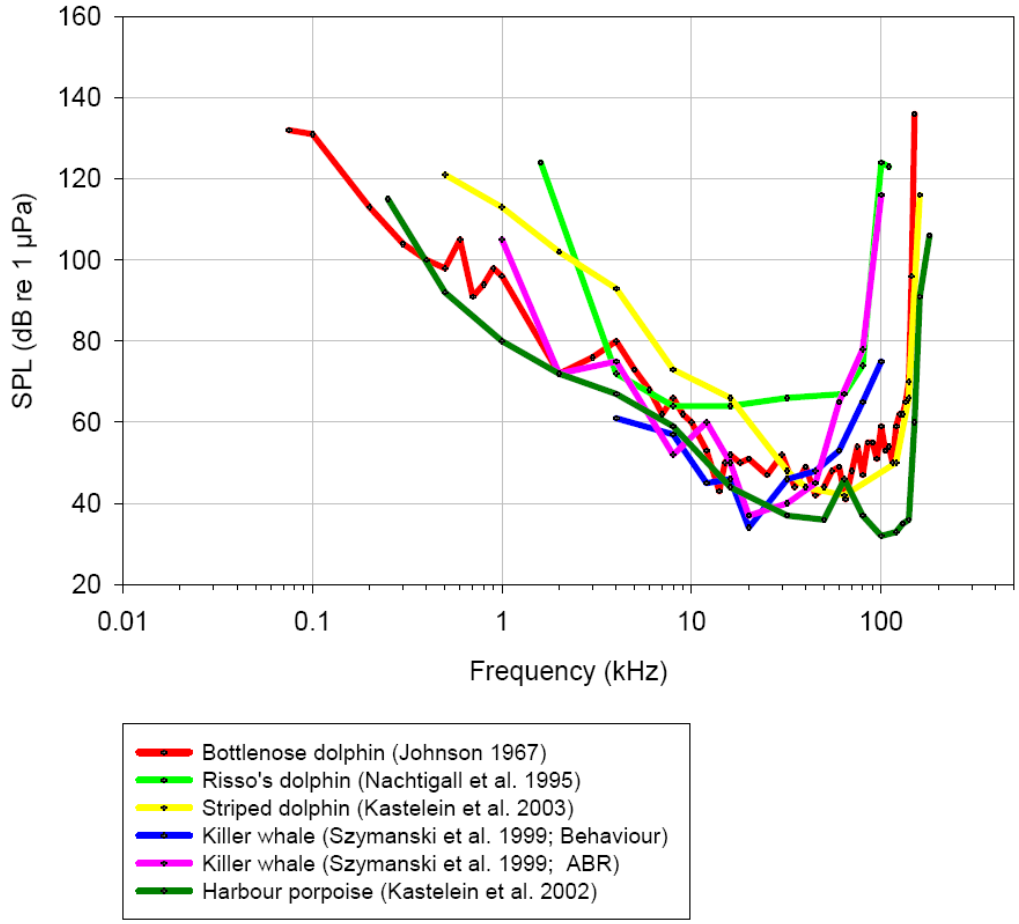

Figure 2.5: Audiograms of odontocete species. From Thomsen et al. (2006).

Marine species are equipped with a variety of hearing mechanisms and specializations. Furthermore, specific species have different hearing abilities at different frequencies. Nedwell et al. (2004) describe the hearing mechanisms present in fishes (which are poorly understood) and marine mammals, and collects a set of audiograms and the methodology to obtain them. An audiogram shows which is the minimum sound pressure level that allows the detection of any response in the animal, at each frequency band. Several audiograms for fish and marine mammal species are included in Figures 2.5 and 2.6. It is important to point out that the frequency domain ranges from about 10 Hz to 10^5 Hz. It is highly remarkable that some marine mammals species (mainly odontocetes) have hearing capabilities up to 100 kHz, even though noises with a frequency higher than 20 kHz are ultrasounds for humans.

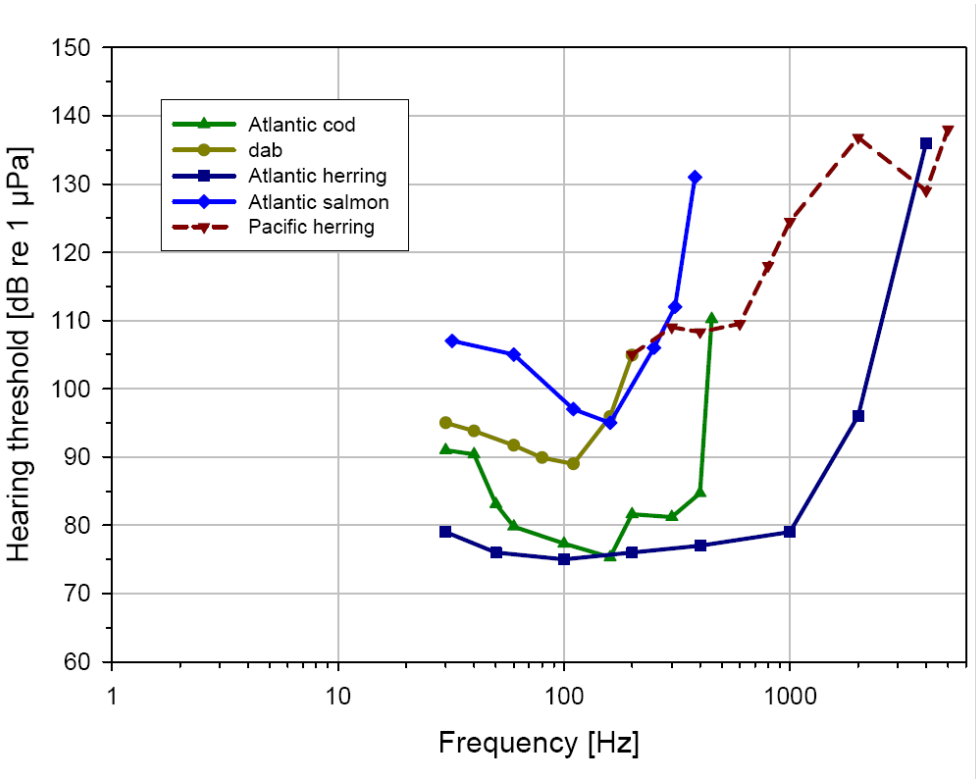

Figure 2.6: Audiograms of Atlantic salmon (Salmo salar) (Hawkins and Johnstone 1978), Atlantic cod (Chapman and Hawkins 1973) Atlantic herring (Enger 1967), and dab (Chapman and Sand 1974). For comparative purpose, the audiogram of Pacific herring (Mann et al. 2005) is included. From Thomsen et al. (2006).

According to Richardson et al. (1995); Commission (2008), the main effects of the underwater noise on the marine fauna are the following (see Figure 2.7):

1. Detection: when the noise intensity exceeds the background noise intensity and the hearing threshold, the animal detects the noise. Simple detection not producing masking or a behavioral response must be identified by monitoring of the electrical activity of the animal‘s hearing mechanism.

2. Masking: obscuring of sounds of interest by interfering sounds, generally at similar frequencies Simpson et al. (2016). Marine mammals are highly dependent on sound, and their ability to recognize sound signals over noise is important in communication, predator and prey detection, and, in the case of toothed whales, echolocation.

3. Behavioral response: behavioral reaction such as leaving the noisy area.

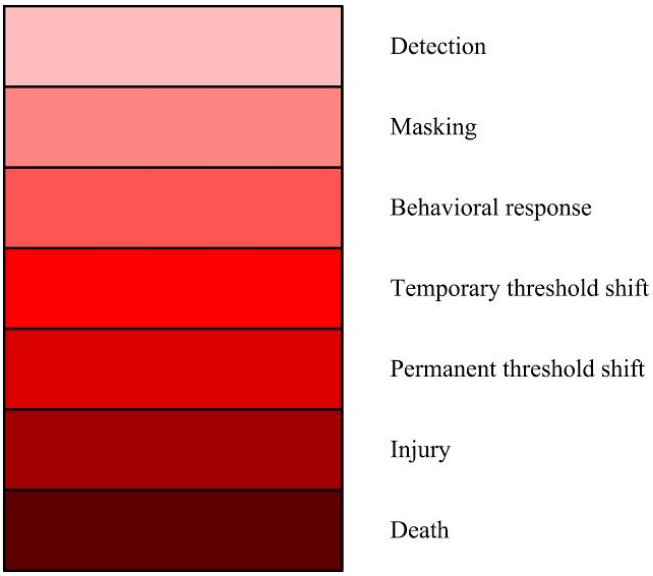

Figure 2.7: Levels of impact produced by underwater noise on marine fauna.

4. Temporary threshold shift (TTS): a temporary elevation of the hearing threshold due to noise exposure.

5. Permanent threshold shift (PTS): a permanent elevation of the hearing threshold due to noise exposure.

6. Injury: Further tissue damage due to noise exposure (lesions in lungs, ears or other internal organs, external hemorrhages, etc.).

7. Death: powerful noises from some directional sonars, pilling or explosions can cause death in some species, as it is documented in Cox et al. (2006).

Inspired in the methodologies that are applied to human hearing research, the current trend in marine noise exposure criteria is to incorporate frequency-weighted hearing curves to marine mammals sound-level measurement. Frequency-weighted curves allow the conversion of sound pressure level spectrum into a scalar value, penalizing the frequencies that produce a more intense response or damage to the species. For instance, marine mammals species are classified into 5 groups, depending on similarities in their hearing: mysticetes, mid-frequency odontocetes, high-frequency

odontocetes, pinnipeds listening in air and pinnipeds listening in water. While in humans the so-called A- or C-weighted curves are used, an M-weighting function is assigned to each group in order to predict auditory damage, rather than detection or behavioral response. See Southall et al. (2007) for more details on sound exposure criteria.

2.4 Regulation on marine environmental acoustics

The growing social concern on the environmental impact of underwater noise materialized in several national and international regulations and agreements. Legislation has been evolving in an attempt to understand and control the noise levels that affect marine ecosystems. There is a particular concern about marine mammals, due to their social impact, although new research points out that more and more marine species can detect sound and use it in several ways.

The first documents regulating marine environment stated the importance of the preservation on marine ecosystems, emphasizing the prevention and reduction of pollution. More recent regulations explicitly identifies man-made noise as a specific type of pollution that causes an impact on these ecosystems Marine Mammal Commission (2007); OSPAR Commission and others (2005), and plans to establish limits on the generated noise intensity The European Commission (2008). In particular, Descriptor 11 from the European Union Commission Decision 2010/477/EU requires future monitoring programs to assess the underwater noise with frequencies ranging between 10 Hz and 10 kHz.

The Coastal Zone Management Act (CZMA) of 1972

The CZMA is a US federal law which is administered within the National Oceanic and Atmospheric Administration (NOAA), in the USA, through the Office of Ocean and Coastal Resource Management. The CZMA recognizes “the national interest in the effective management, beneficial use, protection, and development of the coastal zone” and combines federal/state partnership for managing coastal resources The 92nd United States Congress (1972).

In the context of this federal Act, the Californian Coastal Commission has monitored and controlled several activities likely to produce an acoustic impact, during the past decades. In addition, it imposed operational and geographic restrictions as well as mitigation measures. Although, the active tasks carried out in California contrast with the lower degree of regulation in the rest of the states.

The Marine Mammals Protection Act of 1972 (MMPA)

The first regulation protecting the health of the marine fauna and promoting the collection of data on the health of marine fauna was the US Marine Mammal Protection Act of 1972 (MMPA) Marine Mammal Commission (2007).

The MMPA was enacted in response to increasing concerns among scientists and citizens that significant declines in some species of marine mammals were caused by human activities. The Act established a national policy, the Program in Marine Mammal Health and Stranding Response, that "shall facilitate the collection and dissemination of reference data on the health of marine mammals and health trends of marine mammal populations in the wild; and correlate the health of marine mammals and marine mammal populations, in the wild, with available data on physical, chemical, and biological environmental parameters". The target was to prevent marine mammal species and population stocks from declining beyond the point where they ceased to be significant functioning elements of the ecosystems of which they are a part.

It is important to point out that in the first marine environmental regulations, such as the CZMA and the MMPA, no specific mention to noise pollution can be found, even tough it can be implicitly considered as a harassment. The term harassment is defined as "any act of pursuit, torment, or annoyance which has the potential to injure a marine mammal or marine mammal stock in the wild, or has the potential to disturb a marine mammal or marine mammal stock in the wild by causing disruption of behavioral patterns, including, but not limited to, migration, breathing, nursing, breeding, feeding, or sheltering". However, since late 1990s noise pollution recursively appears as a type of man-made pollution. In 1998, the MMPA included a set of statutory provisions clearly stating that "noise and other anthropogenic changes in the habitat of whales may affect whale populations adversely".

The OSPAR Convention

The OSPAR Convention takes its name from the cities that hosted two previous conventions (Oslo in 1972, and Paris in 1974). The complete name of the convention is Convention for the Protection of the Marine Environment of the North-East Atlantic, which was created in 1992. The Contracting Parties comprise the twelve countries located at the western coasts of Europe, the European Union, Luxembourg and Switzerland, due to their location within the catchments of the Rhine River, and Finland, with some rivers flowing to the Barents sea and historically involved in the efforts to control the dumping of hazardous waste in the Atlantic and the North Sea OSPAR Commission and others (2005).

In the Preamble, the Convention recognizes that "the marine environment and the fauna and flora which it supports are of vital importance to all nations, and the inherent worth of the marine environment of the North-East Atlantic and the necessity for providing coordinated protection for it". It is also stated that the pollution threatens the ecological equilibrium and the need of "measures with respect to the prevention and elimination of pollution of the marine environment". In Article 1, it is established that "pollution means the introduction by man, directly or indirectly, of substances or energy into the maritime area which results, or is likely to result, in hazards to human health, harm to living resources and marine ecosystems, damage to amenities or interference with other legitimate uses of the sea". Article 5 rules that "The Contracting Parties shall take, individually and jointly, all possible steps to prevent and eliminate pollution from offshore sources in accordance with the provisions of the Convention, in particular as provided for in Annex III". Annex IV states that the Contracting Parties shall cooperate in the use and development of scientific assessment tools, such as modeling, remote sensing and progressive risk assessment strategies, carry out research, and take into account the scientific progress.

The Marine Strategy Framework Directive 2008/56/EC (MSFD)

The European Union Marine Strategy Framework Directive The European Commission (2008) is the European Union's wager for the conservation of "marine waters under the sovereignty and jurisdiction of Member States of the European Union", approved in 2008. This Directive recognizes the evident pressure on natural marine resources and describes the marine environment as a precious heritage that must be protected. Article 1 literally says: "This Directive establishes a framework within

which Member States shall take the necessary measures to achieve or maintain good environmental status in the marine environment by the year 2020 at the latest", and forces the Member States to protect and preserve the marine environment, and to prevent and reduce inputs in it.

Article 3 includes some basic definitions. For instance, "a good environmental status (GES) means the environmental status of marine waters where these provide ecologically diverse and dynamic oceans and seas which are clean, healthy and productive within their intrinsic conditions, and the use of the marine environment is at a level that is sustainable, thus safeguarding the potential for uses and activities by current and future generations". The eighth definition explicitly points at anthropogenic noise as a type of pollution: "pollution means the direct or indirect introduction into the marine environment, as a result of human activity, of substances or energy, **including human-induced marine underwater noise**, which results or is likely to result in deleterious effects such as harm to living resources and marine ecosystems, including loss of biodiversity, hazards to human health, the hindering of marine activities, including fishing, tourism and recreation and other legitimate uses of the sea, impairment of the quality for use of sea water and reduction of amenities or, in general, impairment of the sustainable use of marine goods and services".

Annex 1 of MSFD collects a set of qualitative descriptors to determine GES. In particular, the eleventh descriptor explicitly refers to underwater noise as a type of energy pollution. Moreover, Annex III also mentions underwater noise as a physical disturbance, see Table 2.2.

The MSFD requires Member States to develop strategies that should lead to programs of measures that achieve or maintain GES, including monitoring programs for assessment. In Commission Decision 2010/477/EU The European Commission (2010), criteria and methodological standards on GES of marine waters were published. Two indicators were described for Descriptor 11 (Noise/Energy): Indicator 11.1.1 on low and mid frequency impulsive sounds, and Indicator 11.2.1 on continuous low frequency sound (ambient noise). Under the Working Group on Good Environmental Status, a Technical Subgroup on underwater noise (TSG noise) was created with the objective of "clarifying the purpose, use and limitation of the indicators and described methodology that would be unambiguous, effective and practicable". The result is the Monitoring Guidance for Underwater Noise in European Seas, recently published Dekeling et al. (2013), which allowed starting programs for underwater

Table 2

Pressures and impacts

Physical loss	— Smothering (e.g. by man-made structures, disposal of dredge spoil), — sealing (e.g. by permanent constructions).
Physical damage	— Changes in siltation (e.g. by outfalls, increased run-off, dredging/disposal of dredge spoil), — abrasion (e.g. impact on the seabed of commercial fishing, boating, anchoring), — selective extraction (e.g. exploration and exploitation of living and non-living resources on seabed and subsoil).
Other physical disturbance	— Underwater noise (e.g. from shipping, underwater acoustic equipment), — marine litter.
Interference with hydrological processes	— Significant changes in thermal regime (e.g. by outfalls from power stations), — significant changes in salinity regime (e.g. by constructions impeding water movements, water abstraction).
Contamination by hazardous substances	— Introduction of synthetic compounds (e.g. priority substances under Directive 2000/60/EC which are relevant for the marine environment such as pesticides, anti-foulants, pharmaceuticals, resulting, for example, from losses from diffuse sources, pollution by ships, atmospheric deposition and biologically active substances), — introduction of non-synthetic substances and compounds (e.g. heavy metals, hydro-carbons, resulting, for example, from pollution by ships and oil, gas and mineral exploration and exploitation, atmospheric deposition, riverine inputs), — introduction of radio-nuclides.
Systematic and/or intentional release of substances	— Introduction of other substances, whether solid, liquid or gas, in marine waters, resulting from their systematic and/or intentional release into the marine environment, as permitted in accordance with other Community legislation and/or international conventions.
Nutrient and organic matter enrichment	— Inputs of fertilisers and other nitrogen — and phosphorus-rich substances (e.g. from point and diffuse sources, including agriculture, aquaculture, atmospheric deposition), — inputs of organic matter (e.g. sewers, mariculture, riverine inputs).
Biological disturbance	— Introduction of microbial pathogens, — introduction of non-indigenous species and translocations, — selective extraction of species, including incidental non-target catches (e.g. by commercial and recreational fishing).

Table 2.2: Environmental pressures and impacts considered by Annex III of the European Marine Strategy Framework Directive. Underwater noise is included as a physical disturbance. From The European Commission (2008).

noise monitoring. This document strongly suggests the use of modeling as an excellent complement for the in situ noise measurement.

As mentioned above, MSFD identifies two types of anthropogenic noise sources, namely impulsive sounds and low frequency continuous noise.

Impulsive noise The environmental impact introduced by impulsive noise events is evaluated by measuring the displacements of sea fauna individuals due to the noise disturbance. Indicator 11.1.1 defines *considerable* displacement as "the displacement of a significant proportion of individuals over a relevant time period and spatial scale". This impact will have to be restricted when caused by anthropogenic noise.

The guide prescribes the measurement of the distribution in time and place of impulsive sounds between 10 Hz and 10 kHz (indicator 11.1.1). In order to establish the current level and trend of impulsive sounds, a register of occurrence should be set up, by dividing the sea surface into a coarse mesh of 10 x 5 nautical miles, and collecting the following main items:

- Pulse-generating activity
- Day
- Location
- Source level

Ambient noise The ambient noise is composed of natural and anthropogenic sounds, although it is not clear if it will be possible to distinguish between them.

Indicator 11.2.1 requires the analysis of the trends in the annual average of the continuous low frequency sound, in the third octave bands of 63 and 125 Hz (a one-third octave band is defined as a frequency band whose upper band-edge frequency is the lower band frequency times the cube root of two). The lack of historical measurements motivated the Directive to impel the Member States within a sub region to establish an ambient noise monitoring system. The guide recommends 1 year averaging and the use of arithmetic means to establish average ambient noise levels.

The guide affirms that the combined use of measurements and models is the best way to perform the monitoring. Directly related to numerical models, Section 3.3.1 of Part II of the guide states that the use of these models

- contributes to the creation of noise maps,
- constitutes a reliable and cost-effective manner for trend estimation,
- identifies trends for different sources, separately,
- reduces the time to establish a trend, and optimizes the number of monitoring stations,
- helps with the choice of monitoring locations and equipment,
- predicts the effect of future changes and re-constructs a history of the past (hind-cast),
- permits the removal of selected sources if considered not causing a departure from GES,
- provides a better overview of actual noise levels and their distribution.

Section 3.5 of the same part includes technical specifications for "appropriate noise monitoring models". The following points are particularly mentioned as conditions that should be considered by a model: a good characterization of the source, the global bathymetry, the sound velocity profile, the absorption of sound in seawater and the sediment composition.

Although not directly related to this thesis, it is worth to mention that the guide also includes recommendations for the placements of measurement devices, and specifications for the equipment.

Chapter 3

Numerical methods for underwater acoustic problems

This chapter summarizes the past and current techniques devised for simulating the underwater sound propagation. The chapter is composed of 2 sections. Section 3.1 collects a brief historical review of the relevant progress made on the theory of underwater sound propagation. Section 3.2 outlines the current state-of-the-art of the different mathematical and numerical models.

3.1 Historical overview

In 1877, the physicist Lord Rayleigh published one of the first books covering a rigorous analysis of the generation, propagation and reception of sound. Before him, many researchers made important contributions in acoustics, such as Leonardo da Vinci, Isaac Newton, Joseph Fourier or Daniel Colladon, who measured the speed of sound in water, in 1827. The interest in quantifying underwater sound propagation was strongly motivated by the appearance of the first sonar device in 1912, right after the sinking of the Titanic. The sonar technique was conceived to establish communications and to detect objects on or under the sea surface, such as other vessels or icebergs. Other primitive electrical and electronic components and technology were also developed during the beginning of the 20th century.

The outbreak of World War I promoted significant progress in underwater acous-

tics. Rotating binaural listening devices and towed hydrophone devices were successfully employed to detect and locate enemy submarines. Since that moment and until the end of the Cold War, the research on underwater acoustics remained inexorably attached to the development of underwater military devices.

In 1919, the German scientist Lichte (1919) published the first scientific paper on underwater sound, describing theoretically the bending of sound rays (refraction) produced by slight temperature and salinity gradients in the sea. An improved understanding of the physical phenomena involved in sound propagation in the sea began to emerge in the 1930s. The seemingly unpredictable behavior of the ocean as a sound transmission medium began to be understood with the invention of the bathythermograph by Athelsan Spilhaus in 1937, which allowed the measurement of the vertical profile of the seawater temperature.

During the World War II, the interest in pro-submarine and anti-submarine equipment continued to gain importance, and the National Defense Research Committee and several other laboratories carried out an extensive program in underwater acoustics. The purpose of the work of these groups was to improve the design and use of underwater acoustic systems, collecting large amounts of experimental measurements and understanding the factors affecting sound speed in the ocean. During the Cold War, the experimental and theoretical work was continued and expanded to cover the entire sonic as well as ultrasonic region, which enabled more complex sonar system.

In parallel to the development of knowledge and devices related to underwater acoustics, different techniques addressed to the modelization and estimation of the propagation of underwater sound were explored, see next section. More recently, in the course of the last four decades, there has been an increasing number of anthropogenic interventions in the seas with an evident acoustic impact. For instance, a continuously growing commercial shipping, geophysical exploration, operation offshore platforms, noise produced by advanced warfare, and other offshore human activities, see Section 2.2. This trend sparked a significant surge in the number of research projects on underwater acoustics with environmental purposes, leading to a better comprehension and awareness of the risk of noise pollution.

At the same time, the social concern about the environmental impact of the underwater noise pushed public administrations to create regulations limiting the acoustic pollution and even requiring Environmental Impact Assessments (EIA) prior to the acceptance of execution of some engineering projects. This scenario created the need

of more reliable acoustic simulations [1] and motivated laboratories and environmental consultancy companies to develop more complex noise propagation numerical models. As a direct consequence, several numerical methods with growing refinement have been developed to predict the sound pressure level.

3.2 Mathematical and numerical methods for underwater sound propagation

This section outlines the most relevant mathematical and numerical methods used to obtain estimations of the underwater noise propagation. These methods present a wide variety in applicability and complexity, from the simplest range-dependent simplified equation to the more complex three-dimensional finite element methods. Most of them are currently in use, the choice typically depends on the available data, frequency range, domain size, desired accuracy and availability of computational resources.

3.2.1 The sonar equations

The simplest method consist of a single equation that computes the transmission loss in terms of the geometrical spreading, the seawater absorption and, eventually, the ducting effect of the deep sound channel (Section 2). Thus, the source level, the range and few parameters such as the seawater absorption are the only inputs to obtain a first approximation value for the sound level at a point, without the requirement of a detailed bathymetric survey of the area of the project nor the acoustic properties of the sea bottom. Hazelwood and Connelly (2005) collect some of these simplified equations. For instance, the spherical spreading (deep water) of the sound produced by a point source can be modeled by

$$\mathrm{SPL}(r) = \mathrm{SL} - 20 \cdot \log r - \alpha r \ ,$$

where SPL is the sound pressure level (dB) (Section 2.1.1), SL is the source level (dB), r is the range (m) and α is the absorption rate (dB/m), see Section 2.1.3.1.

[1] Ainslie et al. (2009) state that: "...the next challenge is to predict correctly how the sound propagates in the shallow water of the North Sea..." and "It should be investigated whether the method used for the calculation of propagation losses and the generation of underwater sound maps can (in the long term) be further developed to a generally applicable legal basis for underwater sound, as exists for sound in air (industrial and traffic noise)".

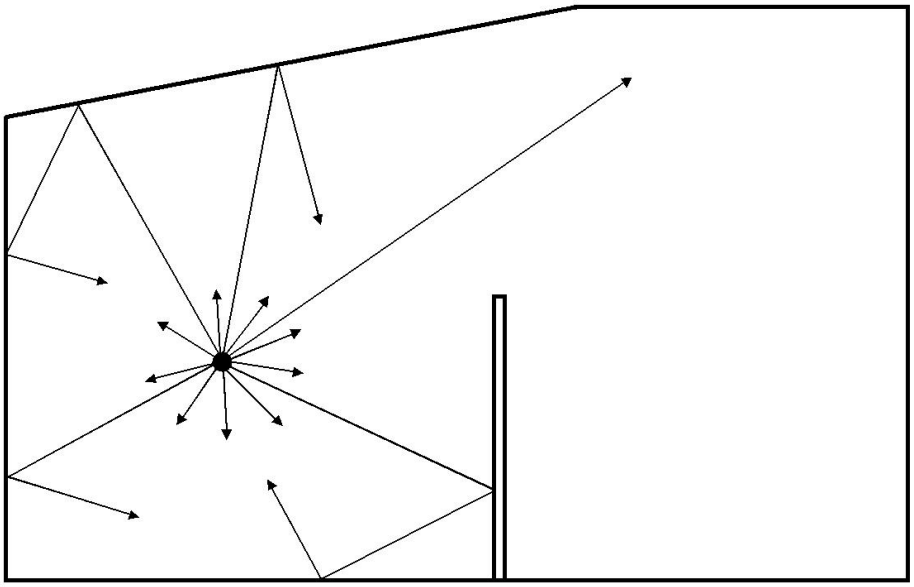

Figure 3.1: Example of a 2D diagram of the ray-tracing method applied to room acoustics. From Oliva-Elorza (2005).

There are versions of the sonar equation for shallow water, with cylindrical spreading. These equations usually consider that the surface is fully reflective. The main drawback of these methods is the limited accuracy of the output under a wide variety of circumstances.

3.2.2 Ray tracing

Ray tracing is a method for estimating the path of waves through a medium, by repeatedly advancing idealized narrow beams called rays by discrete amounts, see Figure 3.1. The direction of these rays is normal to the wave fronts and may change slightly at discrete points if it is affected by refraction, when a non-uniform propagation velocity distribution is present (Section 2.1.3.4). Surface reflections and medium absorption are also easily considered. However, the wave theory is only partially considered. For example, the diffraction phenomenon is not intrinsically included and, thus, ray theory is generally applied to high frequency problems with a wavelength much shorter than the geometrical features of the domain. For low frequencies, the wave length value is similar to the scale of the seabed features and, thus, the diffraction effects cannot be neglected. In addition, the interference between acoustic beams is not included, producing a limited accuracy in some cases.

Despite of these shortcomings, ray tracing models have several advantages. For instance, they are fast from the computational point of view. Moreover, the paths and travel times of the ray coordinates are independent of the frequency. Hence, the same diagram is valid for different frequency bands, and they can be reused in order to recalculate the sound intensity for each new frequency. This technique is commonly used in fields such as computer graphics, optics and the propagation of electromagnetic and mechanical waves, including acoustics. Ray tracing methods are widely applied for numerically simulating the noise propagation in air (e.g. room acoustics) Svensson and Krokstad (2008). Note that, in those problems, high frequencies are present, the number of reflecting surfaces is significant and refraction is negligible.

Ray tracing was one of the first numerical techniques that was developed for underwater sound propagation Anderson and Pedersen (1956); Pekeris and Longman (1958); Graber et al. (1961). It was applied to high frequency bands and incorporated surface and seabed reflections, refraction and seawater absorption.

An improved version of the method, called the Gaussian beam tracing, was developed in the eighties, mitigating some of the artifacts inherent to the standard ray tracing method, by associating to each ray a beam with a Gaussian intensity profile, normal to the ray Červenỳ et al. (1982); Porter and Bucker (1987). Later, a hybrid method that couples Gaussian ray tracing method with the finite element method, called the finite element ray tracing method, was introduced in Porter and Liu (1994). The Marine Operations Noise Model (MONM) BELLHOP code Rodriguez (2008); Zykov et al. (2013) is a commercial code widely used that implements the finite element ray tracing method for medium and high frequencies. Figure 3.2 shows an example of a noise map produced with MONM-BELLHOP code.

It is important to point out that MONM is not a real 3D model for the underwater noise propagation problem. The following paragraph is extracted from (Zykov et al., 2013, Section 2.2):

> "MONM computes acoustic fields in three dimensions by modeling transmission loss (via BELLHOP or RAM) within two-dimensional (2D) vertical planes aligned along radials covering a 360° swath from the source, an approach commonly referred to as Nx2D. These vertical radial planes are separated by an angular step size of $\Delta\theta$, yielding N = $360°/\Delta\theta$ number of planes. MONM treats frequency dependence by computing acoustic

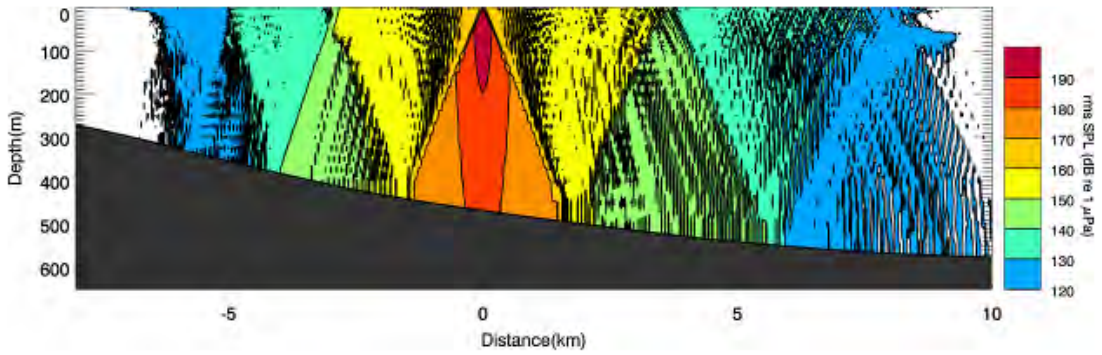

Figure 3.2: Example of a noise propagation map computed with MONM-BELLHOP model, based on the finite element ray tracing method. Vertical cross-section of the 12 kHz frequency band for a multibeam sonar. From Zykov et al. (2013).

> transmission loss at the center frequencies of 1/3-octave bands. Sufficiently many 1/3-octave bands, starting at 10 Hz, are modeled to include the majority of acoustic energy emitted by the source. At each center frequency, the transmission loss is modeled via BELLHOP or RAM within each vertical plane (Nx2D) as a function of depth and range from the source. Third-octave band received SELs are computed by subtracting the band transmission loss values from the directional SL in that frequency band. Composite broadband received SELs are then computed by summing the received 1/3-octave band levels."

3.2.3 The wave equation

Underwater noise is a mechanical phenomenon caused by an unbalanced gradient in the pressure field. For an oscillating noise source, the wave consists of regions of compression and rarefaction that move, or propagate, away from the source at a constant rate (the sound speed) determined by the properties of the medium, see Figure 3.3. The fundamental mathematical equation governing this phenomenon is the wave equation:

$$\frac{\partial^2 \hat{p}_{(\mathbf{x},t)}}{\partial t^2} = c^2 \Delta \hat{p}_{(\mathbf{x},t)} \ , \tag{3.1}$$

where $\hat{p}$ is the pressure (time and space dependent), $\mathbf{x}$ is the position vector, t is the time, c is the sound speed, and Δ is the Laplacian operator.

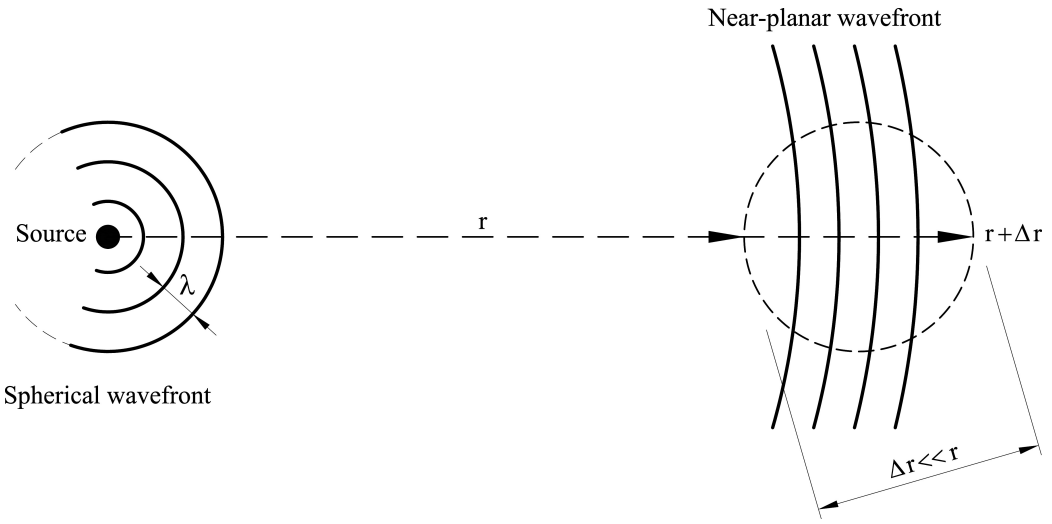

Figure 3.3: Propagation of the sound waves generated by a point source in a homogeneous medium. From Burdic (1983).

Equation (3.1) takes into account all the physical aspects of the wave propagation, including time-dependency, and no additional assumptions are made on the wave propagation behavior. This is typically useful when impulsive sounds, such as explosions or pulses, are addressed. Several numeral techniques have been developed to solve Equation (3.1), such as finite-difference based models Gerstoft (2002), fast-field-program techniques Porter (1990), and non-linear pulse propagation McDonald and Kuperman (1984).

However, full time-domain models based on Equation (3.1) are rather specialized and the computational cost involved in their direct solution is usually non-affordable for industrial applications. Therefore, additional assumptions are made in order to simplify the mathematical model.

3.2.4 Methods based on the Helmholtz equation

When non-impulsive noise sources are addressed, the input noise spectrum is decomposed into a set of harmonic frequency bands, and a simulation is performed for each band. To this end, the standard approach is to assume a time-harmonic solution for the pressure–a harmonic sound is a single-frequency sinusoidal source motion—, and apply separation of variables in the form

$$\hat{p}_{(\mathbf{x},t)} = p_{(\mathbf{x})} \exp(i\omega t) \ , \tag{3.2}$$

where $p_{(\mathbf{x})}$ is a complex space-dependent pressure field, $i = \sqrt{-1}$ is the imaginary unit and ω is the angular velocity,

$$\omega = 2\pi f \ ,$$

f being the frequency. Thus, the pressure has been factorized into a (in general complex) space-dependent factor and a harmonic time-dependent factor.

Introducing Equation (3.2) into Equation (3.1), we obtain the harmonic version of the wave equation, the Helmholtz equation:

$$\Delta p_{(\mathbf{x})} + k^2 p_{(\mathbf{x})} = 0 \ , \tag{3.3}$$

where k is the wavenumber,

$$k = \frac{\omega}{c} = \frac{2\pi f}{c} \ . \tag{3.4}$$

The wavenumber is related to the wavelength, which is the ratio between the sound speed c and the frequency f,

$$\lambda = \frac{c}{f} = \frac{2\pi c}{\omega} = \frac{2\pi}{k} \ , \tag{3.5}$$

and corresponds to the distance between two adjacent wave crests.

The general strategy is to decompose the continuous input SPL spectrum, see Equation (2.1), into third-octave frequency bands. Then, a simulation is performed for each band, generating at point location an output band spectrum.

Note that the Helmholtz equation derives directly from the wave equation and preserves the ability to incorporate all the wave phenomena into the model, except for time-varying non-harmonic effects. Thus, models using the Helmholtz equation (3.3) apply to harmonic inputs without further simplifications. For non-impulsive and non-harmonic noise input, the Helmholtz equation can be also applied generating output fields suitable for engineering purposes. In the case of strongly impulsive noise sources, the results obtained with a model based on the Helmholtz equation should be considered as a first approximation.

For oceanographic purposes, several models have been developed, based on different mathematical and physical simplifications. The most relevant are collected in the following sections.

3.2.4.1 Normal mode methods

Normal mode methods are based on the Helmoltz equation. They apply separation of variables, either in Cartesian or cylindrical coordinates, but always keeping the depth as an uncoupled variable. The range-dependent part of the pressure field is represented by Hankel functions. The depth-dependent part is ruled by an equation similar to the Schrödinger time-independent eigenvalue equation. It is decomposed into a finite sum of normal mode functions (eigenfunctions linked to eigenvalues, also called propagation numbers) plus a branch line integrals. These line integrals are usually neglected at large ranges Pekeris (1948).

As a consequence of the separation of variables (uncoupling depth and range), normal mode methods can be applied if the hypothesis of a nearly flat bottom and a stratified ocean is considered. This means that the acoustic parameters depend on depth and are independent of range. On the contrary, if the environment shows some range-dependence, either through the sound speed profile or the boundary conditions (for example not stratified ocean or non-mild bottom), normal mode theory does not apply. However, when the normal mode theory is applicable, the resulting models are versatile, robust and efficient. Further contributions enhanced the industrial applicability of these methods. Pierce (1965) extended normal mode theory to *almost-stratified* medium and slowly sloping bottom, by using ray theory to compute the waveguide paths followed by the different normal modes. Additionally, the attenuation produced by seawater absorption, see Section 2.1.3.1, was introduced as a perturbation inside the equations Levinson et al. (1995).

Several commercial codes are based on normal mode theory in the field of underwater acoustic propagation, such as KNORMA Boyles (1984), PROTEUS Gragg (1985), KRAKEN Porter (1992), MODELAB Levinson et al. (1995) and ORCA Westwood et al. (1996). The latter accounts for acousto-elastic ocean environments. KRAKEN is probably the most widely used normal mode model in the underwater acoustics community and is known for its accuracy and robustness. There is a complex eigenvalue version of the model, KRAKENC, that handles elastic media.

3.2.4.2 Methods based on parabolic equations

Parabolic methods were designed to analyze the long-range propagation of the sound along the deep sound channel (see Section 2.1.2 and Figure 2.1).

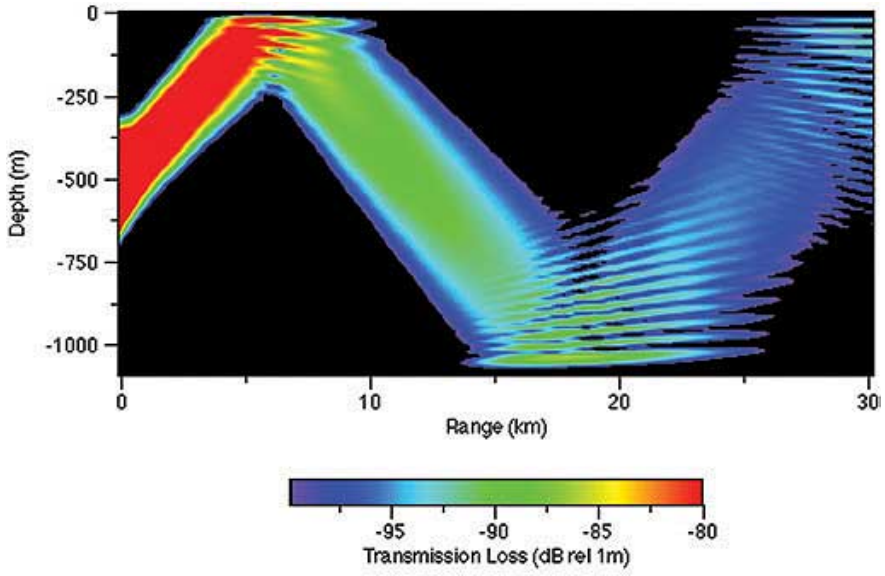

Figure 3.4: Example of a simulation computed with the original NRL-RAM in a simple ocean environment. From http://www.nrl.navy.mil/research/nrl-review/2003/simulation-computing-modeling/zingarelli/ .

Similarly to the normal mode methods, they are also based on the Helmholtz equation. They rely on four main assumptions:

- Outgoing energy dominates backscattered energy. Therefore, only forward propagation from the source point is considered.
- Energy propagates nearly horizontally. The resulting parabolic equation neglects strong vertical variations of the acoustic energy. Then, the solution will not capture non-smooth vertical variations in the sound pressure level.
- The variation with range of the physical properties of the seawater is smooth. In particular, this applies to the sound speed.
- The solution is only valid in the far field. Thus, these methods are not intended to be applied for assessing the environmental impact around off-shore stations.

These techniques were developed at the U.S. Naval Research Laboratory (NRL), by Michael D. Collins and other researchers, extending the work by Tappert (1977), and were called the Range-dependent Acoustic Model (RAM). Figure 3.4 shows an example of a simulation performed using RAM. Note that the range is about 30 km while the depth is just 1 km.

A consultancy company with experience in underwater acoustics assessments, JASCO Applied Sciences Ltd., incorporated the RAM model into its Marine Operations Noise Model (MONM), for low frequency underwater noise propagations (below 2 kHz).

It is important to highlight that the MONM-RAM is not a fully 3D model. In fact it uses a Nx2D strategy similar to the MONM-Bellhop, see Section 3.2.2 for details.

3.2.4.3 Standard Finite Element Methods

The finite element method is one of the most commonly used method to solve engineering problems modeled by partial differential equations, such as equations (3.1) and (3.3), having a strong theoretical background. The method discretizes the geometry using a mesh composed of a finite number of elements and nodes and approximates the solution by a linear combination of piecewise polynomials, usually called shape functions. The FEM with polynomials acting as shape functions is herein referred to as standard FEM.

However, the application of the standard FEM to solve the Helmholtz Equation has two main drawbacks:

- In order to obtain highly accurate solutions, the mesh has to be fine enough to include a minimum number of elements per wavelength, see Equation (3.5). High frequencies lead to small values of the wavelengths and, thus, to very fine meshes, with a large number of nodes and unknown coefficients. This phenomena is further amplified when large domains are considered. Under these conditions, the computational cost involved in the solution of the system of equations becomes unacceptable, and the method is in practice restricted to low frequencies.

- For high frequency problems, the wave number, see Equation (3.4), of the numerical solution obtained using the finite element method with piecewise polynomials differs from the wave number of the analytical solution. This is called pollution error Babuška and Sauter (1997); Ihlenburg (1998); Deraemaeker et al. (1999). In addition, this discrepancy grows with the frequency, and the only way to mitigate it is by using extremely fine meshes. This leads to unaffordable computational costs for high-frequency problems in large domains.

In conclusion, the Finite Element Method is an excellent method for solving the Helmholtz equation for low frequencies and domains with moderate sizes, while it has serious difficulties when dealing with high frequency problems or large domains. See Ihlenburg (1998) for more details on the finite element method applied to acoustic problems.

3.2.4.4 Enriched Finite Element Methods

More recently, novel FEM approaches have been developed by enriching or even substituting the classical piecewise polynomial Galerkin approximation by sets of plane waves, locally pasted at the nodes of the mesh. The inclusion of plane waves introduces *a priori* physical and mathematical information of the problem into the space of solutions, since they reliably reproduce the wavenumber, and they are solution of the governing equations. As a consequence, the pollution error is drastically reduced. Despite the oscillatory behavior of the functions, the integration of the system matrix components can be overcome in an affordable manner by developing specific semi-analytical rules. These enriched methods relieve the requirement of having several mesh elements per wavelength, allowing the use of coarser meshes and reducing, thus, the number of degrees of freedom and the size of the system of equations.

Several enriched formulations have been developed during the last decades for solving the Helmholtz equation. In most of them, the continuity between elements is weakly imposed. For instance, in the Ultra-Weak Variational Formulation (UWVF) Cessenat and Després (1998) the Helmholtz equation is decomposed into coupled subproblems for each element. In the Discontinuous Enrichment Method (DEM) Farhat et al. (2001, 2003, 2004); Tezaur and Farhat (2006); Massimi et al. (2008); Tezaur et al. (2014), the problem is globally solved and the plane waves are directly added to the classical polynomial shape functions. Continuity is weakly enforced by Lagrange multipliers.

On the contrary, the PUM is based on the Partition of Unity theory Melenk (1995); Babuška et al. (1995); Melenk and Babuška (1996); Babuška and Melenk (1997). The enriching plane waves are multiplied by the classical polynomial shape functions (hat functions) forming a partition of unity, rather than directly added to the base of solution, preserving the continuity of the basis Mayer and Mandel (1997); Laghrouche and Bettess (2000); Ortiz and Sanchez (2001); Laghrouche et al. (2002, 2003); Ortiz (2004); Perrey-Debain et al. (2004); Laghrouche et al. (2005); De Bel

et al. (2005); Strouboulis et al. (2006, 2008); Strouboulis and Hidajat (2006). **This thesis explores the feasibility of solving the underwater acoustic propagation problem by using the PUM enriched with plane waves.** Although the implementation of the PUM is very similar to the standard implementation of the FEM, and it can be easily adapted to any FEM mesh, its application to high frequency and large domains arises two challenges. The first one involves the numerical integration of highly oscillatory functions. In this thesis, this shortcoming is mitigated by using semi-analytical integration rules. The second one concerns the resulting ill-conditioned global system matrix. In this work, we alleviate this drawback by using a low-rank approximation of the matrices based on the singular value decomposition technique.

Chapter 4

2D model for underwater acoustics

This chapter presents a new 2D numerical model to predict the underwater acoustic propagation using the Partition of Unity Method (PUM) enriched with plane waves. The aim of this model is to obtain sound pressure level distributions when multiple operational noise sources are present, in order to assess the acoustic impact on the marine fauna. It takes advantage of the suitability of the PUM for solving the Helmholtz equation, especially in the practical case of large domains and medium frequencies. The seawater acoustic absorption and the acoustic reflectance of the sea surface and the sea bottom are explicitly considered, and Perfectly Matched Layers (PML) are placed at the lateral artificial boundaries to avoid spurious reflections. The model includes semi-analytical integration rules which are adapted to highly oscillatory integrands in order to reduce the computational cost of the integration step. In addition, we develop a novel strategy to mitigate the ill-conditioning of the elemental and global system matrices. Specifically, we compute a low-rank approximation of the local space of solutions, which in turn reduces the number of degrees of freedom, the CPU time and the memory footprint. Numerical examples are presented to illustrate the capabilities of the model and to assess its accuracy.

4.1 Introduction

The acoustic pollution due to anthropogenic activities in the oceans, such as seismic exploration, military sonar operation, commercial shipping, construction, oil and gas extraction or offshore energy generation, has a direct impact on marine ecosystems. Until recent years, there was a lack of knowledge on the environmental impact of the underwater noise, and even nowadays special efforts are focused on monitoring the underwater noise levels Nedwell et al. (2003); Ainslie et al. (2009), identifying and characterizing the effects of the noise on the marine endangered species Thomsen et al. (2006); Thomsen (2009), and establishing criteria to assess this impact The European Commission (2010). For instance, a high level of exposure produces behavioral changes, masking of sounds of interest, hearing losses and temporary or permanent injuries over the marine fauna. Therefore, a growing social concern on this issue materialized in several national and international agreements and regulations that identify the anthropogenic noise as a specific type of pollution Marine Mammal Commission (2007); OSPAR Commission and others (2005), and that plan to establish limits on the generated noise intensity The European Commission (2008). In particular, Descriptor 11 from the European Union Commission Decision 2010/477/EU requires future monitoring programs to assess the underwater noise with frequencies ranging between 10 Hz and 10 kHz.

In this context, underwater acoustic propagation models gain importance as they provide a priori spatial distributions of the sound levels in the region of interest, which are crucial in the elaboration of acoustic impact assessments Dekeling et al. (2013). This chapter focuses on the simulation of the propagation of the noise produced by multiple non-impulsive operational sources through 2D large domains (from hundreds of meters to several kilometers) at medium frequencies (from hundreds of Hz to a few kHz).

Several numerical methods have been developed to predict the sound pressure level under these conditions. For instance, range-dependent simplified methods Hazelwood and Connelly (2005) provide a first approximation by estimating the transmission loss due to the spreading and the seawater absorption. Methods based on a parabolic simplification of the Helmholtz equation produce better results even though they assume that energy propagates nearly horizontally, the speed of sound varies weakly and outgoing energy dominates backscattered energy Tappert (1977); Collins (1993). However, full wave models give more realistic results since the wave physics is considered

and no additional assumptions are made on the wave propagation behavior. When non-impulsive noise sources are addressed, full wave models consider the Helmholtz equation, which is the harmonic version of the wave equation. To this end, each input noise spectrum is decomposed into a set of harmonic frequency bands, and a single simulation is performed for each of them.

The Helmholtz equation leads to oscillatory solutions, which are poorly represented by the classical polynomial shape functions associated with the standard finite element method (FEM), unless the mesh is extremely fine and then computationally unaffordable. Moreover, for high wavenumber applications, the numerical dispersion makes the discrete wavenumber differ from that of the exact solution. This effect is also called pollution error, and separates the solution of the standard FEM from the best approximation Babuška and Sauter (1997) (Ihlenburg, 1998, Section 4.6) Deraemaeker et al. (1999). Alternative finite element formulations have been developed to overcome this shortcoming by including enriching functions into the approximation space. These enriching functions include *a priori* knowledge of the solution and provide better local approximation properties. This also improves the accuracy of the global approximation. In the case of the Helmholtz equation, it is advantageous to include sets of plane waves propagating in different directions Melenk (1995); Melenk and Babuška (1996); Babuška and Melenk (1997), which form c-complete sets of functions for this equation Herrera and Sabina (1978). Plane waves are free-space natural solutions if a uniform wavenumber is considered, and practically eliminate the pollution error Babuška and Melenk (1997). In addition, this alleviates the constraint of having a minimum number of elements per wavelength (typically 10 or 12 as a rule of thumb), allowing the use of coarser meshes with several wavelengths per element, and providing a considerable reduction in the total number of unknowns (more than 90% in some cases Perrey-Debain et al. (2004)).

Enriched formulations have been recently incorporated to several approaches for the solving of the Helmholtz equation Wang et al. (2012). The Ultra-Weak Variational Formulation (UWVF) and the Discontinuous Enrichment Method (DEM) are examples of discontinuous enriched methods in which continuity between elements is weakly imposed. In the UWVF the Helmholtz equation is decomposed into coupled subproblems for each element Cessenat and Després (1998); Huttunen et al. (2002), while in the DEM continuity is weakly enforced by means of Lagrange multipliers Farhat et al. (2001, 2003). Here, we follow the partition of unity method (PUM)

with plane waves, which is based on the partition of the unity theory Melenk (1995); Babuška et al. (1995); Melenk and Babuška (1996); Babuška and Melenk (1997). It combines the good local approximation properties of the plane waves with the standard polynomial shape functions, that ensure continuity between elements.

The PUM has been extensively applied to diffraction and scattering problems Mayer and Mandel (1997); Laghrouche and Bettess (2000); Ortiz and Sanchez (2001); Laghrouche et al. (2002, 2003); Ortiz (2004); Perrey-Debain et al. (2004); Laghrouche et al. (2005); De Bel et al. (2005); Strouboulis and Hidajat (2006). However, in this work we explore a novel application of the method by developing a numerical model to simulate the underwater noise propagation. The seawater absorption phenomenon is included through the imaginary part of the wavenumber. Our model considers non-uniform acoustic properties for the seawater and the sea bottom. We model the behavior of the sea bottom and surface by means of the Robin boundary equation, with a complex transmission coefficient. Additionally, we place perfectly matched layers (PMLs) at the artificial boundaries, in order to avoid numerical reflections.

The introduction of plane waves in the basis of the approximation space increases the accuracy and reduces the number of degrees of freedom of the problem, thanks to the oscillatory behavior of the functions. Nevertheless, this provokes an undesirable rise in the CPU time required for the integration step, if a standard Gauss-Legendre rule is selected, as in the first implementations of the method Laghrouche and Bettess (2000); Laghrouche et al. (2002, 2003); Perrey-Debain et al. (2004); Laghrouche et al. (2005). The reason is that a large number of integration points is required to capture the highly oscillatory integrands. In Ortiz and Sanchez (2001); Ortiz (2004) a local coordinate rotation was introduced in order to develop a problem-adapted semi-analytical integration rule. Later, Strouboulis and Hidajat (2006) applied the Filon's rule to evaluate the integrals over rectangular elements. In this work, we follow the semi-analytical approach developed in Bettess et al. (2003); Sugimoto et al. (2003), which is valid for first order triangular and quadrilateral elements.

Several authors have reported ill-conditioning of the resulting matrices when sets of plane waves are considered as part of the approximation functions Melenk (1995); Melenk and Babuška (1996); Babuška and Melenk (1997); Mayer and Mandel (1997); Ortiz and Sanchez (2001); Laghrouche et al. (2002); Perrey-Debain et al. (2004); Wang et al. (2012). In order to reduce the condition number of the elemental matrices, we perform a low-rank approximation of the local basis functions. To this end, we first

compute the volume integrals of the weak form over a standard domain patch. Then, we compute the singular values of the corresponding matrix, and truncate the smallest ones. This contribution improves the conditioning of the system matrix and reduces the number of degrees of freedom and, hence, the required computational resources.

The remainder of this chapter is organized as follows. In Section 4.2 we introduce our physical model, setting up the problem and detailing how the physical phenomena are considered. In Section 4.3 we focus on the numerical formulation. Specifically, we detail the semi-analytical integration procedure used to compute the elemental contributions, and a technique providing a low-rank approximation based on the singular value decomposition (SVD). Several numerical example are presented in Section 4.4, to illustrate the applicability and accuracy of the proposed method. Finally, Section 4.5 includes some concluding remarks and developments to be addressed in a next step of the research.

4.2 Modelization of the underwater noise propagation

In order to develop a model for the propagation of the underwater noise we assume that the speed of ocean waves and water masses are both small (around several meters per second) compared to the sound speed in water (approximately 1500 m/s). Hence, our model neglects water motion and assumes a completely still medium Kuperman and Lynch (2004) and a still and plane sea surface, see Section 4.2.3. Accordingly, acoustics and fluid dynamics are uncoupled.

For the European offshore wind farms the characteristic water depth varies between 20 m and 200 m, depending on the structural type of the turbine, while their characteristic length scale is a few kilometers Arapogianni et al. (2013). Thus, the overall shape of the domain is nearly rectangular, with the horizontal dimension much larger than the vertical one. In our two-dimensional model, the domain consists of an area enclosed by the sea surface (assumed planar), two artificial lateral boundaries, and the sea bottom, which at the working scale is usually smooth with slight slopes.

We assume stationary harmonic noise sources. In practice, input noise spectra are decomposed into a set of frequency bands, each of them characterized by a reference frequency (and a corresponding wavenumber). Then, the Helmholtz equation can be considered to compute a numerical solution for each of the single frequency bands,

independently. Finally, a sound pressure level spectra distribution is generated after collecting the results for each band.

4.2.1 Problem statement

The unknown complex pressure, p, takes values in Ω and is the solution of the boundary value problem

$$\begin{aligned} \Delta p + k^2 p &= 0 \quad \text{in } \Omega, \\ \frac{\partial p}{\partial n} - \tau k p &= g \quad \text{in } \Gamma = \partial\Omega, \end{aligned} \tag{4.1}$$

where Δ is the Laplace operator, k is the wavenumber (see Section 2.1.3.1), n is the outward unit normal, τ is the complex transmission coefficient (see Section 4.2.3), and g is the independent term that we will use to introduce the input noise sources (see Section 4.2.4).

The corresponding weak form of the problem is stated as: find $p \in H^1(\Omega)$ such that

$$\mathcal{B}(p, v) = \mathcal{L}(v) \qquad \forall v \in H^1(\Omega), \tag{4.2}$$

where

$$\mathcal{B}(p, v) = \int_\Omega (k^2 p\bar{v} - \nabla p \cdot \nabla \bar{v}) \, \mathrm{d}\Omega + \int_\Gamma \tau k p \bar{v} \, \mathrm{d}\Gamma \tag{4.3}$$

$$\mathcal{L}(v) = -\int_\Gamma g\bar{v} \, \mathrm{d}\Gamma, \tag{4.4}$$

being $H^1(\Omega)$ the space of functions with square-integrable derivatives in Ω, and $\bar{\cdot}$ the conjugate of a complex variable.

4.2.2 Seawater absorption and complex wavenumber

The geometrical spreading, that is the attenuation of the intensity when the wave propagates away from the acoustic source, is implicitly accounted for in the elliptic nature of the Helmholtz equation. However, empirical evidence reveals that seawater is a damping medium. The additional attenuation associated with physical-chemical reactions is caused by two groups of phenomena that convert acoustic energy into heat: the shear and volume viscosities effects, and a series of ionic relaxation processes involving, mainly, magnesium sulfate $MgSO_4$ and boric acid $B(OH)_3$. The energy loss

is modeled with the logarithmic absorption coefficient α, which is estimated using the formula proposed in Ainslie and McColm (1998) (Section 2.1.3.1).

The absorption is accounted for in our model by considering a complex wavenumber $k = k_1 + ik_2$, $i = \sqrt{-1}$. The real part of the wavenumber is standard in wave theory: $k_1 = 2\pi f/c$, f being the wave frequency and c the sound speed (Section 2.1.2). The imaginary part, k_2, introduces an omni-directional attenuation of the solution that is proportional to the absorption coefficient α. In order to deduce the relation between them, a plane wave with an arbitrary amplitude A is considered, propagating in a free space following an arbitrary direction vector $\mathbf{e}$. It suffers an exponential decay determined by k_2,

$$W(\mathbf{x}) = A\exp(ik\,\mathbf{e}\cdot\mathbf{x}) = A\exp(-k_2\,\mathbf{e}\cdot\mathbf{x})\,\exp(ik_1\,\mathbf{e}\cdot\mathbf{x}). \tag{4.5}$$

Thus, the absorption coefficient and according to equations (2.1) and (4.5), the transition loss between two points separated a distance r (in km) produced exclusively by the physical absorption is

$$\alpha r = \mathrm{SPL}_0 - \mathrm{SPL}_r = 20\log_{10}\frac{p_{\mathrm{rms},0}}{p_0} - 20\log_{10}\frac{p_{\mathrm{rms},r}}{p_0} = 20\log_{10}[\exp(k_2\cdot 1000\,r)]\ .$$

Hence,

$$k_2 = \frac{\ln 10}{20\cdot 1000}\ \alpha,$$

where k_2 is measured in rad/s and α in dB/km.

4.2.3 Boundary conditions

The boundary condition, Equation (4.1), models the behavior of the solution at different parts of the boundary (sea surface, sea bottom, and lateral artificial boundaries). The dimensionless transmission coefficient τ is related to the rate of transfer of energy at the corresponding boundary Isaacson and Qu (1990), and it allows prescribing fully reflecting ($\tau = 0$), non-reflecting ($|\tau| = 1$) or partially reflecting ($0 < |\tau| < 1$) boundary conditions Berkhoff (1976).

Depending on the availability of empirical measurements, the value of the transmission coefficient can be obtained either from the transmission loss at the interface TL_i, measured in dB, or from the acoustic impedance of the boundary $Z_b = \rho_b c_b$, being ρ_b the density of the boundary material, see Appendix B for more details. In the first case, we have

$$\tau = i\frac{1-10^{-\mathrm{TL}_i/20}}{1+10^{-\mathrm{TL}_i/20}}. \tag{4.6}$$

In the second case, we have

$$\tau = i\frac{Z_{sw}}{Z_b}, \tag{4.7}$$

where $Z_{sw} \approx 1.54 \times 10^6$ kg/(m^{2}s) is the acoustic impedance of the seawater.

Note that we can reproduce full reflection (Neumann boundary conditions) by setting $\tau = 0$ ($\mathrm{TL}_i = 0$ or $Z_b >> Z_{sw}$), and null reflection (0-order absorbing boundary conditions) by setting $\tau = i$ ($\mathrm{TL}_i \to \infty$ or $Z_{sw} = Z_b$).

The sea surface behaves as a reflector when it is smooth, due to the large acoustic impedance contrast, and as a scatterer when it is rough. The sea surface is treated as plane and fully reflective ($\tau = 0$), being a conservative assumption with respect to all possible sea states.

On the contrary, the impedance mismatch between the seawater and sea bottom materials is less severe and, hence, the sea bottom is considered as a partially reflecting and scattering boundary. Its acoustic properties depend, for instance, on the multi-layered composition of the materials, the frequency and the angle of incidence, see details in (Urick, 1983, Section 5.8) and (Burdic, 1983, Section 5.3).

The lateral boundaries are artificial entities that truncate the unbounded domain and, hence, they should behave as non-reflecting boundaries. Several absorbing boundary conditions (ABC) perform well for some propagation directions, but introduce spurious reflections for others. Higher order ABCs are more accurate but also more complex and demanding in terms of storage and calculation time Rappaport (1995). Here, Perfectly Matched Layers (PMLs) are adopted in order to achieve full absorbing conditions and avoid spurious reflections Berenger (1994). PMLs are analytic continuations of the Helmholtz equation into complex spatial coordinates, see Johnson (2007). The PML technique assumes homogeneous medium properties along the normal to the boundary. In order to simplify the formulation, the lateral boundaries are taken parallel to the axes. Modesto et al. (2015) successfully applied PML layers to harbor agitation problems.

4.2.4 Noise generation

Note that the size of the sound sources (wave energy generators, wind turbines, or other elements) is small compared to the size of the domain. Moreover, the region of interest is usually placed at distances equal to several times their characteristic size. Hence, we assume that noise sources are punctual and located on the surface.

The input noise is introduced via the analytical solution of the pressure field generated by a point source with the hypothesis of a uniform wavenumber k_0. This pressure field is introduced into the Robin boundary equation (4.1) and, then, the resulting independent term g is integrated along the boundary edges of the adjacent elements. Specifically, the pressure field p_a produced by a point source in a homogeneous 2D medium can be approximated by (see (Kinsler et al., 1999, Chapt. 5))

$$p_a(\mathbf{x}) = p_{\mathbf{x_0}} \left(\frac{r(\mathbf{x_0})}{r(\mathbf{x})} \right)^{1/2} \exp\Big(ik_0 \big(r(\mathbf{x}) - r(\mathbf{x_0}) \big) \Big), \tag{4.8}$$

where $\mathbf{x}$ is the spatial coordinates vector, $p_{\mathbf{x_0}}$ is the pressure produced by the source at a reference point $\mathbf{x_0}$, and $r(\cdot)$ is the distance to the point source $\mathbf{x}_s$. Hence, according to Equation (4.1),

$$\begin{aligned} g(\mathbf{x}) &= \frac{\partial p_a(\mathbf{x})}{\partial n} - k(\mathbf{x})\tau(\mathbf{x}) p_a(\mathbf{x}) \\ &= \left(\frac{ik_0 r(\mathbf{x}) - 1/2}{r^2(\mathbf{x})} \, (\mathbf{x} - \mathbf{x_s}) \cdot \mathbf{n} - k(\mathbf{x})\tau(\mathbf{x}) \right) p_a(\mathbf{x}) \ . \end{aligned} \tag{4.9}$$

Note that the source point must be separated from the surface since there is a singularity point at $r(\mathbf{x}_s) = 0$. Numerical experiments demonstrate that a distance of $\lambda/3$ from the sea surface is sufficient, where $\lambda = 2\pi/k$ is the wavelength.

Multiple noise sources are easily introduced invoking the linearity of the problem and the superposition principle.

4.3 Numerical model

4.3.1 Partition of Unity Method

The boundary value problem defined by Equation (4.2) is solved using the Partition of Unity Method (PUM). Domain Ω is discretized using a quadrilateral mesh with characteristic size h, see Section 4.3.2, and a total number of nodes n_{nod}. N_m, for $m = 1, \ldots, n_{\text{nod}}$, denotes the classical piecewise bilinear shape function associated to the m-th node of the mesh. The support of N_m, ν_m, is a patch composed by the elements sharing node m.

The partition of unity space $\mathcal{W}_{h,q}$ reads

$$\mathcal{W}_{h,q} = \left\{ v \,\middle|\, v = \sum_{m=1}^{n_{\text{nod}}} N_m \left(\sum_{r=1}^{q} a_{m,r} W_{m,r} \right) \right\}, \tag{4.10}$$

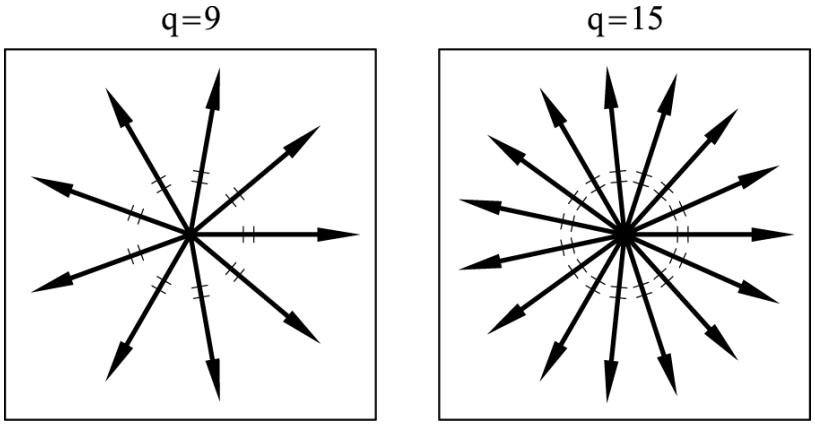

Figure 4.1: Examples showing possible directions of the 2D plane waves enriching functions employed at each node.

where q is the number of plane waves (enrichment functions) pasted at the m-th node (patch), $a_{m,r}$ is the complex coefficient (amplitude) of the r-th plane wave associated to the m-th node, namely

$$W_{m,r}(\mathbf{x}) = \exp\big(ik_m\, \mathbf{e_r} \cdot (\mathbf{x} - \mathbf{x_m})\big), \tag{4.11}$$

being k_m the wavenumber at the m-th node, $\mathbf{e_r} = \big(\cos(\theta_r), \sin(\theta_r)\big)$ the r-th propagation direction, $\theta_r = (2\pi r)/q$ the counterclockwise angle with respect to the x axis, and $\mathbf{x_m}$ the coordinates of the m-th node. Figure 4.1 depicts two examples of sets with equidistributed directions for the plane waves.

Remark 4.1. *Functions N_m, for $m = 1, \ldots, n_{nod}$, are a partition of the unity*

$$\sum_{m=1}^{n_{nod}} N_m \equiv 1 \quad \text{on } \Omega.$$

In addition, N_m and their derivatives are bounded. Under these conditions, the local approximation properties of the enrichment functions are inherited by the global space of solutions, see details in Melenk (1995); Babuška et al. (1995); Melenk and Babuška (1996).

Remark 4.2. *In several applications with plane wave enrichment functions, the standard finite element polynomial approximation space is kept in the definition of the solution space Strouboulis et al. (2006, 2008). That is, Equation* (4.10) *is replaced by*

$$\mathcal{W}_{h,q} = \left\{ v \,\middle|\, v = \sum_{m=1}^{n_{nod}} b_m N_m + \sum_{m=1}^{n_{nod}} N_m \left(\sum_{r=1}^{q} a_{m,r} W_{m,r} \right) \right\}. \tag{4.12}$$

Here, we adopt the approach presented in Melenk and Babuška (1996); Mayer and Mandel (1997); Laghrouche and Bettess (2000); Ortiz and Sanchez (2001); Laghrouche et al. (2002); Ortiz (2004); Laghrouche et al. (2005); Strouboulis and Hidajat (2006) that only considers the part of the approximation space including the planar waves (we assume $b_m = 0$ in Equation (4.12)). This is supported by two reasons. First, the enhanced rate of convergence is given by the contribution of the plane wave basis, rather than the polynomials Ortiz (2004). Second, we deal with pressure fields that a priori *have null average.*

Remark 4.3. *Although it is possible to use high-order finite element shape functions, we consider bilinear polynomials, following the rationale of Remark 4.2. Moreover, this also simplifies the semi-analytical integration rules to compute the elemental contributions.*

Remark 4.4. *The definition of the enrichment functions* (4.11) *is local. Thus, it is possible to paste different sets of plane waves at each node patch. We take advantage of this property to incorporate non-uniform distributions for the sound speed (wavenumber). The wavenumber evaluated at the m-th node is assigned to the plane waves pasted at the m-th patch. Note that the k_m value applies to the whole patch, thus, it is assumed that the spatial gradient of the sound speed is smooth.*

The PUM solution of the weak problem, Equation (4.2), is defined as follows. Find $p_{h,q} \in \mathcal{W}_{h,q}$ such that

$$\mathcal{B}(p_{h,q}, v) = \mathcal{L}(v) \qquad \forall v \in \mathcal{W}_{h,q}.$$

According to Equation (4.10), the PUM approximation has the form

$$p_{h,q}(\mathbf{x}) = \sum_{m=1}^{n_{\text{nod}}} \sum_{r=1}^{q} a_{m,r} \phi_{m,r}(\mathbf{x}), \tag{4.13}$$

where $\phi_{m,r}$ is the approximation function associated to the m-th node and the r-th direction,

$$\begin{aligned} \phi_{m,r}(\mathbf{x}) &= N_m(\mathbf{x}) W_{m,r}(\mathbf{x}) \\ &= N_m(\mathbf{x}) \exp\left(ik_m \, \mathbf{e_r} \cdot (\mathbf{x} - \mathbf{x_m})\right). \end{aligned} \tag{4.14}$$

The procedure is similar to the standard finite element method scheme. Here, the terms to be integrated include harmonic functions and, therefore, the corresponding

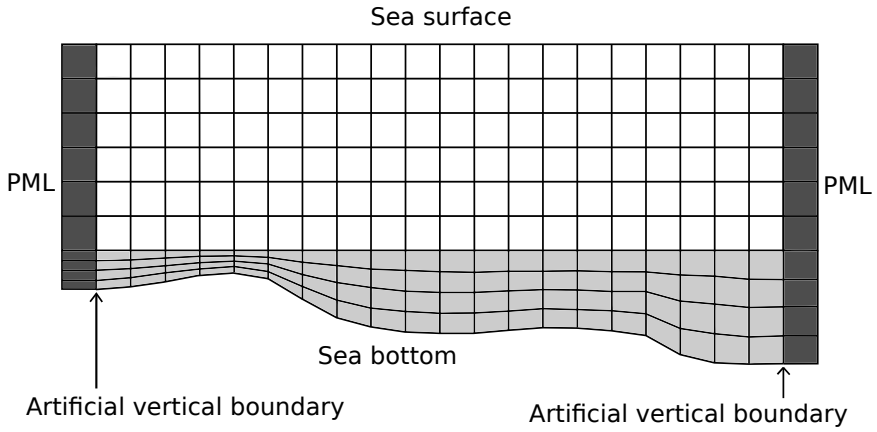

Figure 4.2: Example of a two-dimensional mesh of quadrilaterals, with PMLs at the artificial vertical boundaries.

elementary matrices and vectors are integrated using specific semi-analytical integration rules (see Section 4.3.3), and assembled in the global matrix and right-hand side vector. Then, the algebraic complex linear system is solved numerically. Finally, a specific post-processing has to be efficiently applied on the resulting solution vector to recover the pressure field, Equation (4.13).

4.3.2 Domain discretization

The computational domain is the sea area enclosed by 3 straight segments (the planar sea surface and 2 lateral artificial boundaries defined by the PML layers) and a smooth sea bottom curve. Therefore, the domain is quasi-rectangular and can be easily discretized using quadrilateral elements. First, a preliminary structured grid of rectangles is generated. Second, the lower rows of elements are adapted to fit the bottom. Thus, the resulting meshes are composed of 3 types of elements (see Figure 4.2): rectangular geometrically identical non-PML elements (white elements), quadrilateral non-PML elements (gray elements), and rectangular PML elements (dark gray elements). We will take advantage of theses structured meshes during the computation of the integrals involved in the element contributions of the weak form (4.2), see Section 4.3.3.

Two factors determine the target element size h: the number of waves per element and the characteristic bathymetric length, that is, the length associated to the roughness of the sea bottom definition. For low-frequency simulations (below

approximately 100 Hz), the wavelength is longer than the characteristic bathymetric lengths and the mesh coarseness is limited by the bathymetry. On the contrary, for higher frequencies, the element size is limited by the desired number of wavelengths per element size.

4.3.3 Numerical integration

The approximation functions proposed by the PUM enriched with plane waves are adapted to the nature of the solution. Thus, the enriched approximation space allows a drastic reduction of the pollution error, see Babuška and Sauter (1997) and (Ihlenburg, 1998, Section 4.8) for a detailed analysis. The number of degrees of freedom is also reduced because the same accuracy is reached with coarser meshes. However, due to the highly oscillatory behavior of the resulting integrands, a high number of integration points (up to 120 × 120 points according to Laghrouche and Bettess (2000); Laghrouche et al. (2005)) is needed to compute the elemental contributions, if a standard Gauss-Legendre rule is applied. Therefore, the integration cost becomes prohibitive if high frequencies or large domains are considered unless a more efficient quadrature, particularly devised for this case, is used.

In our model, three kinds of highly oscillatory integrals are evaluated in order to compute the element contributions. We classify them into two groups. In the first group, we have the integrals involved in the computation of the form $\mathcal{B}(p, v)$, see Equation (4.3). These two integrals are finite Fourier transform type, with a smooth non-oscillatory part and a highly oscillatory complex exponential part. In the second group, we have the integral involved in the computation of the linear operator $\mathcal{L}(v)$, see Equation (4.4), where the integrand is the product of two highly oscillatory terms.

In the first group of integrals, we have to evaluate the volume integral matrix (the first term in Equation (4.3)). The contribution of the e-th element is

$$\begin{aligned} K^{(e)}_{mr,ns} &= \int_{\Omega^{(e)}} [k^2 \phi_{n,s} \bar{v}_{m,r} - \nabla\phi_{n,s} \cdot \nabla\bar{v}_{m,r}] \, \mathrm{d}\Omega \\ &= \exp\left[i(\bar{k}_m \mathbf{e_r} \cdot \mathbf{x_m} - k_n \mathbf{e_s} \cdot \mathbf{x_n})\right] \int_{\Omega^{(e)}} F_{mr,ns} \, \psi_{mr,ns} \, \mathrm{d}\Omega \end{aligned}$$

where $\phi_{n,s}$, and $v_{m,r}$ are defined according to Equation (4.14), $m, n = 1, \ldots, n_{\mathrm{nod}}$, and $r, s = 1, \ldots, q$,

$$F_{mr,ns} = k^2 N_m N_n - (\nabla N_m - i\bar{k}_m N_m \mathbf{e_r}) \cdot (\nabla N_n + i k_n N_n \mathbf{e_s})$$

is a non-oscillatory term, and

$$\psi_{mr,ns} = \exp\left(i(-\bar{k}_m \mathbf{e_r} + k_n \mathbf{e_s}) \cdot \mathbf{x}\right) \tag{4.15}$$

is a highly oscillatory term.

Similarly, the contribution of the e-th element to the boundary integral matrix (the second term in equation (4.3)) is

$$B^{(e)}_{mr,ns} = \int_{\Gamma^{(e)}} \tau k \phi_{n,s} \bar{v}_{m,r} \, \mathrm{d}\Gamma = \exp\left[i(\bar{k}_m \mathbf{e_r} \cdot \mathbf{x_m} - k_n \mathbf{e_s} \cdot \mathbf{x_n})\right] \int_{\Omega^{(e)}} F_{mr,ns} \, \psi_{mr,ns} \, \mathrm{d}\Gamma, \tag{4.16}$$

where

$$F_{mn,rs} = \tau k N_m N_n$$

is the non-oscillatory term and $\psi_{mr,ns}$ is given by Equation (4.15).

To compute the integrals in Equations (4.15) and (4.16) we have to evaluate expressions of the type

$$I = \int_{\mathbf{X}} F_{mr,ns}(\mathbf{x}) \, \psi_{mr,ns}(\mathbf{x}) \, \mathrm{d}\mathbf{X}$$

where $\mathbf{X}$ is a 1D or a 2D domain. To this end, we use the semi-analytical quadratures developed in Bettess et al. (2003); Sugimoto et al. (2003). In these rules, the non-oscillatory term of the integrands is approximated by a set of n_{lp} Lagrangian polynomials,

$$F_{mr,ns}(\mathbf{x}) \approx \sum_{p=1}^{n_{\mathrm{lp}}} F_{mr,ns}(\mathbf{x}_p) L_p(\mathbf{x}), \tag{4.17}$$

where $\mathbf{x}_p$, $L_p(\mathbf{x})$ are the p-th interpolation point and its associated Lagrange polynomial, respectively. Therefore, we have

$$\begin{aligned} I &= \sum_{p=1}^{n_{\mathrm{lp}}} F_{mr,ns}(\mathbf{x}_p) \int_{\mathbf{X}} L_p(\mathbf{x}) \psi_{mr,ns}(\mathbf{x}) \, \mathrm{d}\mathbf{X} \\ &= \sum_{p=1}^{n_{\mathrm{lp}}} F_{mr,ns}(\mathbf{x}_p) \, w_{mr,ns;p} \end{aligned}$$

where

$$w_{mr,ns;p} = \int_{\mathbf{X}} L_p(\mathbf{x}) \psi_{mr,ns}(\mathbf{x}) \, \mathrm{d}\mathbf{X}. \tag{4.18}$$

are the integration weights. The key point in the rules proposed in Bettess et al. (2003); Sugimoto et al. (2003) is to perform an analytical integration for these integration weights.

Hence, the quality of the integrals (4.15) and (4.16) is determined by the quality of the approximation (4.17). Note that the non-oscillatory functions are evaluated at the interpolating points, whose spacing is determined by the behavior of this functions rather than by the highly oscillatory full integrand, resulting in a moderate amount of points and function evaluations, compared to the scheme with the Gauss-Legendre rules. The location of the integration points could be optimally selected but it would change from one element to the other, thus, a equally spaced distribution of integration points is used. In our implementation we use 4 equally distributed integration points per axis, giving 16 points per quadrilateral element. The proposed quadrature is exact for $F_{mr,ns}(\mathbf{x})$ being any polynomial of degree less or equal to 3.

In the second group of integrals, we have to compute the element contribution of the independent term g of the Robin equation (noise generation) along the boundary edges surrounding the noise sources, see Equation (4.10),

$$f_{mr}^{(e)} = \int_{\Gamma^e} g\bar{v}_{m,r}\,\mathrm{d}\Gamma = \exp(i\bar{k}_m \mathbf{e_r}\cdot\mathbf{x_m}) \int_{\Gamma^e} \underbrace{g(\mathbf{x})N_m(\mathbf{x})}_{\text{highly oscillatory}}\ \underbrace{\exp\big(-i\bar{k}_m\mathbf{e_r}\cdot\mathbf{x}\big)}_{\text{highly oscillatory}}\,\mathrm{d}\Gamma. \quad (4.19)$$

Since function g is highly oscillatory the semi-analytical methods previously proposed are less competitive (the computational cost involved in the evaluation of a large number of integration weights (4.18) is high). Consequently, we use a standard high order Gauss-Legendre rule to compute Equation (4.19) using 10 integration points per wavelength.

Remark 4.5. *The integration step in the PUM has a larger impact on the CPU time, with respect to the standard FEM. The computational cost of the integration of the volume integrals $K_{mr,ns}^{(e)}$ can be reduced if the geometrical properties of the domain discretization are considered. Since each layer of the upper region of the mesh is composed of elements that are geometrically identical, and if the physical parameters of the elements are the same (sound speed and absorption coefficient), the elemental matrices can be reused for several elements, reducing drastically the CPU time involved in the simulation.*

4.3.4 Basis reduction technique in order to improve conditioning

Several authors have reported ill-conditioning of the resulting matrices when sets of plane waves are considered as part of the approximation functions Melenk (1995);

Melenk and Babuška (1996); Babuška and Melenk (1997); Mayer and Mandel (1997); Ortiz and Sanchez (2001); Laghrouche et al. (2002); Perrey-Debain et al. (2004); Wang et al. (2012). In order to reduce the condition number of the elemental matrices, we perform a low-rank approximation of the local basis functions. To this end, we first compute the volume integrals of the weak form over a standard domain patch. Then, we compute the singular values of the corresponding matrix, and truncate the smallest ones. This contribution improves the conditioning of the system matrix and reduces the number of degrees of freedom and, hence, the required computational resources.

It is well known that the element matrices, equations (4.15) and (4.16) and, therefore, the corresponding global matrix obtained by the PUM method are ill-conditioned, when the solution space is enriched by a set of plane waves Mayer and Mandel (1997); Ortiz and Sanchez (2001); Laghrouche et al. (2002). To mitigate this drawback, we devise a low-rank approximation of the local functional discretisation space discarding the redundant elements of the basis and keeping the relevant terms, associated with the highest singular values provided by the Singular Value Decomposition (SVD). This is a natural approach, already mentioned as a promising possibility in Perrey-Debain et al. (2004), worthy to be explored. Specifically, we propose a novel low-rank approximation of the local enrichment basis, in the context of the PUM enriched with plane waves. The approximation is obtained by applying the SVD to identify and truncate the smallest singular values of the matrix corresponding to a standard patch. This introduces a linear transformation of the local solution and local test spaces, leading to a new number $\tilde{q}$ of approximation functions per node, and reduces the size of the system of equations. As a consequence, a large saving in the computational cost (both in terms of CPU time and memory footprint) is produced.

The low-rank approximation is computed with the following procedure. First, a standard patch (set of elements sharing a node) is defined using the physical properties of a rectangular element of the upper rows of the discretization (white elements in Figure 4.2), and a uniform sound speed is set as an average of the vertical sound speed profile. Then, the approximation functions associated with the patch (to the inner node of the patch) are integrated according to (4.15). The SVD is then applied to the resulting $q \times q$ matrix:

$$\mathbf{K}^{\text{patch}} = \mathbf{U}\boldsymbol{\Delta}\mathbf{V}^{*},$$

where the $q \times q$ diagonal matrix $\boldsymbol{\Delta}$ contains non-negative real numbers, the singular

values of $\mathbf{K}^{\text{patch}}$, $\mathbf{U}$, $\mathbf{V}$ are $q \times q$ unitary matrices, and * denotes conjugate transpose.

Remark 4.6. *If seawater absorption is not considered, the wavenumber k is real. Thus, matrix $\mathbf{K}^{patch}$ is hermitian, see Equation (4.3). In this case $\mathbf{U} = \mathbf{V}$. However, for the general case, the wavenumber k is complex, and $\mathbf{K}^{patch}$ is no longer hermitian.*

Let $\delta_{max} = \max\{\delta_i\}$ for $i = 1, \ldots, q$ be the maximum singular value. We select those singular values that verify

$$\frac{\delta_i}{\delta_{max}} \geq \varepsilon \approx \frac{1}{\kappa(\mathbf{K}^{\text{patch}})}, \tag{4.20}$$

being ε a given tolerance and $\kappa(\cdot)$ the condition number. We define the square reduced diagonal matrix $\tilde{\mathbf{\Delta}}_{\tilde{q}\times\tilde{q}}$, including the largest $\tilde{q}$ singular values of $\mathbf{\Delta}$, and the rectangular reduced matrices $\tilde{\mathbf{U}}_{(q\times\tilde{q})}$ and $\tilde{\mathbf{V}}_{(q\times\tilde{q})}$, composed by the corresponding $\tilde{q}$ columns of the matrices $\mathbf{U}$ and $\mathbf{V}$, respectively. Therefore, matrix $\mathbf{K}^{\text{patch}}$ is approximated by

$$\mathbf{K}^{\text{patch}}_{(q\times q)} \approx \tilde{\mathbf{U}}_{(q\times\tilde{q})}\tilde{\mathbf{\Delta}}_{(\tilde{q}\times\tilde{q})}\tilde{\mathbf{V}}^*_{(\tilde{q}\times q)},$$

where $\tilde{\mathbf{U}}$ and $\tilde{\mathbf{V}}$ are the linear transformation matrices from the original spaces of test functions and approximation functions to the reduced ones, respectively.

We highlight that the CPU time involved in this procedure is moderate since the SVD and the transformation matrices are computed once for a generic patch, and the impact on the CPU time of the remaining operations is negligible.

From a practical point of view, the elemental matrices and independent term vectors are integrated for the original approximation and test functions in order to take profit of the semi-analytical rules presented in Section 4.3.3. After that, the following transformations are applied over the nodal blocks $\mathbf{K}^{(e)}_{(m,n)}$ and $\mathbf{f}^{(e)}_{(m)}$, before the assembly:

$$\begin{aligned} \tilde{\mathbf{K}}^{(e)}_{(m,n)} &= \tilde{\mathbf{U}}^*\mathbf{K}^{(e)}_{(m,n)}\tilde{\mathbf{V}}, \\ \tilde{\mathbf{f}}^{(e)}_{m} &= \tilde{\mathbf{U}}^*\mathbf{f}^{(e)}_{m}, \end{aligned}$$

for $m, n = 1, \ldots, 4$, and $e = 1, \ldots, n_{\text{elem}}$, being n_{elem} the number of elements.

Once the reduced system is solved, the transformation of the space of solutions is reverted in order to apply the original post-processing routines,

$$\mathbf{a}_{(m)} = \tilde{\mathbf{V}}\tilde{\mathbf{a}}_{(m)},$$

where $\mathbf{a}_{(m)}$ and $\tilde{\mathbf{a}}_{(m)}$ are the vectors containing the complex coefficients associated to the m-th node in the original (q components) and reduced ($\tilde{q}$ components) local approximation spaces, respectively.

4.4 Numerical experiments

In this section we present four examples that illustrate the capabilities and the behavior of the proposed method. First, we test our model by computing the free propagation (without the interaction of obstacles or boundaries) of the sound generated by a point source in a lossy medium. The second example analyzes the effect of having different sea bottom transmission coefficients on the computed pressure field. In the third example we compute the pressure field when the sound speed profile is non-uniform, and two noise sources are considered. Finally, we perform a sensitive analysis of the low-rank approximation of the local basis on the accuracy and the required computational resources.

In all the examples, the sea surface is assumed horizontal and fully reflective ($\tau = 0$). The noise sources generate a harmonic sound with an amplitude of 10 Pa (SPL = 137 dB, see Equation (2.1)) at a distance of 1 m. The attenuation parameter for the PMLs is equal to zero at the non-PML regions and grows 10 rad/s per wavelength at the PMLs. The local spaces of solutions contain an initial number of $q = 200$ plane waves per node before the basis reduction is performed. The sound speed is $c = 1,500$ m/s, except in the third example where a non-uniform sound speed is considered. No absorption is taken into account, except in the first example. It is worth to notice that the unknowns associated to the PML region are not included when reporting the total number of unknowns of each simulation. The spatial coordinates and lengths are expressed in meters. For this work, we have used the built-in direct solving algorithm `mldivide`, included in MATLAB R2013b.

4.4.1 Free propagation through a lossy medium

The objective of this example is to illustrate the accuracy of the proposed model when the seawater absorption is taken into account. We consider the free propagation field generated by a single point source through a half-plane. The domain is truncated creating a rectangular geometry $\Omega = [-500, +500] \times [-100, 0]$, and discretized using a rectangular mesh with 10 wavelengths per element, resulting in an element size of $(\Delta x, \Delta y) = (29.4, 25)$, and giving 26,775 DOFs ($\tilde{q} = 153$). The source is located at the center of the surface, $\mathbf{x} = (0, 0)$, and generates a noise with a frequency of $f = 500$ Hz. A layer of PML elements is added around the lateral artificial boundaries and below the sea bottom boundary, see Figure 4.3.

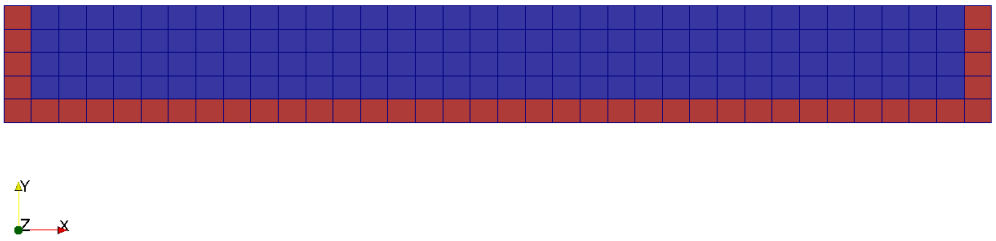

Figure 4.3: 2D mesh used in Example 1, including non-PML elements (in blue) and PML elements (in red).

Two cases are analyzed. First, we consider the case with null seawater absorption ($\alpha = 0$ dB/km). Second, to highlight the effects of the attenuation, we set $\alpha = 50$ dB/km, that in fact corresponds to the absorption produced at a higher frequency value of 100 kHz (see Figure 2.2 in Section 2.1.3.1).

Figures 4.4(a) and 4.5(a) show the real part of the pressure field and the sound pressure level, when null absorption is considered. Note that the decay in the sound pressure level caused by geometrical spreading is clearly recognizable in Figure 4.5(a). Figures 4.4(b) and 4.5(b) depict the same fields when the seawater absorption is considered. As expected, the solution includes an additional attenuation with respect to the solution without absorption. The additional attenuation associated with the seawater absorption is illustrated in Figures 4.4(c) and 4.5(c) plotting the evolution along the y-axis (for $y \in [-100, 0]$ at $x = 0$) of the real part of the pressure field and the sound pressure level, respectively.

Since the analytical solution p_a of this problem is given by Equation (4.8), we measure the accuracy of the numerical solution in two ways. First, we compute the point-wise relative error as the discrepancy with the analytical solution of the point source pressure field:

$$\varepsilon_{\text{pw}}(\mathbf{x}) = \frac{|p_{h,q}(\mathbf{x}) - p_a(\mathbf{x})|}{|p_a(\mathbf{x})|}, \tag{4.21}$$

where $p_{h,q}(\mathbf{x})$ is the numerical solution.

The maximum value of this relative error remains below 25%. Figure 4.6 shows this value in both cases. From this figure we realize that the highest values of the point-wise relative error are located in two regions. On the one hand, they are located near the sea surface and far of the input noise sources. This may be caused by the method used to introduce the input noise, since we integrate the independent term

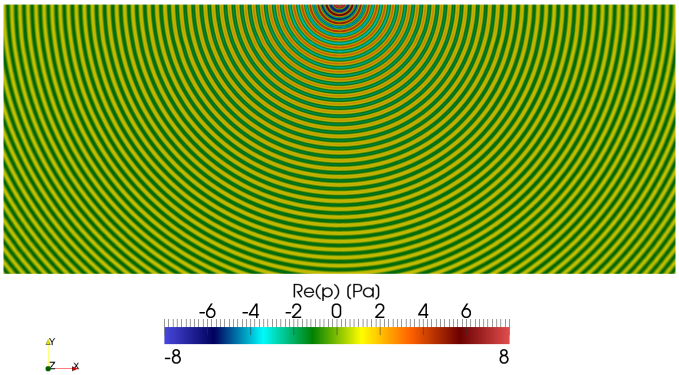

(a)

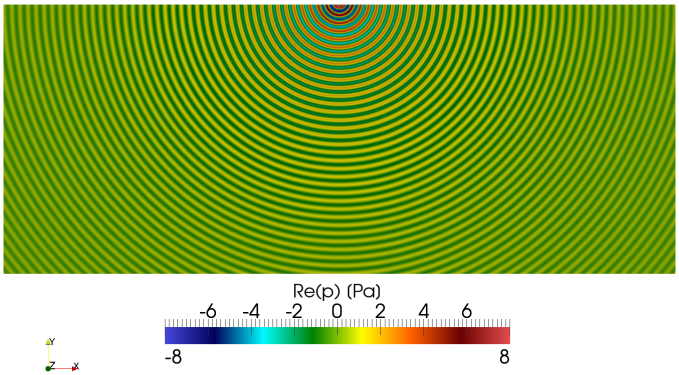

(b)

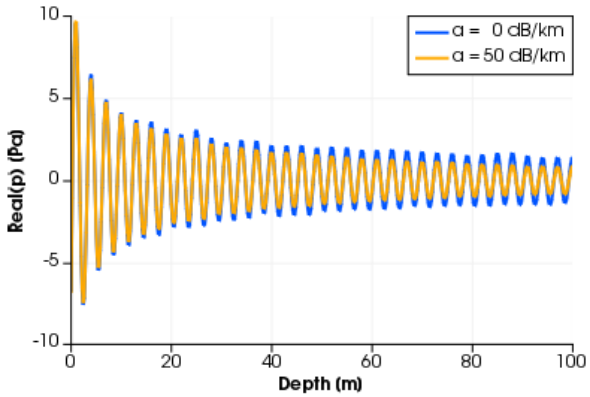

(c)

Figure 4.4: Detail of the real part of the pressure at the central region of the domain ($x \in [-125, +125]$) in Example 1: (a) case without absorption; and (b) case with absorption. (c) Real part of the pressure field along the y axis for both absorption values.

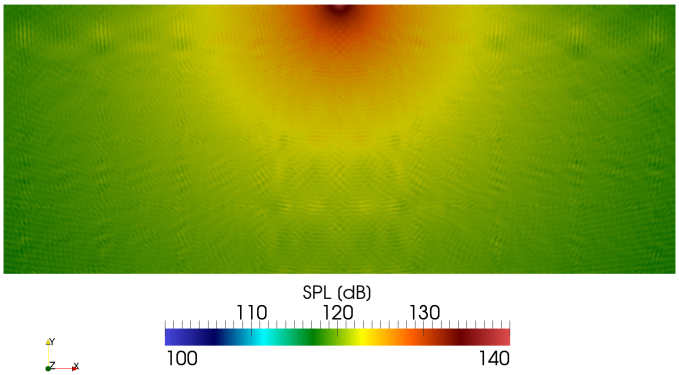

(a)

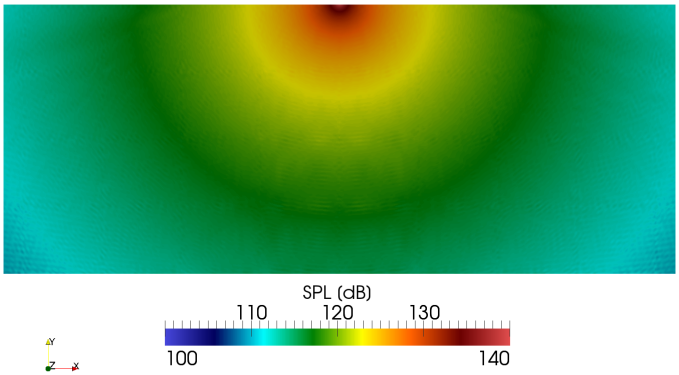

(b)

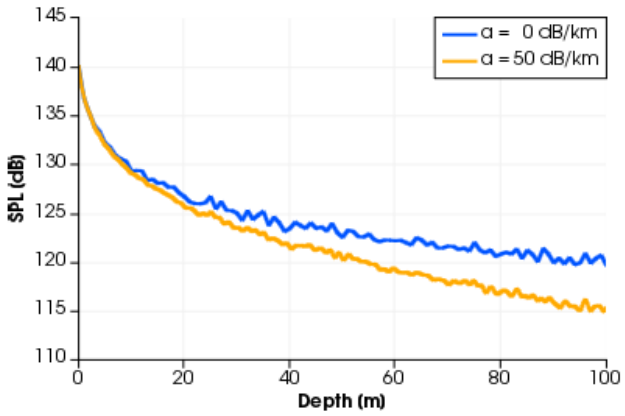

(c)

Figure 4.5: Detail of the SPL (dB) at the central region of the domain ($x \in [-125, +125]$) in Example 1: (a) case without absorption; and (b) case with absorption. (c) SPL distribution along the y-axis for both absorption values.

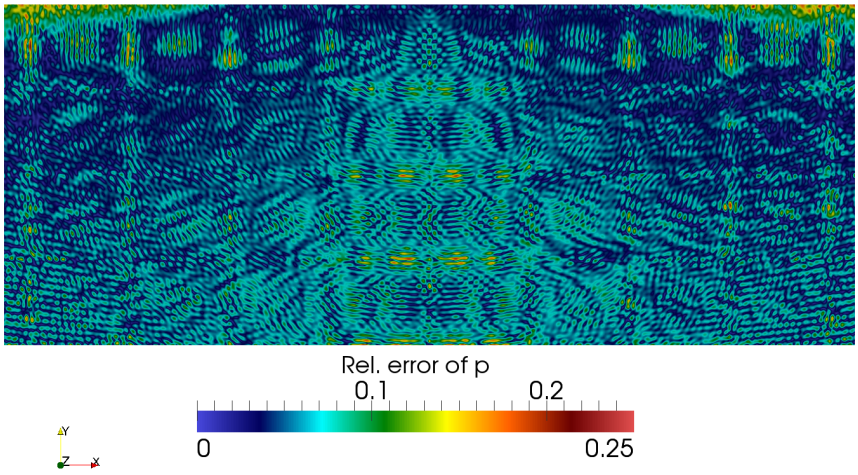

(a)

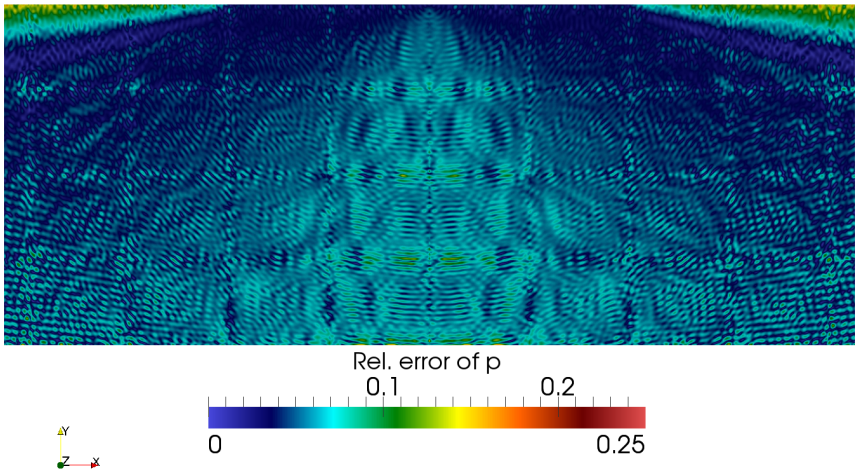

(b)

Figure 4.6: Detail of the point-wise relative error in the pressure at the central region of the domain ($x \in [-125, +125]$) in Example 1: (a) case without absorption; and (b) case with absorption.

of the Robin equation along the boundary edges of few elements around the noise source, see Section 4.2.4. On the other hand, large errors are also located along the edges of the quadrilateral elements.

Second, we also measure the accuracy of the PUM solution by computing the

relative error in L^2 norm as

$$\varepsilon_{L^2} = \frac{\|p_{h,q}(\mathbf{x}) - p_a(\mathbf{x})\|_{L^2}}{\|p_a(\mathbf{x})\|_{L^2}}, \tag{4.22}$$

where

$$\|\cdot\|_{L^2} = \sqrt{\int_\Omega |\cdot|^2 \, \mathrm{d}\Omega},$$

being $|\cdot|$ the complex modulus.

We obtain $\varepsilon_{L^2} = 0.1120$ and $\varepsilon_{L^2} = 0.0541$, for the lossless and lossy cases, respectively. In order to assess the relevance of these error values and if they are acceptable for engineering applications, it is important relating them to the standard relative errors of a quantity in environmental underwater acoustics such as the SPL. To this end, let E_{SPL} be the absolute error in the SPL generated by an absolute error, E_p, in the pressure field. Thus, from Equation (2.1) and according to the Taylor expansion, we have

$$\mathrm{SPL} + E_{\mathrm{SPL}} = 20 \, \log_{10}\left(\frac{p + E_p}{p_0}\right) = 20 \, \log_{10}\left(\frac{p}{p_0}\right) + \frac{1}{\ln(10)} \, \frac{E_p}{p} + \mathcal{O}(E_p^2).$$

Thus, the same expression for the relative errors reads

$$\varepsilon_{\mathrm{SPL}} \, \mathrm{SPL}_{\mathrm{ref}} \approx \frac{1}{\ln(10)} \, \varepsilon_p,$$

where $\varepsilon_{\mathrm{SPL}} = E_{\mathrm{SPL}}/\mathrm{SPL}_{\mathrm{ref}}$ being $\mathrm{SPL}_{\mathrm{ref}}$ a reference SPL value, and $\varepsilon_p = E_p/p$. The SPL in standard audiograms of marine mammals and other fish species ranges from 30 dB to 150 dB, see Thomsen et al. (2006), and is usually given with two significant digits i.e. $\varepsilon_{\mathrm{SPL}} \leq \frac{1}{2}10^{-2}$. Therefore, the worst case scenario corresponds to $\mathrm{SPL}_{\mathrm{ref}} = 30$ dB leading to

$$\varepsilon_p = \ln(10) \, \mathrm{SPL}_{\mathrm{ref}} \, \varepsilon_{\mathrm{SPL}} = 0.34.$$

Therefore, the obtained values for point-wise relative error (4.21), and for the global relative error (4.22) remain inside typical engineering acceptable limits.

4.4.2 Sea bottom with different transmission coefficients

This example includes a bottom composed of two different sloped segments. The left-hand side (LHS) segment has a slope of +0.04 and a transmission coefficient $\tau = 0.9i$

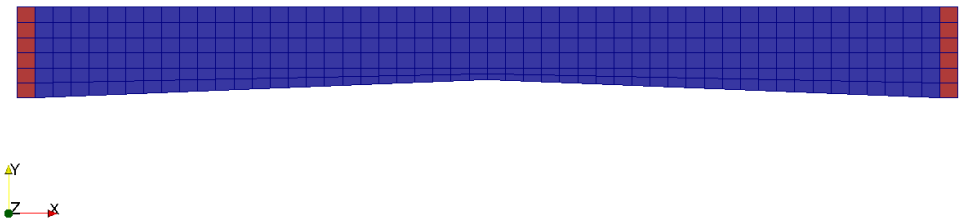

Figure 4.7: 2D mesh used in Example 2, including non-PML elements (in blue) and PML elements (in red).

('soft' material, low impedance mismatch), while the right-hand side (RHS) segment has a slope of -0.04 and a transmission coefficient of $\tau = 0.1i$ ('hard' material, high impedance mismatch). The domain depth varies between 100 m at both lateral ends ($x^- =$ -500 m and $x^+ = 500$ m), and 80 m at the center of the domain, under the noise source. We consider the propagation of the sound generated by a single point source located at the center of the sea surface, $\mathbf{x} = (0, 0)$, with a frequency of $f = 750$ Hz.

A layer of PML elements is placed around the lateral artificial boundaries, see Figure 4.7. The domain is discretized using a structured quadrilateral mesh with 10 wavelengths per element, with element size $(\Delta x, \Delta y) = (20, 16.7)$. The number of approximation functions after the low-rank reduction is 159, giving 56,763 DOFs.

Figures 4.8 and 4.9 show the different noise patterns produced by an absorbing and a reflecting sea bottom. In the LHS domain region, most part of the acoustic energy penetrates the bottom and the fields are similar to the ones of the free propagation case. In the RHS region, most energy reflects and the pattern becomes more complex, as a result of the interaction of the incident and reflected wave fronts (the acoustic energy is partially trapped between the surface and the bottom).

4.4.3 Two sources over a non-horizontal sea bottom with non-uniform sound speed

In this example we consider non-horizontal sea bottom and a non-uniform vertical profile for the sound speed. We set a uniform slope of 0.04, with a depth varying between 100 m at $x^- =$ -500 m, and 60 m at $x^+ = 500$ m. Two identical sources

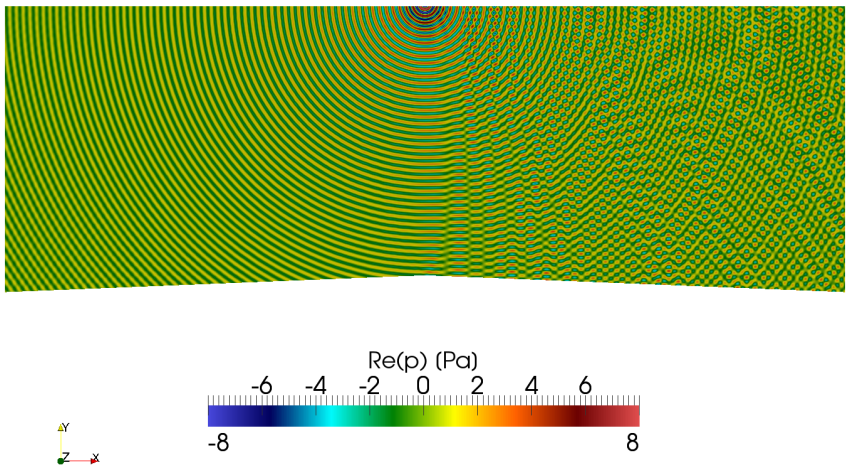

Figure 4.8: Detail of the real part of the pressure (Pa) at the central region of the domain ($x \in [-125, +125]$) in Example 2.

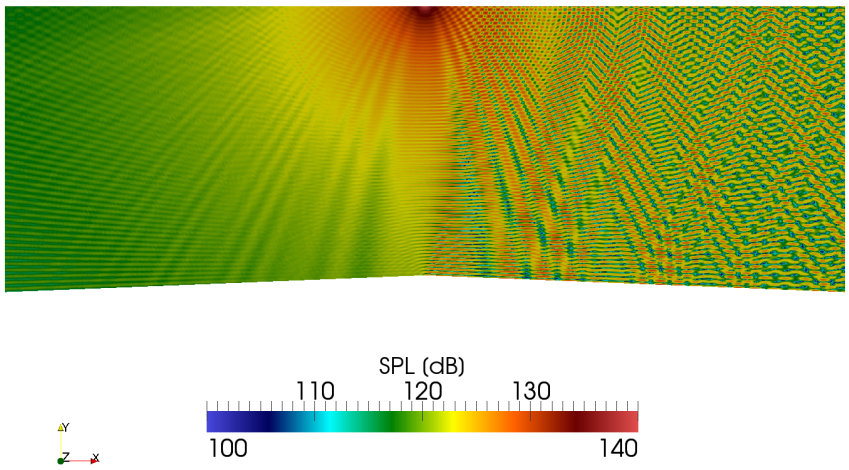

Figure 4.9: Detail of the SPL (dB) at the central region of the domain ($x \in [-125, +125]$) in Example 2.

are placed on the surface at locations (-80,0) and (+80,0). The frequency is $f = 750$ Hz and the transmission coefficient at the bottom is $\tau = 0.9i$. The vertical profile of the sound speed is non-uniform: the speed takes a value of 1,500 m/s at the surface and decreases linearly with depth, at a rate of -0.5 (m/s)/m (1450 m/s at the sea bottom).

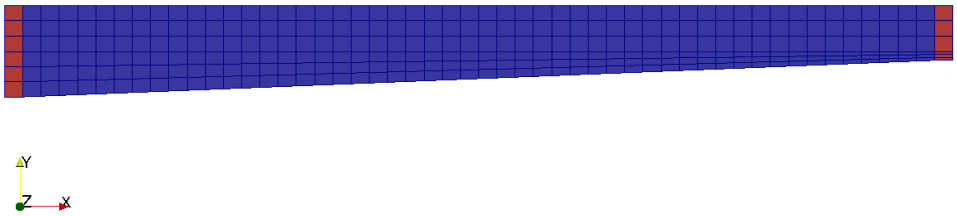

Figure 4.10: 2D mesh used in Example 3, including non-PML elements (in blue) and PML elements (in red).

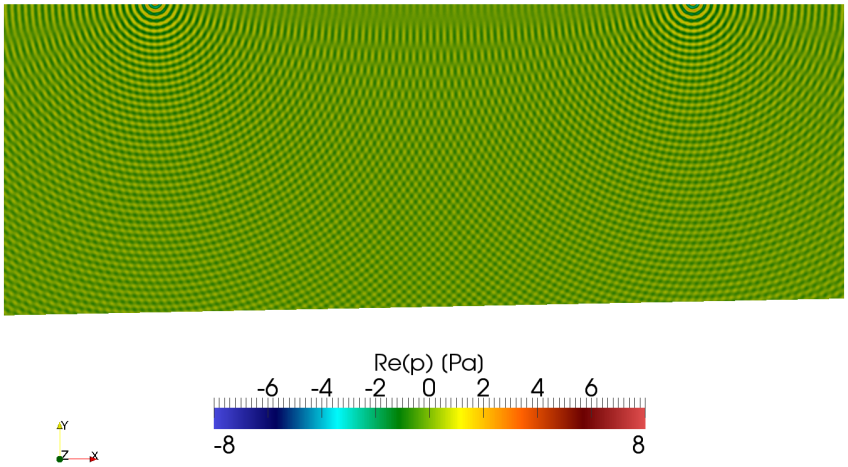

Figure 4.11: Detail of the real part of the pressure (Pa) at the central region of the domain ($x \in (-125, +125)$) in Example 3.

The domain is laterally truncated by PMLs, and it is discretized using a structured quadrilateral mesh that includes 10 wavelengths per element, see Figure 4.10, with an element size of $(\Delta x, \Delta y) = (20, 16.7)$. The number of approximation functions per node after the basis reduction is $\tilde{q} = 159$, giving 56,763 DOFs.

Figure 4.11 shows the constructive and destructive interactions between the two pressure fields, while Figure 4.12 depicts the resulting sound pressure level map.

4.4.4 Sensitivity analysis of the SVD

This example analyzes the influence of the low-rank approximation of the local enrichment basis on the behavior of the method, paying special attention on the memory

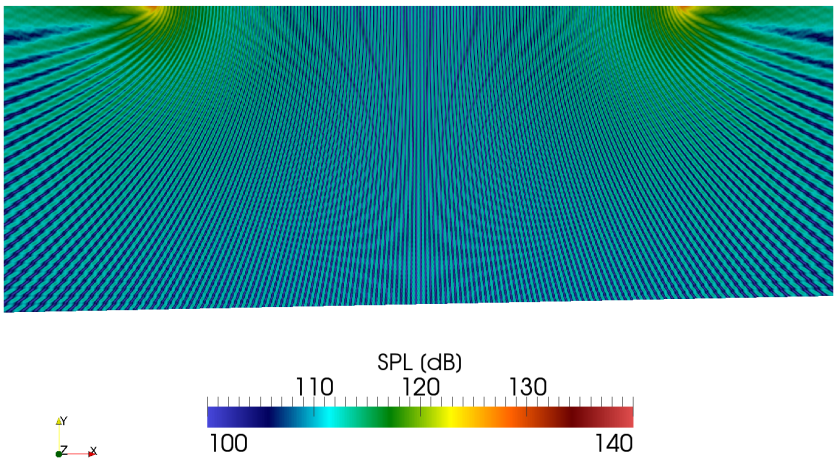

Figure 4.12: Detail of the SPL (dB) at the central region of the domain ($x \in (-125, +125)$) in Example 3.

footprint, CPU time and accuracy of the proposed method. The key parameter is the tolerance applied to the singular values of the patch matrix, see Equation (4.20), and the resulting number of local approximation functions per node, $\tilde{q}$.

We consider the free propagation field generated by a single point source through a half-plane. The domain is truncated creating a rectangular geometrical domain $\Omega = [-500, +500] \times [-100, 0]$. The source is located at center of the sea surface, $\mathbf{x} = (0, 0)$, and generates a noise with a frequency of $f = 250$ Hz.

The example is solved using 2 meshes with different resolutions. First, we use a mesh with 5 wavelengths per element, giving an element size of $(\Delta x, \Delta y) = (29.4, 25)$. Second, we set 10 wavelengths per element, producing an element size of $(\Delta x, \Delta y) = (55.56, 50)$. A layer of PML elements is added around the lateral artificial boundaries and below the sea bottom boundary in both cases.

The initial solution space is determined by $q = 200$ plane waves per node and, after integrating the standard patch matrix, a SVD is computed, see Section 4.3.4. Then, we select the number of singular values that verify Equation (4.20) for $\varepsilon = 10^{-16}, 10^{-14}, \ldots, 10^{-2}$. For each tolerance value, we obtain a reduced approximation space with the corresponding number of approximation functions per node, $\tilde{q}$. Since the analytical solution of this problem is provided by Equation (4.8), we will assess the accuracy of the solution by computing the relative error in L^2 norm given by Equation (4.22).

(a)

Tol	$\tilde{q}$	DOF	K storage (MB)	t solving (s)	E	$\kappa(K\text{patch})$	$\kappa(K\text{red})/\kappa(K)$
0	200	25,000	1597.0	2342.85	13.8834	1.07E+16	1.00E+00
1E-16	200	25,000	1597.0	2347.51	13.8834	1.07E+16	1.00E+00
1E-14	128	16,000	654.2	386.21	0.1018	9.99E+13	9.62E-01
1E-12	99	12,375	391.4	172.23	0.1028	2.43E+11	3.58E-02
1E-10	95	11,875	360.4	163.98	0.1029	5.72E+09	2.59E-02
1E-08	89	11,125	316.3	130.77	0.1018	3.22E+07	1.38E-02
1E-06	83	10,375	275.1	105.61	0.1017	3.39E+05	7.34E-03
1E-04	77	9,625	236.8	80.55	0.1067	7.37E+03	3.52E-03
1E-02	67	8,375	179.3	9.09	0.1027	9.85E+01	1.37E-04

(b)

Tol	$\tilde{q}$	DOF	K storage (MB)	t solving (s)	E	$\kappa(K\text{patch})$	$\kappa(K\text{red})/\kappa(K)$
0	200	11,400	558.6	183.95	0.0759	7.78E+14	1.00E+00
1E-16	200	11,400	558.6	183.33	0.0759	7.78E+14	1.00E+00
1E-14	193	11,001	520.2	165.17	0.0831	9.42E+13	1.11E-03
1E-12	171	9,747	408.4	120.68	0.0716	2.82E+11	9.78E-05
1E-10	165	9,405	380.2	108.47	0.0754	2.91E+09	7.62E-05
1E-08	159	9,063	353.1	97.66	0.0698	4.31E+07	1.65E-04
1E-06	152	8,664	322.7	87.06	0.0768	9.75E+05	1.29E-04
1E-04	143	8,151	285.6	70.67	0.0794	6.43E+03	4.34E-04
1E-02	127	7,239	225.3	50.99	0.1075	8.44E+01	3.13E-04

Table 4.1: Required computational resources and achieved accuracy in Example 4, when (a) 5 or (b) 10 wavelengths per element are considered. For each tolerance value we detail: the reduced number of shape functions $\tilde{q}$ (the initial number is $q = 200$), the global number of degrees of freedom, the memory space for the global system matrix, the CPU time for the solving step, the relative L^2-norm error, the condition number of the patch matrix, and the ratio between the condition numbers of the reduced and original system matrices.

Table 4.1 summarizes, for each tolerance value ε, the most relevant computational parameters and the obtained accuracy, when 5 and 10 wavelengths per element are considered. We highlight that for both meshes, increasing the tolerance ε (first column) reduces the number of singular values (second column), that is the number of approximation functions per node, leading to a linear reduction in the number of DOFs (third column). This implies an important decrease in the size of the global system matrix or memory footprint (fourth column) and in the CPU time needed to solve the linear system (fifth column), while the relative L^2-norm error is also reduced

(sixth column). It is important to point out that the CPU time involved in the low-rank approximation calculation step is small (below 4 seconds in all cases), compared to the total time of the simulation. In addition, the CPU time for the integration step is almost constant once the number of wavelengths per element is fixed since, in practice, the original approximation functions are always integrated whatever the tolerance value.

As expected, if the original number of shape functions is considered ($q = 200$), the condition number of the generic patch matrix is extremely large, but it decreases as the number of singular values is reduced (seventh column). Moreover, the latter implies a decreasing in the condition number of the global matrix up to 5 orders of magnitude (eighth column).

One of the drawbacks of using enriched solution spaces is that the number of components of the elemental matrices increases with the square of the number of approximation function per node, q, leading to large element matrices, and reducing the sparsity of the global matrix. For instance, the ratio of the number of non-zero entries over the total number of entries in this example is 3.6% when the mesh contains 5 wavelengths per element, and 8.7% when it contains 10 wavelengths per element. However, in this example we show that a given accuracy can be achieved using a reduced number of combinations of these basis functions. Thus, we can use coarse meshes (large number of wave lengths per element) while keeping the sparsity of the matrix moderate.

Although, for a given accuracy, the use of coarser meshes, with a larger number of wavelengths per elements, requires an increase of the number of enrichment functions per node, numerical experiments show that the increment in the number of approximation functions is compensated by the reduction in the number of mesh nodes, leading to a smaller global number of degrees of freedom, and consequently, to a lower computational cost, see Table 4.1.

4.5 Concluding remarks

In this chapter we have presented a new 2D numerical model to simulate the undersea acoustic propagation generated by multiple non-impulsive (operational) noise sources. The model includes the most relevant physical phenomena such as sea water absorption, via a complex wavenumber, and the reflectance of the sea bottom and

surface. Artificial fully absorbing boundary conditions are also included in the lateral boundaries by means of Perfectly Matched Layers.

We have successfully used the Partition of the Unity Method to solve the corresponding weak form of the Helmholtz equation, since harmonic noise sources are heeded. Specifically, we enrich the solution space by pasting several plane waves with the physical wavenumber at each patch of the discretization. Two basic ingredients are proposed to properly solve the weak form. On the one hand we have implemented a semi-analytical scheme in order to integrate highly oscillatory functions over quadrilateral elements. This allows reducing the computational cost of the integration step while maintaining its accuracy. On the other hand, we have developed a new procedure to reduce the condition number of the elemental and global matrices. It is based on a low-rank approximation of the local enrichment basis associated to the central node of a reference patch. This way, we have reduced the size of the global matrix while preserving the accuracy of the approximation.

We have applied the model to several scenarios including absorbing medium, sea bottom composed of different materials, and non-planar sea bottom. In addition, we have computed the free propagation of the sound generated by a single point source through a lossless and through a lossy media, and compared it with the analytical solution. In both cases we obtained accurate results. Finally, we have analyzed the influence of the low-rank approximation on the behavior of the proposed method. Numerical experiments show that by reducing the number of local approximation functions, we can also reduce the required computational resources and the accuracy of the results.

Chapter 5

A semi-analytical scheme for highly oscillatory integrals over tetrahedra

This chapter details a semi-analytical procedure to efficiently integrate the product of a smooth function and a complex exponential over tetrahedral elements Hospital-Bravo et al. (2017). These highly oscillatory integrals appear at the core of different numerical techniques. Here, the partition of unity method enriched with plane waves is used as motivation. The high computational cost or the lack of accuracy in computing these integrals is a bottleneck for their application to engineering problems of industrial interest. In this integration rule, the non-oscillatory function is expanded into a set of Lagrange polynomials. In addition, Lagrange polynomials are expressed as a linear combination of the appropriate set of monomials, whose product with the complex exponentials is analytically integrated, leading to 16 specific cases that are developed in detail. Finally, we present several numerical examples to assess the accuracy and the computational efficiency of the proposed method, compared with standard Gauss-Legendre quadratures.

5.1 Introduction

During the last two decades, special attention has been focused on the computation of highly oscillatory integrals in applied sciences and engineering. The problem arises in several fields such as quantum mechanics, image analysis, electrodynamics, and wave propagation problems. This type of integrals cannot be efficiently computed with standard quadratures (such as the Gauss-Legendre quadrature) because the highly oscillatory integrand is not properly represented by polynomial interpolation. Thus, a very large number of integration points is needed and the computational cost becomes prohibitive, particularly in the case of medium or high frequencies, three-dimensional (3D) problems or large domains.

Wave problems lead to oscillatory solutions, which are poorly captured by the classical polynomial shape functions, associated with the standard finite element method. Moreover, for high wavenumber applications, the numerical dispersion makes the discrete wavenumber differ drastically from the exact solution. This is called the pollution effect, and it separates the solution of the standard finite element method from the best approximation Babuška and Sauter (1997) (Ihlenburg, 1998, Section 4.6) Deraemaeker et al. (1999).

Although high-order methods and discontinuous formulations provide lower dissipation and dispersion, alternative finite element formulations have been developed to overcome this limitation by including special shape functions into the approximation space, see Melenk (1995); Melenk and Babuška (1996) for continuous formulations or Farhat et al. (2001, 2003, 2004); Hiptmair et al. (2011) for discontinuous formulations. These *enriching* functions include a priori knowledge of the solution and improve the quality of the local and global approximation properties. In the case of the Helmholtz equation, it is advantageous to include sets of plane waves propagating in different directions, because they are free-space natural solutions when a uniform wavenumber is considered and they form a so-called *c-complete* set of functions that allows spanning the whole space of solutions, see Herrera and Sabina (1978); Laghrouche and Bettess (2000) for details. Thus, the enriched approximation space allows a drastic reduction of the pollution error, see Babuška and Sauter (1997) and (Ihlenburg, 1998, Section 4.8) for a detailed analysis. This alleviates the constraint of having a minimum number of elements per wavelength (typically 10 or 12 as a rule of thumb), allowing the use of coarser meshes with several wavelengths per element. These meshes provide a considerable reduction in the total number of unknowns (more than 90% in some

cases).

However, the enriching functions and their derivatives have to be integrated over each element. In some of these plane-waves based methods the integrals are easier to compute, such as the Ultra Weak Variational Formulation Cessenat and Després (1998) or the Discontinuous Enrichment Method Farhat et al. (2001, 2003, 2004). In the case of the Partition of the Unity Method (PUM), the selection of standard Gauss-Legendre quadratures becomes inadequate due to the highly oscillatory behavior of the resulting integrands, and alternative efficient integration techniques are needed. Many classical and modern methods for solving one-dimensional (1D) finite regular Fourier integrals can be found in Evans and Webster (1999) and in Iserles and Nørsett (2005); Huybrechs and Vandewalle (2006). In the context of the Partition of the Unity Method (PUM), Ortiz and Sanchez (2001) introduced a local coordinate rotation over triangular elements to obtain 1D oscillatory integrands and compute these integrals semi-analytically. A semi-analytical rules for two-dimensional (2D) problems that consider the special nature of the integrand and profit from it to perform the integration were presented in Bettess et al. (2003); Sugimoto et al. (2003) developed . In these rules, the non-oscillatory part of the integrands is approximated by a set of interpolating Lagrange polynomials. Then, the products of these polynomials and the complex exponentials are integrated analytically. The result is a set of integration weights, which are specific for each combination of element geometry and parameter of the complex exponential. The key point of these rules is that the distribution of the integration points captures the behavior of the smooth part of the integrand, rather than the whole oscillatory behavior, which is analytically captured by the integration weights. Therefore, the spacing of the integration points is larger, dramatically reducing their number and, hence, the number of function evaluations, compared with the Gauss-Legendre quadrature. This approach has been recently applied in the context of underwater acoustics in Hospital-Bravo et al. (2016). An alternative approach to compute the integral of the product of a polynomial and a complex exponential over arbitrary polygons is presented in Gabard (2009), polyhedral volumes and 3D surfaces, by rewriting volume integrals in terms of 1D integrals along the element edges thanks to the Gauss and the Stokes theorems.

The novelty of our contribution is a fast and robust semi-analytical rule to compute the volumetric integrals of highly oscillatory functions (expressed as the product of a smooth function and a complex exponential) on tetrahedral elements. In this sense,

it is a generalization to a 3D setting of the integration rule developed by Bettess et al. (2003); Sugimoto et al. (2003). The method proposed here follows the usual practice of standard quadratures and considers the evaluation of the non-oscillatory function at the integration points. This is in contrast to Gabard (2009) that considers as input data the coefficients of the polynomial (non-oscillatory part of the integrand), and after applying the Gauss and the Stokes theorems, performs 1D integrals along the element edges. The proposed quadrature is better fitted to be implemented in a Finite Element like methodology. This is because the information describing the (non-oscillatory part of the) function to be integrated is required as values at a set of integration points, which is the standard practice in Finite Elements. On the contrary, the quadrature introduced in Gabard (2009) requires as input data the coefficients of the polynomial in some basis. Thus, for the specific application in a Finite Element framework, using Gabard (2009) requires an additional step that consists in finding the analytical expression of the polynomial from point values with some interpolation technique. Note that this new operation introduces an additional interpolation error.

The rest of this chapter is organized as follows: Section 5.2 describes the semi-analytical scheme, detailing the Lagrange expansion in terms of a linear combination of a basis of monomials, and the expression of the integration weights of the semi-analytical rule. Section 5.3 provides several preliminary results required to develop Section 5.4, which presents the new scheme to compute the target integral. Specifically, we detail how this scheme leads to 16 different cases. Section 5.5 summarizes how the PUM enriched with plane waves benefits from this semi-analytical scheme. Section 5.6 presents several numerical examples to underline the main properties of the proposed rule. Finally, the conclusions extracted from this work are collected in Section 5.7.

5.2 Highly oscillatory integral over a tetrahedron

The objective of this work is obtaining an efficient semi-analytical integration rule to compute the following family of highly oscillatory integrals over a tetrahedron Ω^{TET}:

$$K = \int_{\Omega^{\mathrm{TET}}} f(\mathbf{x}) \exp\left(i\mathbf{v}\cdot\mathbf{x}\right) \mathrm{d}\mathbf{x}, \tag{5.1}$$

where $\mathbf{x}$ is the vector of coordinates, f is a smooth (non-oscillatory) function, $i = \sqrt{-1}$ is the imaginary unit, and $\mathbf{v}$ is an arbitrary and complex vector. The complex

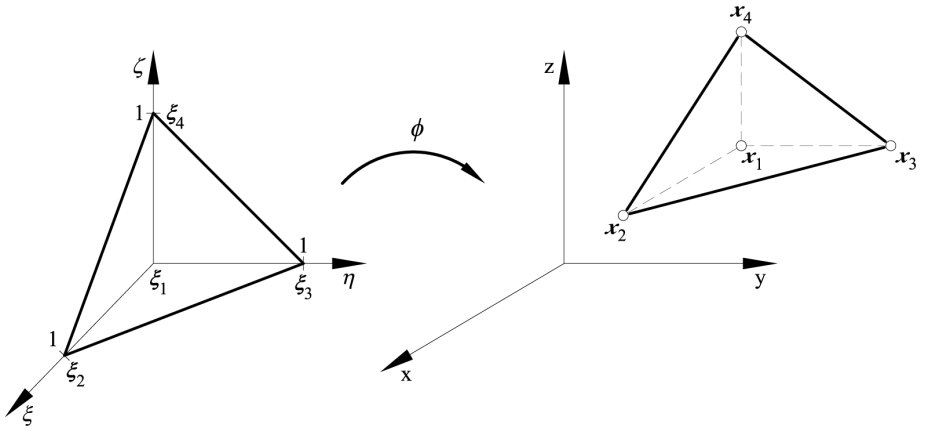

Figure 5.1: Geometrical mapping between the reference and physical tetrahedral element.

exponential is considered as highly oscillatory if it oscillates several times inside the element, that is, if

$$\frac{\|\mathbf{v}\|h}{2\pi} \gg 1,$$

where h is a characteristic length. Because the methodology is conceived for an application in the context of generalized finite elements, in the following h denotes the element size. This kind of integral is also known as regular finite Fourier integral.

5.2.1 Lagrange polynomials expansion and semi-analytical scheme

We rewrite the integral in Equation (5.1) at the reference tetrahedron Ω^{ref} (Figure 5.1) as

$$K = \int_{\Omega^{\text{ref}}} f(\mathbf{x}(\xi)) \exp\left(i\mathbf{v}\cdot\mathbf{x}(\xi)\right) |\mathbf{J}(\xi)| \, \mathrm{d}\xi = \int_{\Omega^{\text{ref}}} F(\xi) \exp\left(i\mathbf{v}\cdot\mathbf{x}(\xi)\right) \, \mathrm{d}\xi, \qquad (5.2)$$

where $\xi = (\xi, \eta, \zeta)$ is the vector of reference coordinates and $F(\xi) = f(\mathbf{x}(\xi))|\mathbf{J}(\xi)|$, and $|\mathbf{J}(\xi)|$ stands for the Jacobian of mapping ϕ between the reference and the physical tetrahedron. Although the Jacobian $|\mathbf{J}(\xi)|$ is constant (independent of ξ) for linear tetrahedral elements, the dependence on ξ is however kept inside $\mathbf{J}$ to highlight that this framework is also valid for mappings with a nonuniform Jacobian.

The non-oscillatory function $F(\xi)$ is now approximated by means of a set of Lagrange interpolating polynomials:

$$F(\xi) \approx \sum_{d=1}^{n_p} F(\xi_d) L_d(\xi), \tag{5.3}$$

where L_d is the Lagrange polynomial of degree p associated with the d-th integration point ξ_d, $d = 1, \ldots, n_p$, and n_p is the number of integration points. Therefore, the integral in Equation (5.1) is computed using the following integration rule:

$$K \approx \int_{\Omega^{\text{ref}}} \left(\sum_{d=1}^{n_p} F(\xi_d) L_d(\xi) \right) \exp\left(i\mathbf{v} \cdot \mathbf{x}(\xi)\right) \, \mathrm{d}\xi = \sum_{d=1}^{n_p} F(\xi_d) w_d,$$

where

$$w_d = \int_{\Omega^{\text{ref}}} L_d(\xi) \exp\left(i\mathbf{v} \cdot \mathbf{x}(\xi)\right) \, \mathrm{d}\xi \qquad \text{for } d = 1, \ldots, n_p, \tag{5.4}$$

is the complex integration weight corresponding to the d-th integration point. Note that the accuracy of integral (5.1) strongly depends on the quality of the approximation in Equation (5.3).

The difficulty lies now in the evaluation of the integration weights w_d, for $d = 1, \ldots, n_p$. Their values depend on vector $\mathbf{v}$ and the element geometry. Therefore, it is not possible to *a priori* compute a set of weights for a given set of integration points that are valid for any element geometry. To develop an efficient procedure, it is convenient to decompose the Lagrange polynomials into the appropriate set of 3D monomials:

$$L_d(\xi) = \sum_{|\mathbf{a}| \leq p} \lambda_{d,\mathbf{a}} M_{\mathbf{a}}(\xi), \tag{5.5}$$

where

$$M_{\mathbf{a}}(\xi) = \xi^a \eta^b \zeta^c, \tag{5.6}$$

and $\lambda_{d,\mathbf{a}}$ is the coefficient associated with the d-th polynomial and the $\mathbf{a}$-th monomial. The multi-index notation considers $\mathbf{a} = (a, b, c)$, where a, b, c are non-negative integers and $|\mathbf{a}| := a + b + c \leq p$. Appendix C details a procedure to compute the coefficients $\lambda_{d,\mathbf{a}}$ of the monomial decomposition in a straightforward manner.

Substituting Equation (5.5) into Equation (5.4), we obtain a new expression for the integration weights:

$$w_d = \sum_{|\mathbf{a}| \leq p} \lambda_{d,\mathbf{a}} \int_{\Omega^{\text{ref}}} M_{\mathbf{a}}(\xi) \exp\left(i\mathbf{v} \cdot \mathbf{x}(\xi)\right) \, \mathrm{d}\xi. \tag{5.7}$$

Remark 5.1. *Other interpolation functions could be used to approximate $F(\xi)$ in Equation* (5.3)*. Nevertheless, Lagrange polynomials are easily decomposed into a set of monomials (Appendix C) leading to the integration of products of monomials and complex exponential that can be performed semi-analytically. The examples presented in Section 5.6 show that this procedure is also advantageous from the computational point of view.*

Remark 5.2. *The number of integration points, n_p, can be determined by imposing that the quadrature integrates Equation* (5.2) *exactly (up to round-off errors) when $F(\xi)$ is a polynomial of degree $\leq p$. This number must coincide with the dimension of the polynomial space, which can be obtained from the Pascal's pyramid as*

$$n_p = \frac{1}{2}\left(\frac{(p+1)^3}{3} + (p+1)^2 + \frac{4(p+1)}{6}\right).$$

If $F(\xi)$ is not a polynomial function, an appropriate value for p fitting the behavior of the function has to be selected.

Remark 5.3. *Following the work proposed in Bettess et al. (2003); Sugimoto et al. (2003), we consider an equidistributed set of integration points. Selecting optimal locations for the integration points as in the case of the Gauss-Legendre quadratures is not possible in this context. This is because the oscillating term, $\exp(i\mathbf{v}\cdot\mathbf{x}(\xi))$, acting as kernel of a bilinear form that should be a scalar product, is a complex function. Consequently, it cannot be used to define a scalar product (a complex kernel function is associated with non-positive definite bilinear form). Even if the kernel was real valued, it would be dependent on the geometry of the element and on the argument of the complex exponential, vector $\mathbf{v}$.*

5.2.2 Tetrahedral finite elements

We consider the 3D linear mapping ϕ from the reference coordinates ξ to the global coordinates $\mathbf{x}$:

$$\mathbf{x} = \phi(\xi) = \alpha\xi + \beta\eta + \gamma\zeta + \delta, \tag{5.8}$$

where

$$\alpha = \mathbf{x}_2 - \mathbf{x}_1, \qquad \beta = \mathbf{x}_3 - \mathbf{x}_1, \qquad \gamma = \mathbf{x}_4 - \mathbf{x}_1, \qquad \delta = \mathbf{x}_1,$$

defined on the reference domain $0 \leq \xi \leq 1-\zeta-\eta$, $0 \leq \eta \leq 1-\zeta$, and $0 \leq \zeta \leq 1$ (Figure 5.1). Introducing equations (5.6) and (5.8) into the expression for the integration

weights, Equation (5.7), we obtain

$$w_d = \exp(iD) \sum_{|\mathbf{a}| \leq p} \lambda_{d,\mathbf{a}} I_{\mathbf{a}}, \tag{5.9}$$

where

$$I_{\mathbf{a}} = \int_0^1 \int_0^{1-\zeta} \int_0^{1-\zeta-\eta} \xi^a \eta^b \zeta^c \exp(iA\xi) \exp(iB\eta) \exp(iC\zeta) \, \mathrm{d}\xi \, \mathrm{d}\eta \, \mathrm{d}\zeta, \tag{5.10}$$

$$A = \mathbf{v} \cdot \alpha, \qquad B = \mathbf{v} \cdot \beta, \qquad C = \mathbf{v} \cdot \gamma, \qquad D = \mathbf{v} \cdot \delta,$$

and a, b, c being non-negative integers. Note that the weights depend on vector $\mathbf{v}$ and the element geometry through the complex parameters A, B, C, and D.

The rest of the paper focuses on the analytical solution of the integral in Equation (5.10).

5.3 Preliminary results: integrating 1D products of a monomials and a complex exponential function

This section provides two basic results that will be used in Section 5.4 to obtain the analytical solution of integral (5.10). Our semi-analytical procedure seeks successive 1D term collections that head toward the analytical integration of the following 1D product of a monomial and a highly oscillatory term:

$$I_{1\mathrm{D}} = \int s^\nu \exp(i\mu s) \, \mathrm{d}s, \tag{5.11}$$

where ν is a non-negative integer, and the value of the complex coefficient μ depends on the values of coefficients A, B and C.

We consider this type of 1D integral at two stages of the development of our numerical procedure. On the one hand, the analytical manipulation of Equation (5.10) leads to 1D highly oscillatory integrals such that the upper limit of the integral depends on the reference spatial coordinates, see details in Section 5.4. On the other hand, these intermediate integrals are further developed leading to 1D highly oscillatory integrals with fixed integration limits (between 0 and 1). This section focuses on the first situation while Appendix D deals with the second one.

We consider two cases in the first situation, depending on the value of parameter μ, as suggested in Sugimoto et al. (2003). First, if the modulus of μ is not small, $\mu \nrightarrow 0$, and given that exponent ν is a non-negative integer, after recursively applying the integration by parts theorem we have

$$\int s^{\nu} \exp(i\mu s)\, \mathrm{d}s = \nu! \sum_{r=0}^{\nu} \frac{i^{r-1} s^{\nu-r} \exp(i\mu s)}{(\nu - r)! \mu^{r+1}}. \tag{5.12}$$

Second, for certain combinations of the values of coefficients A, B and C in Equation (5.10), the analytical manipulations involve integrals of type (5.11) with a very small values of coefficient μ, $\mu \to 0$, and Equation (5.12) provides inaccurate results. Thus, it is preferable to apply a truncated Taylor's expansion to the exponential function before proceeding with the analytical integration. Specifically, we set

$$\exp(i\mu s) \approx \sum_{r=0}^{r_{\max}} \frac{(i\mu s)^r}{r!}$$

where $r_{\max}$ is the number of terms retained in the approximation. This number is adjusted so that the truncation error in the series is of the order of the machine accuracy ϵ. Because in this paper both ν and r are non-negative integer parameters, we have

$$\int s^{\nu} \exp(i\mu s)\, \mathrm{d}s \approx \sum_{r=0}^{r_{\max}} \frac{(i\mu)^r}{r!} \int s^{\nu+r}\, \mathrm{d}s = \sum_{r=0}^{r_{\max}} \frac{(i\mu)^r}{r!} \frac{s^{\nu+r+1}}{\nu + r + 1}. \tag{5.13}$$

It remains to determine the threshold value, μ_{th}, to switch between equations (5.12) and (5.13). In our implementation we consider that μ is small enough if $|\mu|^{\nu+1} < \mathrm{tol}$. Thus, the threshold value for μ is

$$\mu_{\mathrm{th}} = \mathrm{tol}^{\frac{1}{\nu+1}}.$$

We set $\mathrm{tol} = 10^{-4}$, based on our experience.

Finally, the following type of integral also appears in Section 5.4:

$$\int s^{\nu} (t - s)^{\kappa} \exp(i\mu s)\, \mathrm{d}s.$$

This integral can be expressed as a sum of integrals from Equation (5.11) thanks to the binomial theorem,

$$(t - s)^{\kappa} = \kappa! \sum_{r=0}^{\kappa} \frac{(-1)^r}{(\kappa - r)! r!} t^{(\kappa - r)} s^r,$$

Table 5.1: Possible combinations of the values of coefficients A, B, and C to obtain the integral $I_{\mathbf{a}}$ from Equation (5.10), leading to 16 cases of analytical expressions.

Case	A	B	C	$C-B$	$C-A$	$B-A$
1	$\nrightarrow 0$	$\nrightarrow 0$	$\nrightarrow 0$	$\nrightarrow 0$	$\nrightarrow 0$	$\nrightarrow 0$
2	$\nrightarrow 0$	$\nrightarrow 0$	$\rightarrow 0$	—	—	$\nrightarrow 0$
3	$\nrightarrow 0$	$\nrightarrow 0$	$\nrightarrow 0$	$\nrightarrow 0$	$\rightarrow 0$	$\nrightarrow 0$
4	$\nrightarrow 0$	$\nrightarrow 0$	$\nrightarrow 0$	$\rightarrow 0$	$\nrightarrow 0$	$\nrightarrow 0$
5	$\nrightarrow 0$	$\nrightarrow 0$	$\nrightarrow 0$	$\rightarrow 0$	$\rightarrow 0$	$\nrightarrow 0$
6	$\nrightarrow 0$	$\rightarrow 0$	$\nrightarrow 0$	—	$\nrightarrow 0$	—
7	$\nrightarrow 0$	$\rightarrow 0$	$\nrightarrow 0$	—	$\rightarrow 0$	—
8	$\nrightarrow 0$	$\rightarrow 0$	$\rightarrow 0$	—	—	—
9	$\nrightarrow 0$	$\nrightarrow 0$	$\nrightarrow 0$	—	$\nrightarrow 0$	$\rightarrow 0$
10	$\nrightarrow 0$	$\nrightarrow 0$	$\nrightarrow 0$	—	$\rightarrow 0$	$\rightarrow 0$
11	$\nrightarrow 0$	$\nrightarrow 0$	$\rightarrow 0$	—	—	$\rightarrow 0$
12	$\rightarrow 0$	$\nrightarrow 0$	$\nrightarrow 0$	$\nrightarrow 0$	—	—
13	$\rightarrow 0$	$\nrightarrow 0$	$\nrightarrow 0$	$\rightarrow 0$	—	—
14	$\rightarrow 0$	$\nrightarrow 0$	$\rightarrow 0$	—	—	—
15	$\rightarrow 0$	$\rightarrow 0$	$\nrightarrow 0$	—	—	—
16	$\rightarrow 0$	$\rightarrow 0$	$\rightarrow 0$	—	—	—

leading to

$$\int s^{\nu}(t-s)^{\kappa}\exp\left(i\mu s\right)\,\mathrm{d}s = \kappa!\sum_{r=0}^{\kappa}\frac{(-1)^r t^{\kappa-r}}{(\kappa-r)!r!}\int s^{\nu+r}\exp\left(i\mu s\right)\,\mathrm{d}s, \tag{5.14}$$

that can be solved using equations (5.12) or (5.13), depending on the value of coefficient μ.

5.4 Analytical development to obtain the expressions for the weights

To obtain the integration weights (5.9) of the semi-analytical rule, in this Section we develop a procedure to evaluate the highly oscillatory integral in Equation (5.10). Specifically, we first apply the analytical expressions presented in the previous section, Equations (5.12) and (5.13), to perform the inner integrals involving ξ and η. This procedure leads to 16 cases depending on the values of coefficients A, B and C, and their respective differences (Table 5.1). In all of them, we finally have to compute

a 1D highly oscillatory integral in terms of ζ between 0 and 1. This last integral is performed using the procedure detailed in Appendix D.

From Equation (5.10) we first collect terms depending on ξ:

$$I_{\mathbf{a}} = \int_0^1 \int_0^{1-\zeta} \eta^b \zeta^c \exp(iB\eta) \exp(iC\zeta) \left(\int_0^{1-\zeta-\eta} \xi^a \exp(iA\xi)\, \mathrm{d}\xi \right) \mathrm{d}\eta\, \mathrm{d}\zeta. \quad (5.15)$$

The inner integral in Equation (5.15) corresponds to the type of integrals in Equation (5.11), presented in Section 5.3. Thus, its evaluation depends on the value of A. Cases 1-11 in Table 5.1 consider $A \nrightarrow 0$ while cases 12–16 consider $A \to 0$.

5.4.1 Cases from 1 to 11 ($A \nrightarrow 0$)

If $A \nrightarrow 0$, we perform the 1D integral with respect to ξ by means of Equation (5.12),

$$\begin{aligned}
I_{\mathbf{a}} &= \int_0^1 \int_0^{1-\zeta} \eta^b \zeta^c \exp(iB\eta) \exp(iC\zeta) \left[a! \exp(iA\xi) \sum_{r=0}^{a} \frac{i^{r-1} \xi^{a-r}}{(a-r)! A^{r+1}} \right]_0^{1-\zeta-\eta} \mathrm{d}\eta\, \mathrm{d}\zeta \\
&= a! \int_0^1 \int_0^{1-\zeta} \eta^b \zeta^c \exp(iB\eta) \exp(iC\zeta) \\
&\quad \left(\exp(iA(1-\zeta-\eta)) \sum_{r=0}^{a} \left(\frac{i^{r-1}(1-\zeta-\eta)^{a-r}}{(a-r)! A^{r+1}} \right) \right. \\
&\quad \left. - \lim_{\xi \to 0} \left(\exp(iA\xi) \sum_{r=0}^{a} \frac{i^{r-1} \xi^{a-r}}{(a-r)! A^{r+1}} \right) \right) \mathrm{d}\eta\, \mathrm{d}\zeta \\
&= a! \left(\exp(iA) \sum_{r=0}^{a} \left(\frac{i^{r-1}}{(a-r)! A^{r+1}} I_{1,r} \right) - \frac{i^{a-1}}{A^{a+1}} I_{TRI} \right), \quad (5.16)
\end{aligned}$$

where

$$I_{1,r} = \int_0^1 \int_0^{1-\zeta} \eta^b \zeta^c (1-\zeta-\eta)^{a-r} \exp(i(B-A)\eta) \exp(i(C-A)\zeta)\, \mathrm{d}\eta\, \mathrm{d}\zeta \quad (5.17)$$

and

$$I_{\mathrm{TRI}} = \int_0^1 \int_0^{1-\zeta} \eta^b \zeta^c \exp(iB\eta) \exp(iC\zeta)\, \mathrm{d}\eta\, \mathrm{d}\zeta. \quad (5.18)$$

Equation (5.18) is the 2D version over triangular elements of the integral in Equation (5.10). The semi-analytical rule for this integral was proposed in Bettess et al. (2003), and it is detailed in Appendix E for completeness.

Taking into account Equation (5.14), and collecting the terms of η, Equation (5.17) becomes

$$I_{1,r} = (a-r)!\sum_{s=0}^{a-r}\left(\frac{(-1)^s}{(a-r-s)!s!}\int_0^1 \zeta^c(1-\zeta)^{a-r-s}\exp\left(i(C-A)\zeta\right)\left(\int_0^{1-\zeta}\eta^{b+s}\exp\left(i(B-A)\eta\right)\,\mathrm{d}\eta\right)\,\mathrm{d}\zeta\right). \tag{5.19}$$

At this point, another split in the procedure is produced depending on the value of $B-A$.

5.4.1.1 Cases from 1 to 8 ($A \nrightarrow 0, B-A \nrightarrow 0$).

Because $B-A \nrightarrow 0$ we rewrite the inner integral in Equation (5.19) using Equation (5.12). Thus,

$$I_{1,r} = (a-r)!\sum_{s=0}^{a-r}\left(\frac{1}{(a-r-s)!s!}(b+s)!\left(\exp\left(i(B-A)\right)\sum_{t=0}^{b+s}\left(\frac{i^{2s+t-1}}{(b+s-t)!(B-A)^{t+1}}\int_0^1\zeta^c(1-\zeta)^{a+b-r-t}\exp\left(i(C-B)\zeta\right)\,\mathrm{d}\zeta\right)-\frac{i^{b+s-1}}{(B-A)^{b+s+1}}\int_0^1\zeta^c(1-\zeta)^{a-r-s}\exp\left(i(C-A)\zeta\right)\,\mathrm{d}\zeta\right)\right). \tag{5.20}$$

Eight different cases arise depending on the possible combinations of B, C, $C-A$ and $C-B$. The expressions for these integrals are obtained by developing equations (5.18) and (5.20), using the results presented in Appendixes E and D, respectively.

5.4.1.2 Cases from 9 to 11 ($A \nrightarrow 0, B-A \to 0$) .

Because $B-A \to 0$, we develop the inner integral in Equation (5.19) using Equation (5.13). Thus,

$$I_{1,r} = (a-r)!\sum_{s=0}^{a-r}\left(\frac{1}{(a-r-s)!s!}\sum_{t=0}^{t_{\max}}\left(\frac{i^{2s+t}(B-A)^t}{t!(b+s+t+1)}\int_0^1\zeta^c(1-\zeta)^{a+b-r+t+1}\exp\left(i(C-A)\zeta\right)\,\mathrm{d}\zeta\right)\right). \tag{5.21}$$

Three different cases arise depending on the possible combinations of C and $C-A$. Again, integral (5.18) is computed using the procedure detailed in Appendix E.

The expressions for Equation (5.21) can be obtained by using the binomial theorem, Equation (5.14), and Appendix D.

5.4.2 Cases from 12 to 16 ($A \to 0$)

Starting again from Equation (5.15), and considering that $A \to 0$, we perform the 1D integral with respect to ξ using Equation (5.13). Hence,

$$I_{\mathbf{a}} = \sum_{r=0}^{r_{\max}} \frac{(iA)^r}{r!(a+r+1)} \int_0^1 \int_0^{1-\zeta} \eta^b \zeta^c (1-\zeta-\eta)^{a+r+1} \exp(iB\eta) \exp(iC\zeta)\, \mathrm{d}\eta\, \mathrm{d}\zeta.$$

Applying the binomial theorem, Equation (5.14), and collecting terms depending on η, we obtain

$$I_{\mathbf{a}} = \sum_{r=0}^{r_{\max}} \left(\frac{A^r (a+r)!}{r!} \sum_{s=0}^{a+r+1} \frac{i^{r+2s}}{(a+r-s+1)!s!} I_{2,rs} \right),$$

where

$$I_{2,rs} = \int_0^1 \zeta^c (1-\zeta)^{a+r+1-s} \exp(iC\zeta) \left(\int_0^{1-\zeta} \eta^{b+s} \exp(iB\eta)\, \mathrm{d}\eta \right) \mathrm{d}\zeta. \tag{5.22}$$

The procedure to evaluate Equation (5.22) depends on the values of B. Hence, another branching is considered.

5.4.2.1 Cases from 12 to 14 ($A \to 0, B \nrightarrow 0$).

If $B \nrightarrow 0$, we develop the integral over η applying Equation (5.12). Thus,

$$\begin{aligned} I_{2,rs} \;=\; & (b+s)! \Bigg(\exp(iB) \sum_{t=0}^{b+s} \frac{i^{t-1}}{(b+s-t)!B^{t+1}} \\ & \int_0^1 \zeta^c (1-\zeta)^{a+b+r-t+1} \exp(i(C-B\zeta)\, \mathrm{d}\zeta \\ & - \frac{i^{b+s-1}}{B^{b+s+1}} \int_0^1 \zeta^c (1-\zeta)^{a+r-s+1} \exp(iC\zeta)\, \mathrm{d}\zeta \Bigg). \end{aligned} \tag{5.23}$$

Three cases have to be considered depending on the values of C and $C-B$. All of them are solved by first using the binomial theorem, Equation (5.14), second applying Equation (5.12) and/or Equation (5.13), and finally using Appendix D.

5.4.2.2 Cases 15 and 16 ($A \to 0, B \to 0$).

If $B \to 0$, the integral over η in Equation (5.22) is carried out using Equation (5.13). Thus,

$$I_{2,rs} = \sum_{t=0}^{t_{\max}} \frac{(iB)^t}{t!(b+s+t+1)} \int_0^1 \zeta^c (1-\zeta)^{a+b+r+t+2} \exp(iC\zeta)\, \mathrm{d}\zeta. \tag{5.24}$$

After applying the binomial theorem, Equation (5.14), both cases 15 and 16 are solved by using the corresponding method in Appendix D.

5.5 Example of a practical application: the PUM enriched with plane waves

An important application of the semi-analytical rule presented in this work is the computation of the highly oscillatory integrals that appear when the Helmholtz equation is solved using the Partition of Unity Method enriched with plane waves. The Helmholtz equation is the time-harmonic version of the wave equation, namely:

$$\Delta u + k^2 u = 0 \quad \text{in } \Omega, \tag{5.25}$$

where k is the wavenumber, Δ is the Laplace operator, Ω is the problem domain, and the unknown u is, for instance, the acoustic pressure, the wave height, or the electro-magnetic potential. Equation (5.25) is complemented by a Robin boundary condition

$$\frac{\partial u}{\partial n} - \tau k u = g \qquad \text{in } \Gamma = \partial\Omega, \tag{5.26}$$

where n is the outward normal to the boundary, τ is the complex transmission coefficient and g is the Robin independent term. We assume that domain Ω is discretized into a tetrahedral mesh composed of n_n nodes. The weak form of the problem is stated as: find $u_{h,q} \in \mathcal{W}_{h,q}$ such that

$$\int_\Omega (k^2 u_{h,q}\bar{v} - \nabla u_{h,q} \cdot \nabla \bar{v})\, \mathrm{d}\Omega + \int_\Gamma \tau k u_{h,q}\bar{v}\, \mathrm{d}\Gamma = -\int_\Gamma g\bar{v}\, \mathrm{d}\Gamma, \qquad \forall v \in \mathcal{W}_{h,q}, \tag{5.27}$$

where $\bar{\cdot}$ denotes complex conjugate,

$$\mathcal{W}_{h,q} = \left\{ v \,\middle|\, v = \sum_{m=1}^{n_n} N_m \left(\sum_{r=1}^{q} a_{m,r} W_{m,r} \right) \right\} \tag{5.28}$$

is the solution space corresponding to a mesh characterized by an element size h and q plane waves (enrichment functions) pasted at each node (patch), N_m is the standard first-order polynomial shape function (hat function) associated with the m-th node, and $a_{m,r}$ is the unknown complex coefficient associated with the r-th plane wave at the m-th node, namely

$$W_{m,r}(\mathbf{x}) = \exp\big(ik_m\,\mathbf{e}_r \cdot (\mathbf{x} - \mathbf{x}_m)\big), \tag{5.29}$$

k_m and $\mathbf{x}_m$ being the wavenumber and coordinates vector of the m-th node, and $\mathbf{e}_r$ the unit vector corresponding to the r-th plane wave direction.

According to equations (5.28) and (5.29), the PUM approximation has the form

$$u_{h,q}(\mathbf{x}) = \sum_{m=1}^{n_n}\sum_{r=1}^{q} a_{m,r}\phi_{m,r}(\mathbf{x}),$$

where $\phi_{m,r}$ is the approximation function associated with the m-th node and the r-th direction,

$$\phi_{m,r}(\mathbf{x}) = N_m(\mathbf{x})W_{m,r}(\mathbf{x}) = N_m(\mathbf{x})\exp\big(ik_m\,\mathbf{e}_r \cdot (\mathbf{x} - \mathbf{x}_m)\big). \tag{5.30}$$

The surface integrals appearing in Equation (5.27) can be computed using the 2D methods proposed in Bettess et al. (2003); Sugimoto et al. (2003). Here we focus on the efficient and accurate evaluation of the volume integral. Specifically, the volumetric elemental contribution to the system matrix is obtained by introducing this set of approximation functions into the weak form of the problem. Thus, integrating over the element $\Omega^{(e)}$ we obtain

$$\begin{aligned} K^{(e)}_{mr,ns} &= \int_{\Omega^{(e)}} [k^2\phi_{n,s}\bar{\psi}_{m,r} - \nabla\phi_{n,s}\cdot\nabla\bar{\psi}_{m,r}]\,\mathrm{d}\mathbf{x} \\ &= \exp\big(i(\bar{k}_m\mathbf{e}_r\cdot\mathbf{x}_m - k_n\mathbf{e}_s\cdot\mathbf{x}_n)\big)\int_{\Omega^{(e)}} f_{mr,ns}(\mathbf{x})\exp\big(i(-\bar{k}_m\mathbf{e}_r + k_n\mathbf{e}_s)\cdot\mathbf{x}\big)\,\mathrm{d}\mathbf{x}, \end{aligned} \tag{5.31}$$

where $m, n = 1, \ldots, n_n$, $r, s = 1, \ldots, q$,

$$\begin{aligned} f_{mr,ns}(\mathbf{x}) =& k^2(\mathbf{x})N_m(\mathbf{x})N_n(\mathbf{x}) - (\nabla N_m(\mathbf{x}) \\ &- i\bar{k}_m N_m(\mathbf{x})\mathbf{e}_r)\cdot(\nabla N_n(\mathbf{x}) + ik_n N_n(\mathbf{x})\mathbf{e}_s) \end{aligned} \tag{5.32}$$

is a non-oscillatory function, and $\psi_{m,r}$ is the test function associated with the m-th node and the r-th direction, which has the same form as the approximation function $\phi_{m,r}$ in Equation (5.30). Note that the integral in Equation (5.31) is a particular case of Equation (5.1) with $\mathbf{v} = -\bar{k}_m\mathbf{e}_r + k_n\mathbf{e}_s$.

5.6 Numerical experiments

In this section we present three examples that involve the integration of highly oscillatory functions over tetrahedra, in order to test the semi-analytical integration rule proposed in this work. Specifically, we compare its performance with the one of the standard Gauss-Legendre quadrature.

In the first example, several non-oscillatory functions are considered and the product of each of them and a complex exponential is integrated over a single tetrahedral element. They were run on a personal computer with a processor i7-3770 8x3.40 GHz with 16 GB of RAM memory.

Examples 2 and 3 deal with practical acoustic problems solved with the PUM enriched with plane waves. They have been computed in a machine Dell Power Edge R630 Xeon E5-2667 v3 (2x8x3.2 GHz/20MB cache, 2133Mhz FSB) with 62 GB of available memory.

In the legends of the figures, acronym SA denotes the solutions obtained with the Semi-Analytical integration rule, and similarly GL denotes the solutions obtained with a Gauss-Legendre quadrature. All the developments are coded in MATLAB R2013b.

5.6.1 Integration of the product of polynomials and a complex exponentials over a tetrahedron

The objective of this example is to test the performance of the semi-analytical rule by comparing its accuracy and CPU time consumption with those of the standard Gauss-Legendre quadrature. To this end, the product of smooth functions and a complex exponential is integrated over a single tetrahedron (Equation (5.1)). The tetrahedron is defined by nodes $\mathbf{x}_1 = [1, 1, 1]$, $\mathbf{x}_2 = [2, 0, 0]$, $\mathbf{x}_3 = [2, 2, 2]$ and $\mathbf{x}_4 = [1, 0, 3]$. Vector $\mathbf{v}$ is written as $\mathbf{v} = v \times [1, 1, 1]$, with $v = \{2, 4, 10, 20, 40\}$, corresponding to 1.09, 2.19, 5.47, 10.94 and 21.88 wavelengths per element, respectively. We consider three non-oscillatory functions: $f_1(\mathbf{x}) = 1$, $f_2(\mathbf{x}) = r^2(\mathbf{x})$ and $f_3(\mathbf{x}) = r^4(\mathbf{x})$, where $r(\mathbf{x})$ is the distance from $\mathbf{x}$ to the reference point $\mathbf{x}_0 = [0, 0, 0]$. We have computed those integrals using the semi-analytical rule with $n_{SA} = 1, 2, \ldots, 10$ integration points per dimension, and the Gauss-Legendre quadrature with $n_{GL} = 3, 5, 7, 10, 15, 20, 30, 40, 50$ and 100 integration points per dimension.

We measure the accuracy of the integration rules by computing the relative error

$$r_I = \frac{|I - I_{ref}|}{|I_{ref}|}, \tag{5.33}$$

where I is the value computed using the corresponding method and I_{ref} is a reference value. Because Gauss-Legendre quadratures converge to the exact value of the integral when the number of integration points is increased, see Davis and Rabinowitz (1984), we set I_{ref} equals to the value of the integral computed using $n_{GL} = 300$ Gauss points per direction.

We have computed the relative error (5.33) of the integrals when the integrand is $f_1(\mathbf{x}) = 1$ using the semi-analytical rule for all the detailed values of the wavelengths per element and number of integration points per dimension, n_{GL}. For this integrand, the error is exclusively produced by the integration of the weights, and the interpolation error of the integrand is null (apart from round-off errors) regardless the number of integration points. The rule produces excellent results and the relative error remains very low ($r_I < 10^{-12}$) for all cases. Nevertheless, the error is still lower for small values of v, for instance $r_I < 10^{-14}$ for $v = 2$ and $v = 4$.

Figure 5.2 plots the relative error (5.33) of both integration methods against the integration CPU time for $f_2(\mathbf{x}) = r^2(\mathbf{x})$ and $f_3(\mathbf{x}) = r^4(\mathbf{x})$. We observe that, as we increase the number of Gauss points, the integrals calculated with the Gauss-Legendre quadrature tend to the reference value. The behavior of this quadrature is the same for both functions, requiring an increasing number of integration points to reach an acceptable accuracy when v grows, especially if the integrand oscillates more than 10 times in an element ($v > 20$). The relative error of the semi-analytical rule drastically decreases when we use $n_{SA} = p + 1$ integration points per dimension, p being the degree of $f(\mathbf{x})$. That is, $n_{SA} = 3$ and $n_{SA} = 5$ integration points for $f(\mathbf{x}) = r^2(\mathbf{x})$ and $f(\mathbf{x}) = r^4(\mathbf{x})$, respectively. Note that, according to Equation (5.3), this number coincides with the minimum number of Lagrange points required to exactly approximate the integrand except for round-off errors. It is important to point out that for both functions, the semi-analytical rule outperforms the Gauss-Legendre quadratures when the integrands have more than 10 wavelengths per element ($v > 20$).

Remark 5.4. *The main cost of the semi-analytical rule comes from the computation of the integration weights. In this sense, the scenario in the first example is unfavorable for the semi-analytical rule because only a single integral is computed with*

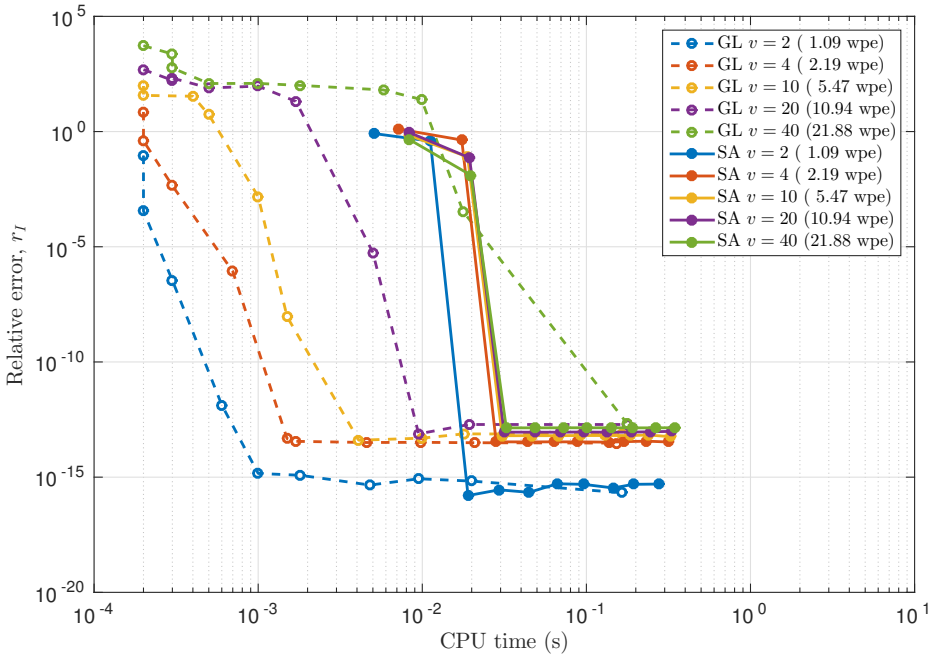

(a)

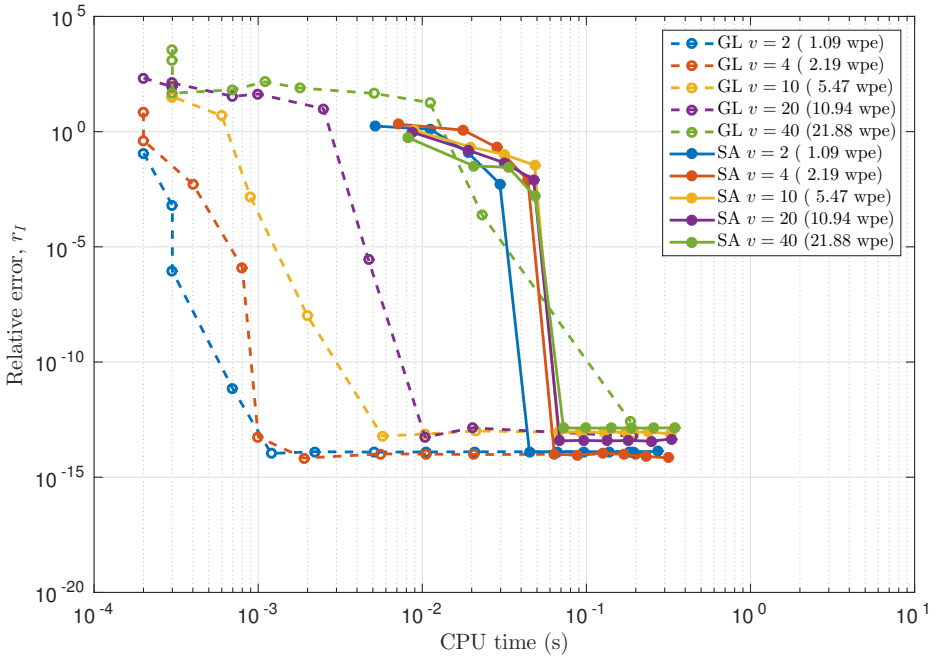

(b)

Figure 5.2: Relative error against integration CPU time for two non-oscillatory functions in Example 1: (a) $f_2(\mathbf{x}) = r^2(\mathbf{x})$; (b) $f_3(\mathbf{x}) = r^4(\mathbf{x})$. Number of integration points per dimension and element: $n_{SA} = 1, 2, \ldots, 10$; $n_{GL} = 3, 5, 7, 10, 15, 20, 30, 40, 50$ and 100.

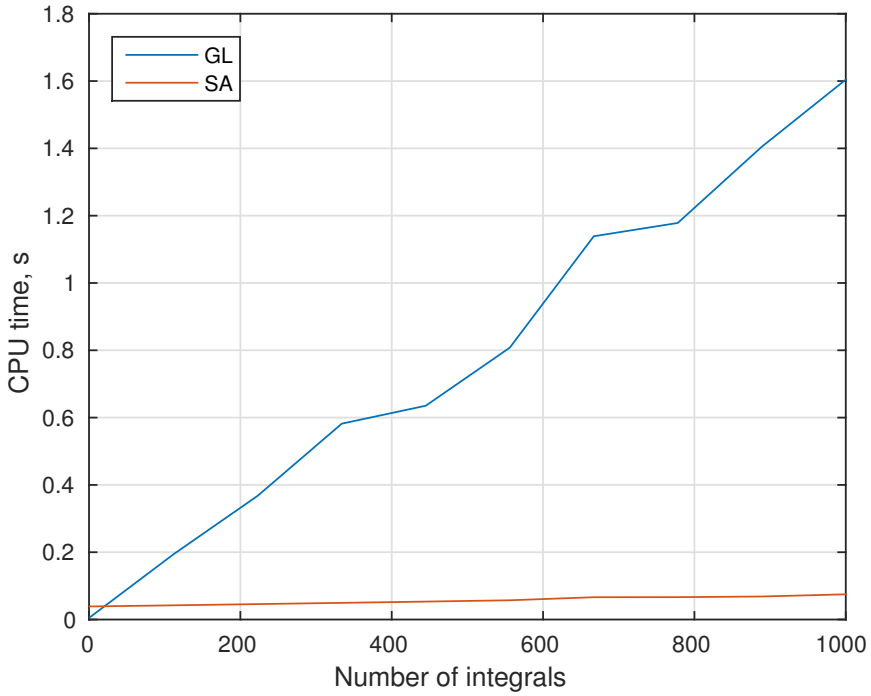

Figure 5.3: CPU time against number of integrals computed over the same element, with $v = 30$, $n_{GL} = 20$ and $n_{SA} = 3$.

the same set of weights. This is not the case of several practical applications such as the PUM enriched with plane waves. In this case, the products of several polynomial functions and the same complex exponential function have to be integrated over the same reference element when computing the elemental contributions (5.31)*. Therefore, the weights can be computed once for each element, drastically reducing the computational cost of the semi-analytical rule. This reduction is obtained for any value of the number of oscillations in the integration interval. In the context of highly-oscillatory integrands, this approach is competitive compared with the Gauss-Legendre quadrature because it requires a much lower number of integration points.*

Figure 5.3 illustrates the behavior indicated in the previous remark, by plotting the evolution of the CPU time against the number of times the same integral is computed over a given element for the same level of accuracy. The time consumed by the Gauss-Legendre quadrature linearly increases with a rate of 1.6 s for every 1000 integrals. On the contrary, the CPU time for the semi-analytical rule presents a moderate initial jump corresponding to the computation of the weights, and then it grows with

a small rate, that is practically flat with respect to the Gauss-Legendre slope. The overhead cost for each integral computation is associated with 1. the number of integration points and 2. the cost of functional evaluation at the integration points (recall that for Gauss-Legendre it involves computing costly complex exponential functions). Likewise, if the computational cost of evaluating the non-oscillatory function $f(\mathbf{x})$ is high, the Gauss-Legendre quadrature is further penalized because the integrand has to be evaluated a larger number of times.

5.6.2 Simulation of a single traveling wave using PUM

In this example we assess the accuracy and the performance of the semi-analytical rule in a practical application by comparing it with the standard Gauss-Legendre quadrature, when the propagation of a single time-harmonic traveling wave through a cubic domain is computed using the PUM enriched with plane waves.

First, we use the Frobenius norm to compare the global matrices obtained from the volumetric contributions of the weak form (5.27). Second, we solve the global linear systems, including the boundary conditions, and we compute the relative error in L^2-norm of the PUM solution with respect to the analytical solution. Specifically, we consider a single traveling plane wave with the following form:

$$u(\mathbf{x}) = A_{pw} \exp(ik\, \mathbf{e}_{pw} \cdot \mathbf{x}), \tag{5.34}$$

where $A_{pw} = 1$ Pa is the amplitude, $k = 0.52$ m^{-1} is the wavenumber and $\mathbf{e}_{pw} = [0, 0, 1]$ is the direction vector of the wave (towards positive z-axis). The plane wave directions are obtained thanks to the algorithm developed in Leopardi (2006). This algorithm has been recently used in Hospital-Bravo et al. (2016). In this example, the direction of propagation of the solution matches one of the directions of the set of plane waves basis and, thus, the traveling wave (5.34) belongs to the solution space (5.28). This cancels the error due to the quality of the approximation space, while focusing on the error produced during the integration step.

The size of the domain is $72 \times 72 \times 72$ m, and it is discretized using two different coarse meshes composed of 6 and 48 tetrahedra (6 and 3 wavelengths per element, respectively), pasting $q = 150$ plane waves at each node of the meshes. We solve Equation (5.25) for both geometry discretizations, prescribing the appropriate boundary condition (5.26). Equation (5.34) is introduced into the Robin conditions (5.26) with $\tau = i$, and the resulting independent term g is integrated over the whole

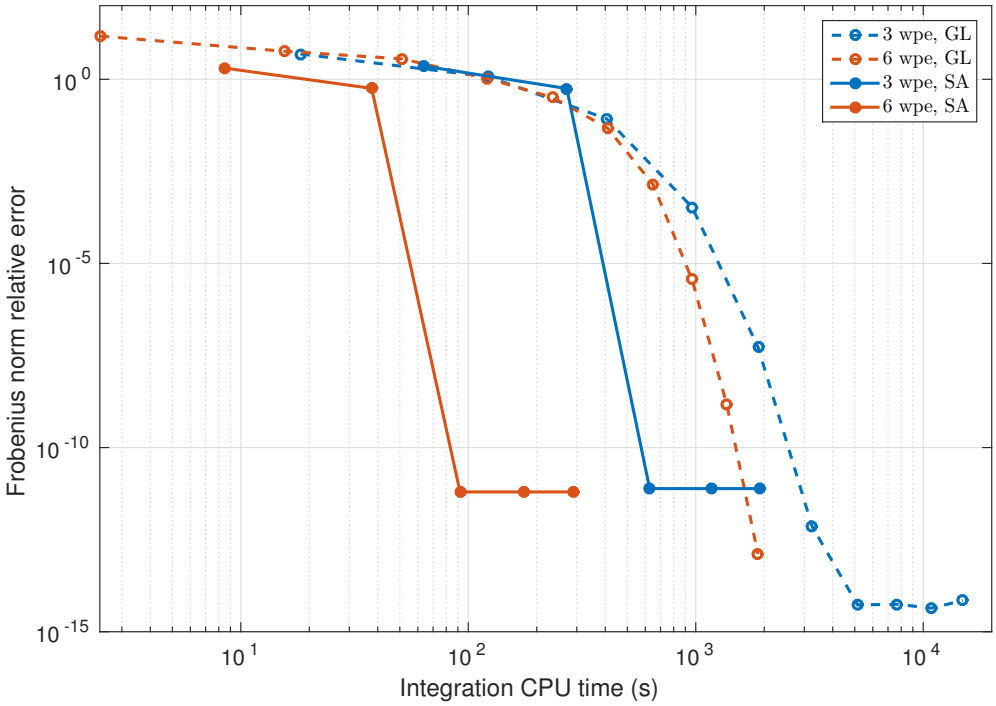

Figure 5.4: Relative error of the volume contribution to the system matrix in terms of the Frobenius norm against the integration CPU time in Example 2. Number of integration points per dimension and element: $n_{SA} = 1, \ldots, 5$; $n_{GL} = 5, 10, 15, \ldots, 50$.

boundary. We use the procedure proposed in Bettess et al. (2003), summarized in Appendix E, to compute the 2D integrals. The volume contributions to the global system matrix (5.31) are computed using the semi-analytical rule with $n_{SA} = 1, \ldots, 5$ integration points per dimension and element, and the Gauss-Legendre quadratures with $n_{GL} = 5, 10, 15, \ldots, 50$ integration points per dimension and element.

First, the system matrices obtained with both methods are compared by computing the relative error

$$r_m = \frac{\|\mathbf{K}_I - \mathbf{K}_{ref}\|_F}{\|\mathbf{K}_{ref}\|_F}, \tag{5.35}$$

where $\mathbf{K}_I$ is the system matrix computed using a numerical integration rule, $\mathbf{K}_{ref}$ is the system matrix computed using a reference quadrature, and $\|\cdot\|_F$ denotes the

Frobenius norm defined as

$$\|\mathbf{A}_{(m\times n)}\|_F = \sqrt{\sum_{i=1}^{m}\sum_{j=1}^{n}|a_{ij}|^2},$$

$|\cdot|$ being the complex modulus. We set as a reference value the matrix obtained using the Gauss-Legendre quadrature with $n_{GL} = 80$ integration points per dimension and element.

Figure 5.4 shows the relative error in terms of the Frobenius norm (5.35) against the required CPU time for the integration step. We observe that the semi-analytical rule with 3 or 4 integration points per dimension achieves an excellent accuracy ($r_m < 10^{-11}$) using less than one order of magnitude of the CPU time required by the Gauss-Legendre quadrature. As expected, we realize that using meshes with 6 waves per element (coarse meshes) is cheaper than using meshes with 3 waves per element (fine meshes). Note that this is also true for Gauss-Legendre quadratures. However, they require a larger number of integration points to achieve a similar accuracy.

After solving the systems, we measure the accuracy of the numerical solutions by computing the relative error in L^2-norm with respect to the analytical solution (5.34) as

$$r_{L^2} = \frac{\|u_{h,q}(\mathbf{x}) - u_a(\mathbf{x})\|_{L^2}}{\|u_a(\mathbf{x})\|_{L^2}}, \tag{5.36}$$

where $u_{h,q}(\mathbf{x})$ is the numerical solution, $u_a(\mathbf{x})$ is the analytical solution (5.34), and

$$\|\cdot\|_{L^2} = \sqrt{\int_\Omega |\cdot|^2 \,\mathrm{d}\Omega}.$$

Figure 5.5 plots the relative error (5.36) of the numerical solutions against the CPU time required by the integration step. We realize that the semi-analytical rule requires less than two orders of magnitude in CPU time to obtain a solution with the same accuracy than the obtained with the Gauss-Legendre quadrature. In addition, we also observe that using the semi-analytical procedure, the minimum error is achieved using 2 integration points per dimension and element.

5.6.3 Free-space propagation of a single noise source using PUM

This example compares the proposed semi-analytical rule and the standard Gauss-Legendre quadrature in terms of accuracy and required CPU time, when the free

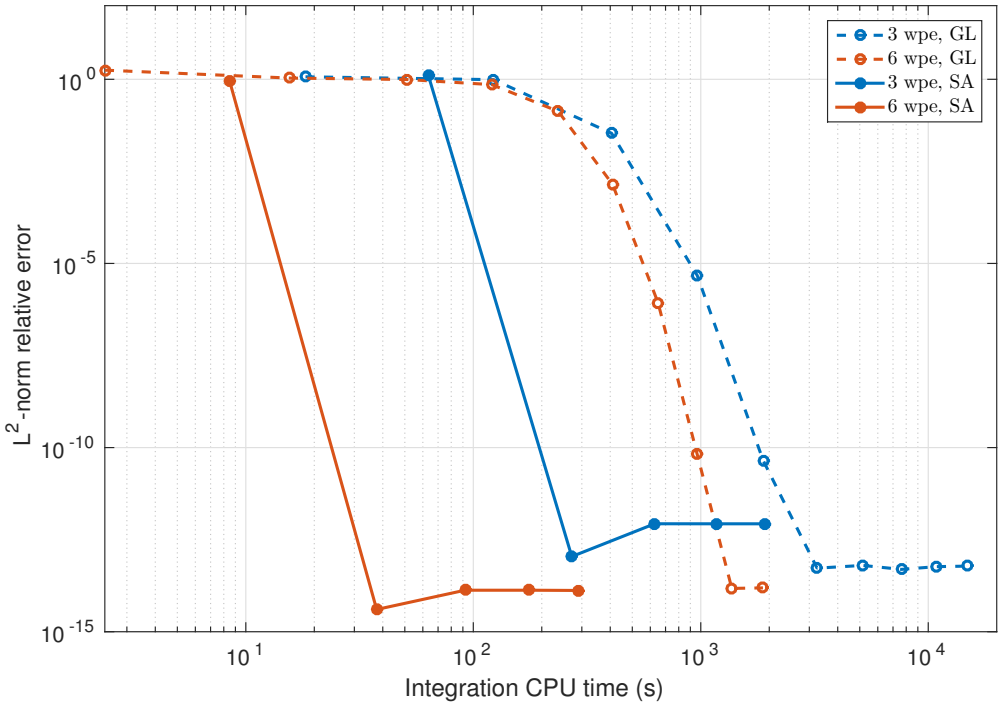

Figure 5.5: Relative error in L^2-norm against integration CPU time in Example 2. Number of integration points per dimension and element: $n_{SA} = 1, \ldots, 5$; $n_{GL} = 5, 10, 15, \ldots, 50$.

propagation of underwater noise is computed using the PUM enriched with plane waves. To perform this example, we follow the methodology that will be presented in Chapter 6 for the 3D numerical tool. We consider three cubic domains (Table 5.2) each of them is discretized using a tetrahedral mesh with 3 wavelengths per element, with $q = 330$ plane waves per node. The sound speed of the seawater is 1500 ms^{-1}. The example considers time-harmonic waves with a frequency of 250 Hz ($k = 1.05$ m^{-1}) generated by a single noise source located over the sea surface at $\mathbf{x}_s = [0, 0, \lambda/3]$, where λ is the wavelength (note that the noise source is placed slightly outside of the domain to avoid the singularity (Hospital-Bravo et al., 2016, Section 2.5)). The intensity of the source is selected such that it produces a pressure modulus of $p_{r_0} = 10$ Pa at a reference distance from the source of $r_0 = 1$ m. The combination of the values for the frequency, the sound speed and the number of wavelengths per element produces an element size of $h = 18$ m. The sea surface is treated as fully reflective, τ

Domain size (m)	# of elements (with PML)	Integration rule	t_{int} (s)	r_{L^2}
$36 \times 36 \times 18$	32	GL	4705.1	1.87E-002
		SA	579.9	1.88E-002
$72 \times 72 \times 18$	72	GL	19168.2	1.98E-002
		SA	2367.0	1.94E-002
$108 \times 108 \times 36$	192	GL	87185.0	6.01E-002
		SA	10752.6	6.01E-002

Table 5.2: CPU time and relative error in L^2-norm in Example 3, for each of the three domains and both integration rules.

$= 0$, and the input noise is introduced through the independent term g of the Robin condition (Equation (5.26)). Fully absorbing boundary conditions are prescribed at the lateral boundaries and sea bottom, using the PML technique Berenger (1994). The PMLs include a linear distribution for the attenuation parameter, characterized by a maximum value $\sigma_{\text{PML,max}} = 30\ \text{s}^{-1}$.

The analytical solution of the pressure field, $p_a(\mathbf{x})$, for this problem (homogeneous medium and uniform wavenumber) can be approximated by (Kinsler et al., 1999, Chapt. 5):

$$p_a(\mathbf{x}) = p_{r_0} \frac{r_0}{r(\mathbf{x})} \exp\Big(ik\big(r(\mathbf{x}) - r_0\big)\Big),$$

where $r(\cdot)$ is the distance to the point source $\mathbf{x}_s$. We have performed the integration step of this problem by means of the semi-analytic rule with $n_{SA} = p + 1 = 4$ integration points per element and dimension, because the non-oscillatory part of the integrands has a degree of $p = 3$ (taking into account the variation in the weak form produced by the PMLs), and the Gauss-Legendre quadrature with 25 integration points per element and dimension. Figure 5.6 shows the real part of the pressure field for the second domain obtained with the semi-analytical rule.

The accuracy of the numerical solutions is measured by computing the relative error in L^2-norm, according to (5.36). Table 5.2 details the accuracy and the required CPU time using both integration methods. We notice that for each domain, and for the same level of accuracy, the CPU time required by the semi-analytical rule is almost one order of magnitude smaller than the time required by the Gauss-Legendre quadrature.

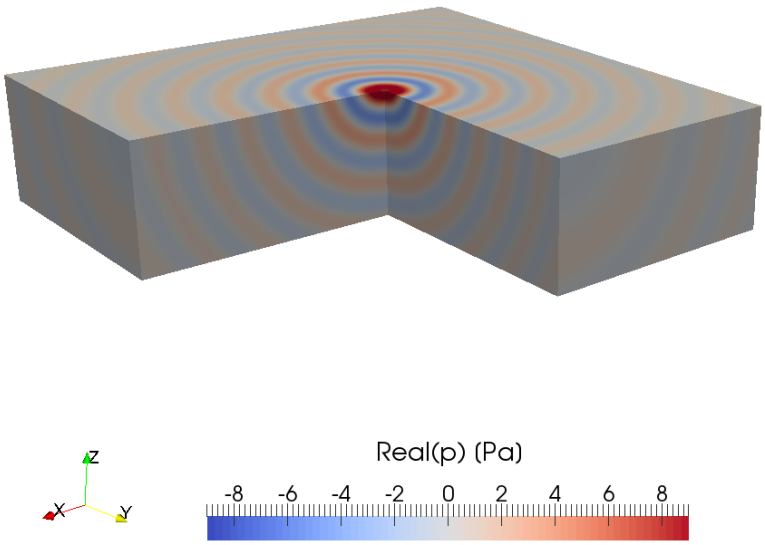

Figure 5.6: Real part of the pressure field obtained using the semi-analytical integration rule for the second domain in Example 3.

5.7 Concluding remarks

In this chapter we detail a novel semi-analytical rule to compute the integral of highly oscillatory functions over a tetrahedron. The integrand is expressed as the product of a non-oscillatory part and a complex exponential function that models the oscillatory part. The rule is designed to be exact, except round-off errors, for integrals with a polynomial non-oscillatory part. This is of interest for a wide range of applications such us the numerical solution of the Helmholtz equation by the PUM enriched with plane waves. In these cases, $p + 1$ integration points per dimension should be considered, p being the degree of the polynomial.

The key point of the proposed rule is to approximate the non-oscillatory part using Lagrange interpolation, that is an exact representation (up to round-off errors) for polynomials. Then, the Lagrange polynomials are linearly decomposed in terms of the appropriate set of monomials. In order to integrate the products of these monomials with a complex exponential over a tetrahedral element, our procedure identifies 16

possible cases that lead to a collection of 1D highly oscillatory integrals. For these kind of integrals we propose a scheme that selects an appropriate 1D analytical integration procedure that provides the required accuracy with a reduced computational cost.

The examples clearly show that the proposed rule efficiently integrates, both in terms of accuracy and CPU time, the product of a polynomial and a complex exponential function over tetrahedra. Specifically, it provides relevant CPU time savings for the same level of accuracy, compared with the standard Gauss-Legendre rules, in either of these situations: *1.* when the integrands have more than 10 oscillations in the integration interval; *2.* when the semi-analytical rule is applied to compute multiple integrals with the same oscillatory part (same arguments for the complex exponential). In this case, the integration weights can be pre-computed producing substantial CPU time reductions. It is important to highlight that this is the case of the integrals arising in the plane waves enriched PUM.

It is worth to notice that if the evaluation of the integrand is computationally expensive, then the semi-analytical rule is even more competitive because it involves a smaller number of integration points than the Gauss-Legendre quadratures.

Chapter 6

3D model for underwater acoustics

In this chapter, we extend the 2D model presented in Chapter 4 to 3D domains. The Helmholtz equation and its boundary conditions are rewritten in a straightforward manner. The mathematical modeling of the different physical phenomena, i.e. sea-water absorption, interference, reflection, refraction and diffraction, is also extended and intrinsically considered into the governing equation. The analytical expression of the independent term in the Robin boundary condition, which is related to the noise generation of point sources, see Section 4.2.4, is properly updated.

As in the 2D case, the PUM is also well-suited to solve the Helmholtz equation, since the enrichment is composed of plane waves, which are analytical solutions of the Helmholtz equation in 3D. To determine the 3D directions of the plane waves, we use the algorithm presented in Leopardi (2006). Perfectly Matched Layers (PMLs) are also placed at the lateral artificial boundaries of the domain in order to avoid spurious reflections.

The discretization of the domain is performed using *tetrahedral* elements to better capture realistic geometries. Thus, the *semi-analytical* integration rules for highly oscillatory functions developed in Chapter 5 are extensively used to compute the elemental contributions.

Finally, several numerical examples illustrating the main applications of the proposed technique are presented.

6.1 Introduction

The 3D numerical modeling of highly oscillatory wave problems has attracted the interest of several research groups during the last two decades. For instance, Laghrouche et al. (2003) is one of the pioneer works that extended an existing 2D model for scattering problems to the 3D case. The scattered field produced by the incidence of a plane wave over a sphere was accurately computed using the Partition of the Unity Method with plane waves. The plane wave directions were obtained as the intersection of evenly spaced parallels and meridians on the unit sphere. The numerical integration is performed by a high-order Gauss-Legendre quadrature. Perrey-Debain et al. (2004) extend the previous work to boundary elements and non-trivial scattering geometries. The direction of the plane waves are also evenly distributed on the unit sphere and a high-order Gauss-Legendre quadrature is still used. In Huttunen et al. (2004), the discontinuous Ultra-Weak Variational Formulation, see 3.2.4.4, is applied to 3D problems. The work compares the behavior of Perfectly Matched Layers with conventional low-order absorbing boundary conditions. As in the case of the mentioned PUM-based models, plane waves are used and the integration is performed by a high-order quadrature. Similarly, Tezaur and Farhat (2006) also consider a Discontinuous Galerkin Method (DGM) where the continuity between elements is weakly imposed using Lagrange multipliers. The method is based on a Discontinuous Enriched Method (DEM), see 3.2.4.4, but without the subspace generated by the polynomial functions. The authors compared their formulation with the standard high-order Galerkin method. The discretization of the domain is performed using hexahedral elements. The volume integrals are transformed into surface integrals applying the divergence theorem. The resulting surface integrals are analytically evaluated provided that the element faces are planar. Massimi et al. (2008) extend the previous formulation to the analysis of layered media, considering evanescent modes. Recently, Yang et al. (2015, 2018) improved the pioneer formulation Perrey-Debain et al. (2004) by implementing an exact integration algorithm based on the successive use of the Green's theorem. The examples considered a uniform spatial distribution of the wavenumber and tetrahedral elements. In Mahmood et al. (2017), the PUM is successfully applied to the elastic wave propagation, by enriching both P and S waves. The paper explores the performance of several approaches for selecting the plane wave directions. In this work, conventional high-order Gauss-Legendre are used to compute the elemental integrals.

In this chapter, we extend the PUM formulation presented in Chapter 4 to 3D problems. Similar to Laghrouche et al. (2003); Perrey-Debain et al. (2004); Yang et al. (2015); Mahmood et al. (2017); Yang et al. (2018), we paste at each node a set of plane waves. However, we use the set of wave directions proposed in Leopardi (2006). This algorithm is easy to implement and divides the unit sphere into regions of equal area. In this way, plane waves with similar direction of propagation are avoided. Moreover, our model considers *complex* and *non-uniform* wavenumber. As detailed in Section 4.2.2, the imaginary part of the wavenumber allows considering the seawater absorption phenomenon without the need of including further numerical artifacts. In addition, the use of non-uniform wavenumber allows simulating more realistic scenarios such as vertically stratified oceans. Finally, to reduce the computational cost of high-order Gauss-Legendre quadratures, we use the semi-analytical integration rule presented in Chapter 5.

The rest of the chapter is structured as follows. In Section 6.2 we review the mathematical model developed in Section 4.2 and extend it to the 3D case. In Section 6.3 we describe the main features of the numerical model, including an efficient 3D distribution for the plane wave directions. In Section 6.4, we present several examples that illustrate the capabilities of the proposed method. Finally, in Section 6.5 we summarize the achievements.

6.2 3D modeling of the underwater noise propagation

As in the 2D version of the model, the 3D model considers the harmonic version of the wave equation. That is, the complex pressure field is the solution of the Helmholtz equation in a bounded domain, see Section 3.2.4.

6.2.1 Problem statement

For the sake of self-completeness, the equations from Section 4.2.1 describing the strong form of the problem are recovered:

$$\begin{aligned} &\Delta p + k^2 p = 0 \quad \text{in } \Omega, \\ &\frac{\partial p}{\partial n} - \tau k p = g \quad \text{in } \Gamma = \partial\Omega. \end{aligned} \tag{6.1}$$

The weak form of this problem reads: find $p \in H^1(\Omega)$ such that

$$\mathcal{B}(p, v) = \mathcal{L}(v) \qquad \forall v \in H^1(\Omega), \tag{6.2}$$

where

$$\begin{aligned} \mathcal{B}(p, v) &= \int_\Omega (k^2 p\bar{v} - \nabla p \cdot \nabla \bar{v}) \, \mathrm{d}\Omega + \int_\Gamma \tau k p \bar{v} \, \mathrm{d}\Gamma \\ \mathcal{L}(v) &= -\int_\Gamma g\bar{v} \, \mathrm{d}\Gamma. \end{aligned}$$

Now Ω is a 3D volume and Γ is its boundary surface.

6.2.2 Modelization of the physical properties

Section 4.2 details how we incorporate the physical phenomena and parameters associated to underwater noise propagation into the model. All equations apply except for (4.8) and (4.10). In a 3D geometry, Equation (4.8) associated to the pressure field generated by a 2D point sources in a homogeneous and lossless medium must be updated by

$$p(\mathbf{x}) = p_{r_0} \frac{r_0}{r(\mathbf{x})} \exp[ik(r(\mathbf{x}) - r_0)] \ .$$

As a direct consequence, the independent term at the Robin equation that introduces the noise input into the problem takes the form

$$\begin{aligned} g(\mathbf{x}) &= \frac{\partial p_a(\mathbf{x})}{\partial n} - k(\mathbf{x})\tau(\mathbf{x}) p_a(\mathbf{x}) \\ &= \left(\frac{ik_0 r(\mathbf{x}) - 1}{r^2(\mathbf{x})} \, (\mathbf{x} - \mathbf{x_s}) \cdot \mathbf{n} - k(\mathbf{x})\tau(\mathbf{x}) \right) p_a(\mathbf{x}) \ , \end{aligned} \tag{6.3}$$

and is considered instead of Equation (4.10).

6.3 Numerical model

This section summarizes the basic equations derived in Section 4.3 and adds specific issues considered for the 3D case.

6.3.1 Partition of unity method. 3D case

Domain Ω is discretized using a **tetrahedral** mesh with characteristic size h, see Section 6.3.2, and a total number of nodes n_{nod}. The classical piecewise trilinear

shape functions associated to the m-th node of the mesh are denoted by N_m, for $m = 1, \ldots, n_{\text{nod}}$. The support of N_m is a patch composed by the elements sharing node m.

The partition of unity space $\mathcal{W}_{h,q}$ reads

$$\mathcal{W}_{h,q} = \left\{ v \,\middle|\, v = \sum_{m=1}^{n_{\text{nod}}} N_m \left(\sum_{r=1}^{q} a_{m,r} W_{m,r} \right) \right\}, \tag{6.4}$$

where q is the number of plane waves (enrichment functions) pasted at the m-th node (patch), $a_{m,r}$ is the complex coefficient (amplitude) of the r-th plane wave associated to the m-th node, namely

$$W_{m,r}(\mathbf{x}) = \exp\left(ik_m \, \mathbf{e_r} \cdot (\mathbf{x} - \mathbf{x_m})\right),$$

being k_m the wavenumber at the m-th node, $\mathbf{e_r}$ the r-th propagation direction, and $\mathbf{x_m}$ the coordinates of the m-th node.

According to Equation (6.4), the PUM approximation has the form

$$p_{h,q}(\mathbf{x}) = \sum_{m=1}^{n_{\text{nod}}} \sum_{r=1}^{q} a_{m,r} \phi_{m,r}(\mathbf{x}),$$

where $\phi_{m,r}$ is the approximation function associated to the m-th node and the r-th direction,

$$\begin{aligned} \phi_{m,r}(\mathbf{x}) &= N_m(\mathbf{x}) W_{m,r}(\mathbf{x}) \\ &= N_m(\mathbf{x}) \exp\left(ik_m \, \mathbf{e_r} \cdot (\mathbf{x} - \mathbf{x_m})\right). \end{aligned} \tag{6.5}$$

The selection of direction vectors $\mathbf{e_r}$ for the plane waves is straightforward in the 2D case, but not trivial in the 3D case. The first implementations of the PUM applied to acoustic problems used a distribution of directions obtained from the intersections of evenly spaced parallels and meridians on the unit sphere Laghrouche et al. (2003). This approach leads to a concentration of directions near the poles. Later, other enriched methods used distributions of directions based on evenly spaced points on the unit cube Tezaur and Farhat (2006); Massimi et al. (2008). The concentration of directions is less significant but is still present around the vertices of the unit cube, and the number of directions cannot be an arbitrary number. Different approaches to select the direction vectors are based on electrostatic analogies. For instance, the Coulomb Force Method in Peake et al. (2014) generates a distribution of points with equal electrostatic charge over the sphere that are in equilibrium.

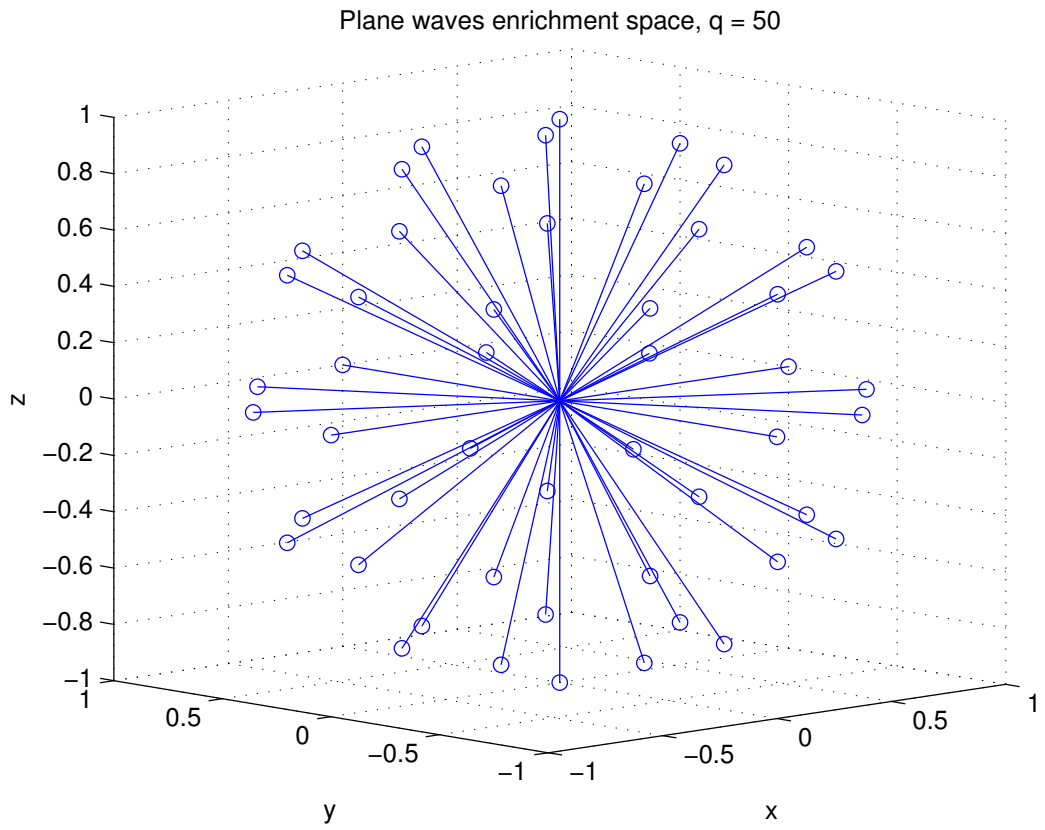

Figure 6.1: Example of a distribution of 50 plane wave directions obtained using the algorithm proposed by Leopardi (2006).

In this work, we use the recursive zonal equal-area partition proposed by Leopardi (2006). This method is easy to implement and provides a procedure to recursively divide the unit sphere into rings and sectors until a set of q patches with equal area is achieved (recursive zonal equal-area partition). The number of patches can be selected as any integer number. The q direction vectors are placed at the center of each patch, according to spherical coordinates, taking the form

$$\mathbf{e_r} = [\sin(\theta_r)\cos(\varphi_r), \sin(\theta_r)\sin(\varphi_r), \cos(\theta_r)],$$

where θ_r and φ_r are the angle with the z axis and the longitude coordinate of the n-th plane wave, respectively, both in radians. Figure 6.1 shows the plane wave directions distribution for $q = 50$, as an example.

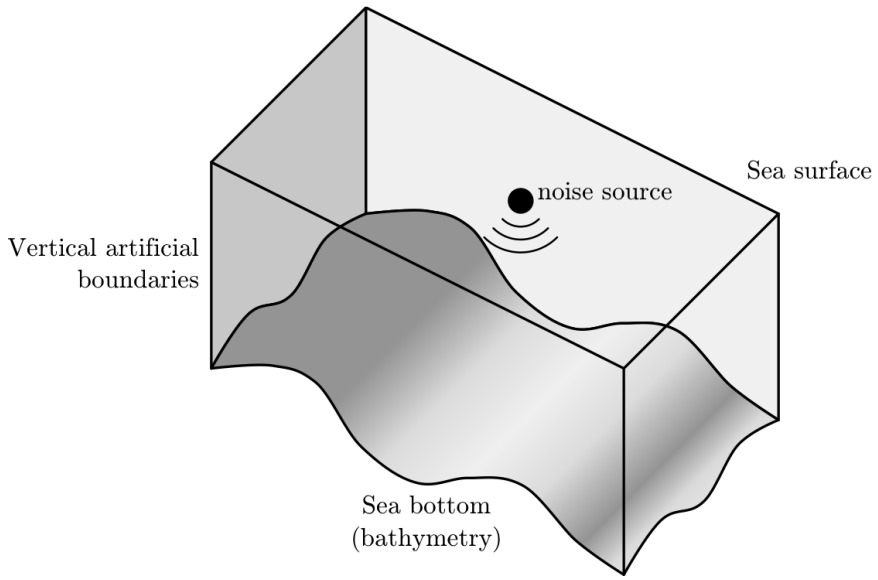

Figure 6.2: Conceptual example of a 3D domain.

6.3.2 Domain discretization

In the 3D case, the region of interest is a volume of marine waters enclosed by the sea surface, the sea bottom and four artificial lateral surfaces that truncate the unbounded domain of propagation, see Figure 6.2.

The selection of the discretization scheme is constrained by the computational cost of the PUM method. In particular, we highlight that the integration of shape functions with complex exponentials is not trivial and requires a special treatment, see Section 4.3.3 for 2D integrals and Chapter 5 for the 3D case. In fact, the computational cost involved in the integration of the interior elements represents an important part of the total cost. We have developed efficient integration techniques for rectangular hexahedra, and tetrahedra. However, it is not possible to approximate properly the bathymetry by using only rectangular hexahedra. In addition, it is not possible to combine these two types of elements in a conforming manner without using a third type of element such as pyramids. For these two reasons, in this applications we use tetrahedral meshes.

In general, three-dimensional marine domains have a smooth bottom boundary. Hence, the overall shape of the domain is almost a rectangular hexahedron. The meshing strategy is the following. First, a structured non-rectangular hexahedral mesh is generated to fit the sea bottom, in such a way that the upper layers of

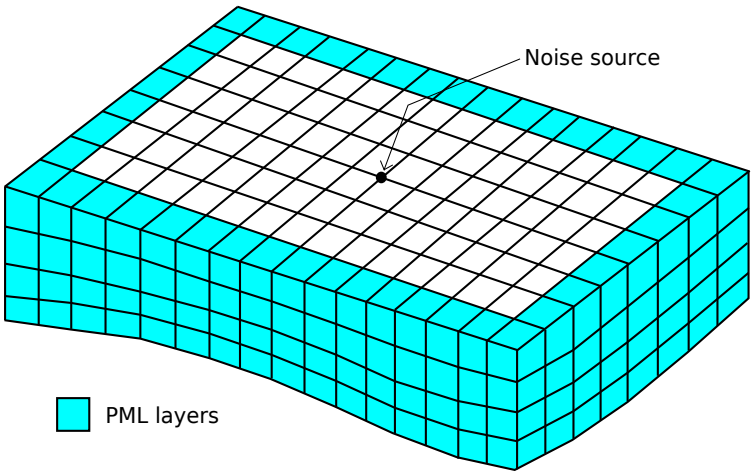

(a)

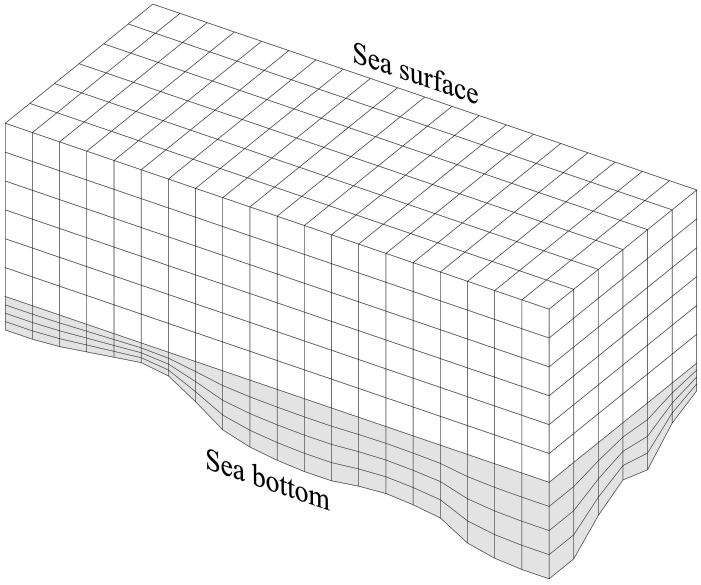

(b)

Figure 6.3: Preliminary discretizations of different domains into hexahedral elements: (a) including lateral PML layers; and (b) without PML layers.

elements are rectangular hexahedra (cuboids) of the same shape and size, and only the bottom layers are composed of non-rectangular hexahedra, similarly to the 2D case, see Figure 6.3(b). After that, the lateral PML layers are generated, see Figure 6.3(a). Finally, we use the technique presented in Dompierre et al. (1999) to transform each hexahedron into a set of 6 tetrahedra, allowing a matching between the faces and edges of the adjacent elements, see Figure 6.4.

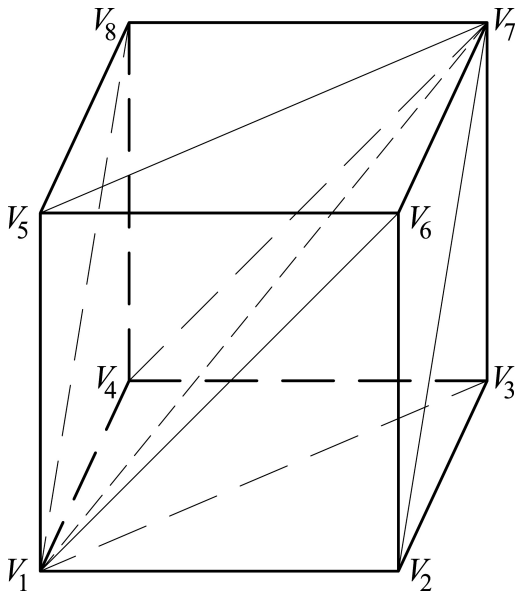

Figure 6.4: Decomposition of an hexahedron into six tetrahedra used in this work.

Note that if the wavenumber k of the upper layers of elements is uniform along x and y axes (only varies along the z axis), and thanks to the local definition of the shape functions, see Equation 6.5, it is possible to compute the element matrix only once for each of the six types of tetrahedron, in order to save integration CPU time.

Remark 6.1. *The same idea collected in Remark 4.5 can now be applied again in the 3D case. Equation* (5.31) *can be rewritten as*

$$\begin{aligned} K^{(e)}_{mr,ns} &= \int_{\Omega^{(e)}} [k^2 \phi_{n,s} \bar{v}_{m,r} - \nabla \phi_{n,s} \cdot \nabla \bar{v}_{m,r}] \, \mathrm{d}\mathbf{x} \\ &= \int_{\Omega^{(e)}} f_{mr,ns}(\mathbf{x}) \exp\left(i(-\bar{k}_m \mathbf{e}_r \cdot (\mathbf{x} - \mathbf{x}_m) + k_n \mathbf{e}_s \cdot (\mathbf{x} - \mathbf{x}_n)\right) \, \mathrm{d}\mathbf{x}, \end{aligned} \tag{6.6}$$

where $f_{mr,ns}$ is a function of the classical shape functions, their derivatives, and the wavenumber, see Equation (5.32)*. Therefore, it is straightforward to check that tetrahedral elements having the same geometry (shape and size), and the same distribution of the wavenumber k, have the same elemental matrix, thanks to the local definition of the plane waves. This way, to speed up the integration process, for each layer, and for each of the six tetrahedra that compose a hexahedral element, we compute their elemental matrix. Then, we reuse these elemental matrices for the equivalent tetrahedral elements in that layer.*

The lateral surfaces of the domain belong to vertical planes that should ideally behave as non-reflecting boundaries. Different kinds of artificial boundary conditions can be used on these lateral boundaries. On the one hand, low order absorbing boundary conditions (ABC) perform well for some propagation directions but introduce spurious reflections at some other wave propagation angles. For example, the Robin condition in Equation (6.1) with transmission coefficient $\tau = i$ and independent term $g = 0$ produces spurious numerical reflections for the wave rays reaching the boundary with an angle different to the normal direction. On the other hand, available higher order ABCs become more complex to implement and require more storage and computational resources Rappaport (1995).

Perfectly Matched Layers (PML) provide a strong absorption of the outgoing waves for any incident angle, without reflection at the interface. PMLs can be viewed as an analytic continuation of the Helmholtz equation into complex spatial coordinates, see Johnson (2007). The main restrictions of the method are the following: *1.* the medium must be homogeneous in the normal direction to the boundary, *2.* the boundary must be normal to a reference axis. Further details on this technique can be found in Berenger (1994). Figure 6.3(a) shows an example of a mesh of hexahedra with PML layers placed around the lateral boundaries.

6.3.3 Numerical integration

The discretization of the weak form of the problem, Equation (6.2), leads to the following three types of elemental integrals:

- Integrals over tetrahedral elements, coming from the contribution of the volumetric term:

$$\begin{aligned} K^{(e)}_{mr,ns} &= \int_{\Omega^{(e)}} [k^2 \phi_{n,s} \bar{v}_{m,r} - \nabla \phi_{n,s} \cdot \nabla \bar{v}_{m,r}] \, \mathrm{d}\Omega \\ &= \exp\left(i(\bar{k}_m \mathbf{e}_r \cdot \mathbf{x}_m - k_n \mathbf{e}_s \cdot \mathbf{x}_n)\right) \int_{\Omega^{(e)}} F_{mr,ns} \psi_{mr,ns} \, \mathrm{d}\Omega, \end{aligned} \tag{6.7}$$

  where

$$F_{mr,ns} = k^2 N_m N_n - (\nabla N_m - i\bar{k}_m N_m \mathbf{e_r}) \cdot (\nabla N_n + i k_n N_n \mathbf{e_s})$$

  is a non-oscillatory term, and

$$\psi_{mr,ns} = \exp\left(i(-\bar{k}_m \mathbf{e_r} + k_n \mathbf{e_s}) \cdot \mathbf{x}\right)$$

is a highly oscillatory term.

- Integrals over the triangular faces of the tetrahedral elements that are located on the domain boundary, coming from the Robin equation (6.1),

$$\begin{aligned} B^{(e)}_{mr,ns} &= \int_{\Gamma^{(e)}} \tau k \phi_{n,s} \bar{v}_{m,r} \, \mathrm{d}\Gamma \\ &= \exp\left[i(\bar{k}_m \mathbf{e_r} \cdot \mathbf{x_m} - k_n \mathbf{e_s} \cdot \mathbf{x_n}) \right] \int_{\Omega^{(e)}} F_{mr,ns} \, \psi_{mr,ns} \, \mathrm{d}\Gamma \end{aligned} \tag{6.8}$$

  where now the non-oscillatory term is

$$F_{mn,rs} = \tau k N_m N_n,$$

  and the highly oscillatory term is the same that appears in the volumetric integral, Equation (6.7).

- Integrals over the triangular faces of the tetrahedral elements that are located on the domain boundary, coming from the independent term g that appears in the Robin equation (6.1).

$$\begin{aligned} f^{(e)}_{mr} &= \int_{\Gamma^e} g \bar{v}_{m,r} \, \mathrm{d}\Gamma \\ &= \exp\left(i\bar{k}_m \mathbf{e_r} \cdot \mathbf{x_m} \right) \int_{\Gamma^e} \underbrace{g(\mathbf{x}) N_m(\mathbf{x})}_{\text{highly oscillatory}} \underbrace{\exp\left(\left(-i\bar{k}_m \mathbf{e_r} \cdot \mathbf{x} \right) \right)}_{\text{highly oscillatory}} \mathrm{d}\Gamma. \end{aligned} \tag{6.9}$$

The first two types of integrals are assembled into the global system matrix, while the third type is assembled into the right-hand side vector.

Equations (6.7), (6.8) and (6.9) can be written in the following general form:

$$I = \int_{\mathbf{X}} F(\mathbf{x}) \, \psi(\mathbf{x}) \, \mathrm{d}\mathbf{X},$$

where $\mathbf{X}$ is either a 2D or a 3D domain. To compute the integral in Equation (6.7), we use the 3D numerical integration scheme developed in Chapter 5. For Equation (6.8), we use the semi-analytical quadratures presented in 4.3.3. Finally, for (6.9), the integrand cannot be decomposed into a non-oscillatory term and a complex exponential one. That is, both F and ψ are highly oscillatory. Therefore, in this case, a standard high order Gauss-Legendre quadrature is applied.

6.4 Numerical experiments

In this section we present three examples that illustrate the accuracy and the capabilities of the three-dimensional implementation of the model. First, we detail one example that emphasizes two basic properties of the proposed method: its accuracy, and its ability to include multiple wavelengths inside an element. Second, we present two examples that illustrate the applicability of the model to underwater acoustics, both with single and multiple point sources. Specifically, we consider uniform and non-uniform spatial distributions for the sound speed (stratified ocean), different seawater absorption coefficients and different transmission coefficients at the sea bottom. For all the examples, the spatial coordinates and lengths are expressed in meters. For this work, we have used the built-in direct solving algorithm `mldivide`, included in MATLAB R2018b.

6.4.1 Single traveling wave

In this example we analyze the accuracy of the three-dimensional version of the developed method. To this end, we consider a single traveling plane wave, similarly to Section 5.6.2. However, in this example the propagation direction of the single wave does not belong to the set of directions determined by the plane wave basis. Two cases are considered. We first compute the solution for null seawater absorption $\alpha = 0$ dB/km, and then we compare it with the case of $\alpha = 100$ dB/km, see 2.1.3.1.

We consider a cubic domain $\Omega = [-9, 9] \times [-9, 9] \times [-9, 9]$ m of seawater ($c = 1500$ m/s). A single traveling plane wave is simulated, with an amplitude of $A_{pw} = 1$ Pa at a frequency of 1 kHz ($k = 4.19$ rad/m), with unit direction vector forming an angle of $\pi/5$ with respect to the positive z-axis and the same angle with respect to the positive x-axis, counterclockwise, $\mathbf{e_{pw}} = (0.475, 0.345, 0.809)$. Thus, the analytical solution of the problem is

$$u_a(\mathbf{x}) = A_{pw} \exp(ik\, \mathbf{e}_{pw} \cdot \mathbf{x}). \tag{6.10}$$

The mesh is composed of $5 \times 5 \times 5$ nodes (384 tetrahedra), with 3 wavelengths ($\lambda = 1.5$m) per element size ($kh = 6\pi$).

To perform a q-convergence analysis, the simulation is computed for several numbers of plane waves pasted at each node, q. Then, we measure the accuracy of the

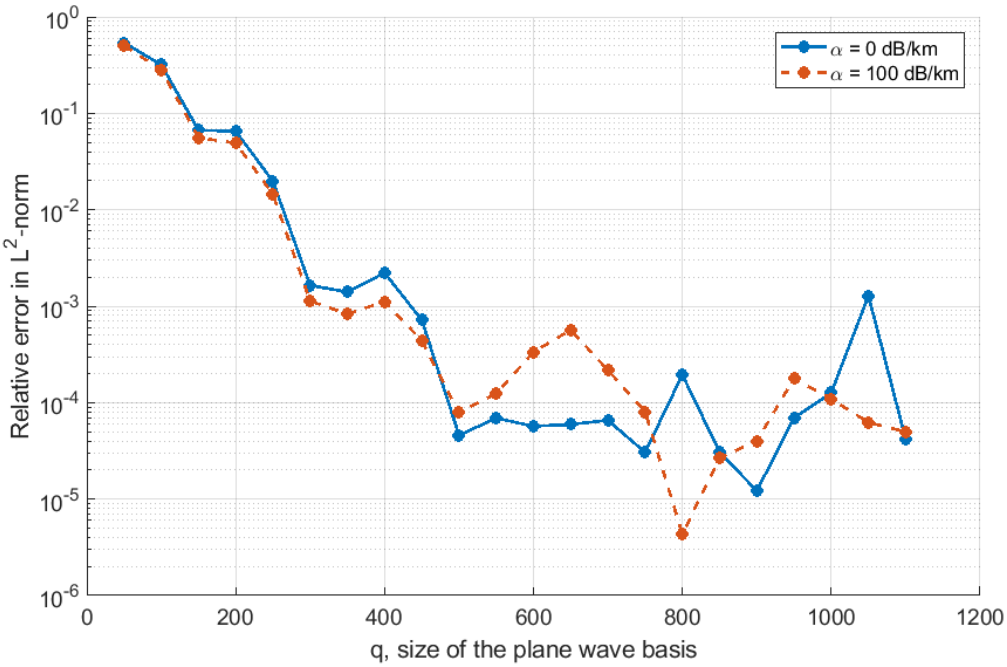

Figure 6.5: Relative error against the number of pasted plane waves per node q, for $\alpha = 0$ dB/km and $\alpha = 100$ dB/km.

numerical solutions by computing the relative error in L^2-norm as

$$r_{L^2} = \frac{\|u_{h,q}(\mathbf{x}) - u_a(\mathbf{x})\|_{L^2}}{\|u_a(\mathbf{x})\|_{L^2}}, \tag{6.11}$$

where $u_{h,q}(\mathbf{x})$ is the numerical solution, $u_a(\mathbf{x})$ is the analytical solution (6.10), and

$$\|\cdot\|_{L^2} = \sqrt{\int_\Omega |\cdot|^2 \, \mathrm{d}\Omega}.$$

Figure 6.5 shows the relative error in L^2-norm in Equation (6.11) against q, for $\alpha = 0$ dB/km and $\alpha = 100$ dB/km. In this example, the error exhibits a non-monotonic decrease as q increases. For small values of q, the error is monotonically reduced. However, for values above $q = 400$, the error stagnates. As reported by several authors, this behavior can be explained by the increasing ill-conditioning of the system matrix when a large number of plane waves is used to enrich the solution. For this example, the error is acceptable from an engineering point of view above $q = 250$.

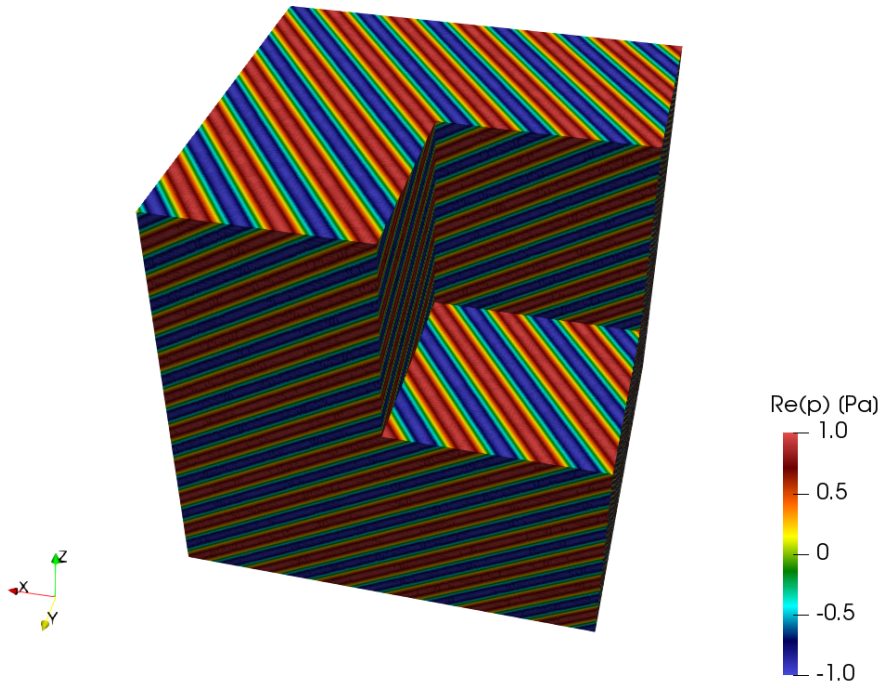

Figure 6.6: Real part of the pressure field in Example 1, without seawater absorption, q=300.

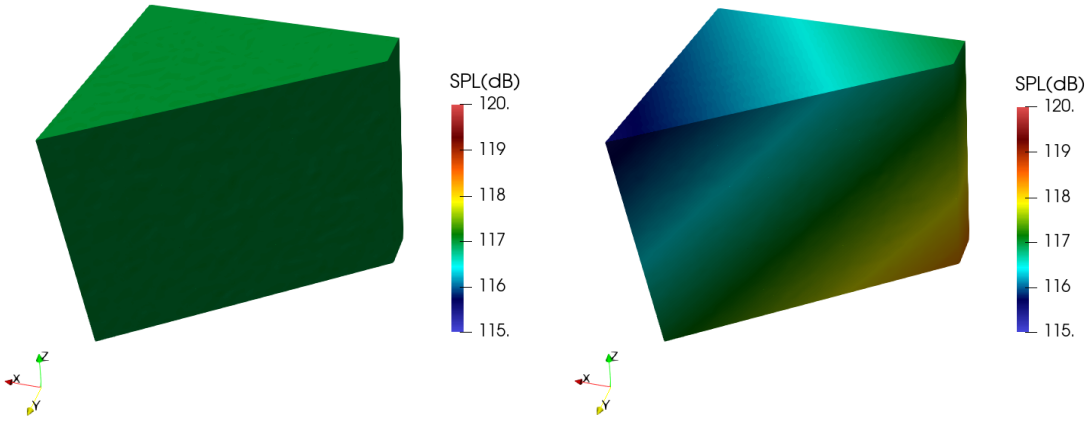

(a) (b)

Figure 6.7: SPL (dB) in Example 1, for q=300. Case a) null seawater absorption, case b) seawater absorption $\alpha = 100$ dB/km.

Figure 6.6 plots the real part of the solution for $q = 300$ and null absorption. The oscillatory behavior of the real part of the pressure field is clearly recognizable and no reduction in the amplitude appears. Figures 6.7(a) and 6.7(b) depict the SPL field for the cases of $\alpha = 0$ dB/km and $\alpha = 100$ db/km, respectively. It is important to point that with no absorption the SPL is uniform, as expected for a single traveling plane wave. On the contrary, for the case with positive absorption, the SPL decreases in the direction of the wave propagation.

6.4.2 Point source with PML's and non-uniform sound speed

In this example, we apply the simulating tool to analyze the 3D propagation of the noise generated by a single point source. The sea bottom is divided into two regions with different transmission coefficients. Two cases are simulated. First, we consider a uniform sound speed distribution $c = 1500$ m/s. Second, we consider a non-uniform vertical profile for the sound speed, with a gradient of -1 (m/s)/m (c decreases with depth), taking a value of 1500 m/s on the sea surface ($z = 0$). A null seawater absorption is considered, $\alpha = 0$ dB/km.

The domain of interest is a rectangular cuboid $\Omega = [-36, 36] \times [-36, 36] \times [-54, 0]$ m of seawater. The sea surface is considered as fully reflective ($\tau = 0$). The sea bottom is composed of two materials: a highly reflective seabed ($\tau = 0.1$) for $y \leq 0$ ('hard' material, high mismatch in the impedance), and lowly reflective seabed ($\tau = 0.9$) for $y > 0$ ('soft' material, low mismatch in the impedance). A PML is placed on the four lateral artificial boundaries of the domain, in order to simulate perfectly absorbing boundary conditions. These layers are characterized by a PML parameter $\sigma_{\text{PML,max}} = 25$ rad/s.

The example considers a single noise source generating spherical time-harmonic waves with a frequency of 250 Hz ($k = 1.05$ m^{-1}), and a modulus of $p_{r_0} = 1$ Pa (SPL = 117 dB) at a reference distance from the source of $r_0 = 1$ m. The source is located over the center of the sea surface at $\mathbf{x}_s = [0, 0, \lambda/3]$, where $\lambda = 6$ m is the wavelength. Note that the noise source is placed slightly outside of the domain to avoid a singularity at the source point, see details in Section 4.2.4.

According to Section 6.3.2, we first generate a hexahedral mesh composed of $4 \times 4 \times 3$ elements, the blue elements in Figure 6.8. The element size is set as $h = 18$ m in order to include three wavelengths per element size ($kh = 6\pi$). Then, a shell

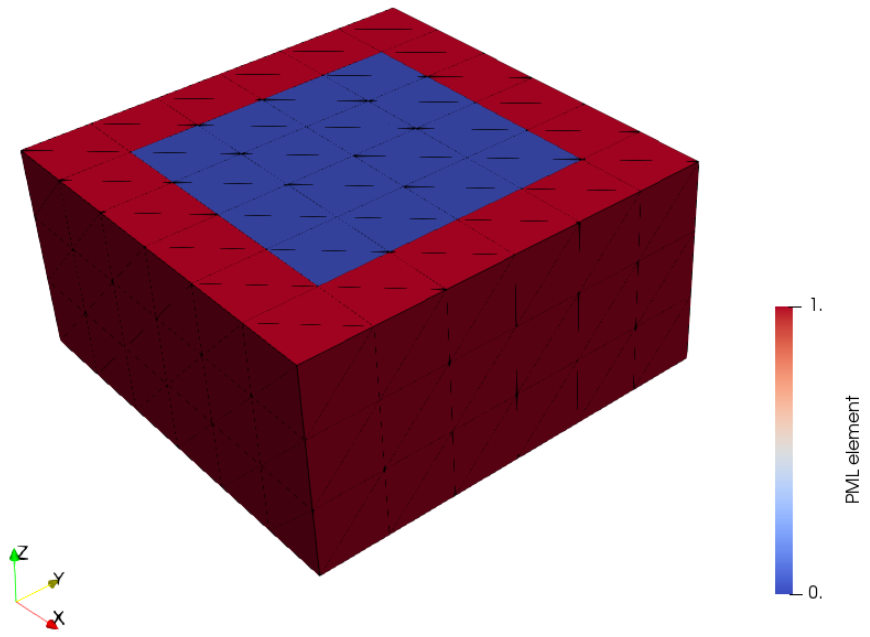

Figure 6.8: Mesh used in Example 2. Blue elements belong to the domain of interest, red elements belong to PML's.

of PML elements is added, the red elements in Figure 6.8. Finally, each hexahedron is split into a set of six tetrahedra. Thus, the computational mesh is composed of $7 \times 7 \times 4$ nodes (196 nodes, 648 tetrahedral elements). We paste $q = 300$ plane waves at each node, leading to 58,800 DOF. It is important to point out that using a standard FEM formulation with 6 elements per wavelength would result in a mesh of linear tetrahedra with approximately 630,000 DOF.

Figures 6.9(a) and 6.9(b) show the computed SPL field clipped at the plane $x = 0$ for uniform and non-uniform vertical profiles of the sound speed, respectively. Constructive and destructive patterns can be identified in the region $y \leq 0$ (the portion of domain above the sea bottom with $\tau = 0.1$), since the intensity of the reflected wave fronts is significant. On the contrary, the interference patterns are weaker in the region $y > 0$, above sea bottom with $\tau = 0.9$.

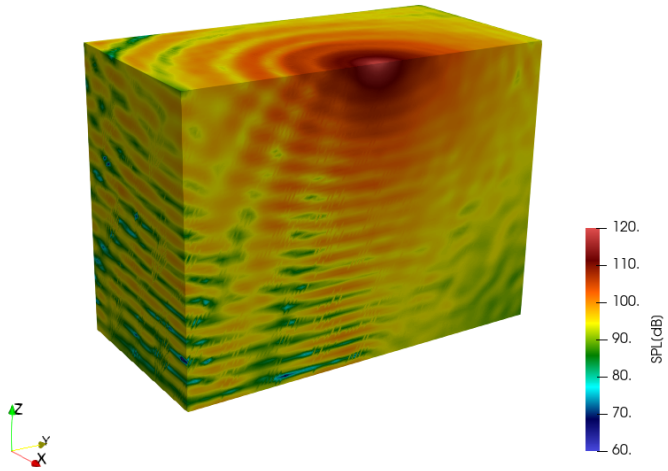

(a)

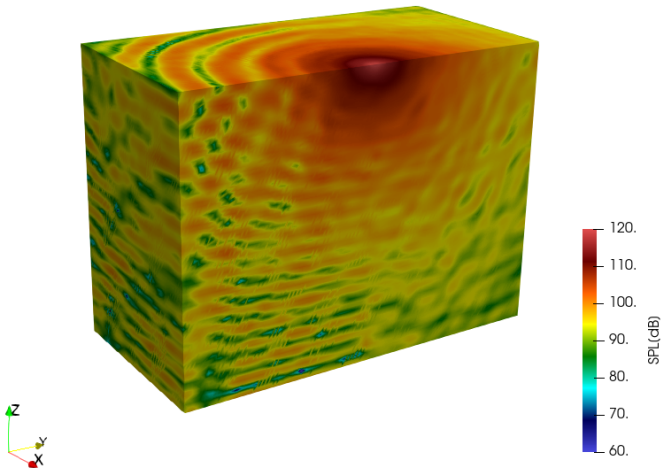

(b)

Figure 6.9: SPL field in Example 2, for $q = 300$. Case a) uniform sound speed $c = 1500$ m/s, case b) non-uniform sound speed, c decreases at a rate of -1 (m/s)/m. The plots are clipped at plane x=0.

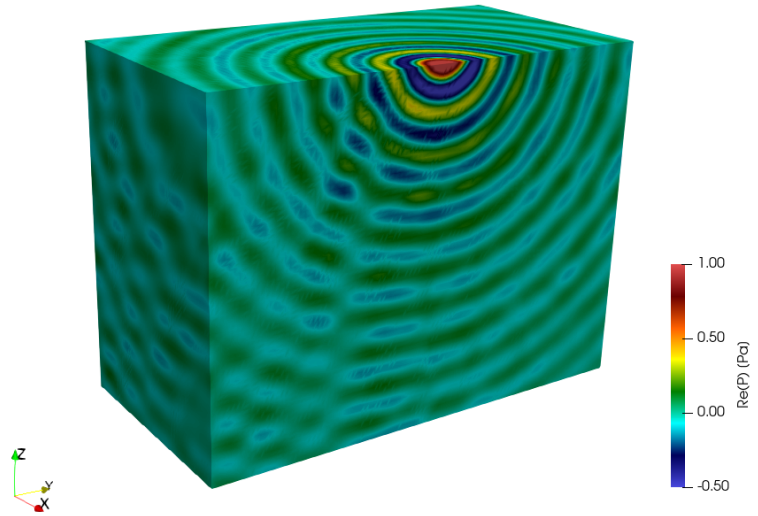

(a)

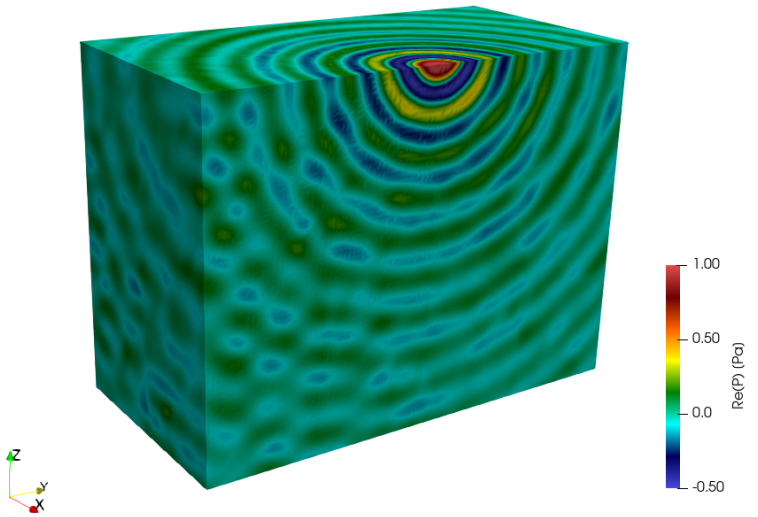

(b)

Figure 6.10: Real part of the pressure field in Example 2, for $q = 300$. Case a) uniform sound speed $c = 1500$ m/s, case b) non-uniform sound speed, c decreases at a rate of -1 (m/s)/m. The plots are clipped at plane x=0.

Figures 6.10(a) and 6.10(b) show the computed real part of the pressure field clipped at the plane $x = 0$ for uniform and non-uniform vertical profiles of the sound speed, respectively. In both figures, two regions with different wave patterns can be identified. First, for $y \leq 0$ (the portion of domain above the highly reflective sea bottom, $\tau = 0.1$) we can observe constructive and destructive interaction between the incident and reflected wave fronts (the seabed transmission coefficient is almost zero). On the contrary, for $y > 0$ (the portion of domain above the lowly reflective sea bottom, $\tau = 0.9$) we can observe the typical spherical wave spreading pattern since the reflected energy at the sea bottom is small (the seabed transmission coefficient is almost one).

6.4.3 Sound field generated by 2 point sources considering seawater absorption

This example shows the capabilities of the developed tool to simulate the 3D sound field generated by two sources. Similarly to the second example, the sea bottom is divided into two regions with different transmission coefficients. Similarly to the first example, two cases are considered. We first compute the solution for null seawater absorption $\alpha = 0$ dB/km, and then we compare it with the case of $\alpha = 100$ dB/km. In both cases, the sound speed is considered uniform, $c = 1500$ m/s. A PML is placed on the four lateral artificial boundaries of the domain, in order to simulate perfectly absorbing boundary conditions. These layers are characterized by a PML parameter $\sigma_{\text{PML,max}} = 25$ rad/s.

The domain of interest is the same as in the previous example: a rectangular cuboid $\Omega = [-36, 36] \times [-36, 36] \times [-54, 0]$ of seawater. The sea surface is considered as fully reflective ($\tau = 0$) again. The sea bottom is composed of two materials: a highly reflective seabed ($\tau = 0.2$) for $y \leq 0$ ('hard' material, high mismatch in the impedance), and lowly reflective seabed ($\tau = 0.8$) for $y > 0$ ('soft' material, low mismatch in the impedance). We use the same mesh as in the previous example. However, we set $q = 400$, leading to 78,400 DOF.

The example considers time-harmonic waves with a frequency of 250 Hz ($k = 1.05$ m^{-1}) generated by two identical noise sources located at $\mathbf{x_{s,1}} = [0, -18, \lambda/3]$ m and $\mathbf{x_{s,2}} = [0, -18, \lambda/3]$ m, where $\lambda = 6$ m is the wavelength. Similarly to the previous example, the noise source is placed slightly outside of the domain to avoid a singularity at the source point, see details in Section 4.2.4. The sources generate spherical waves

with pressure amplitude $p_{r_0} = 1$ Pa (117 dB) at a reference distance from the source of $r_0 = 1$ m.

Figures 6.11(a) and 6.11(b) show the computed SPL field clipped at the plane $x = 0$ for the case with null seawater absorption, $\alpha = 0$ dB/km, and the case with $\alpha = 100$ dB/km, respectively. Several aspects of the obtained results have to be highlighted. First, in both cases the constructive and destructive interaction patterns can be clearly identified, due to the presence of the overlapping radiating waves. Second, in both cases two patterns of the SPL field can be also identified. On the one hand, for $y \leq 0$ (the portion of domain above the highly reflective sea bottom, $\tau = 0.2$) we can observe an additional pattern of constructive and destructive interaction, between the incident and reflected wave fronts at the sea bottom. On the other hand, for $y > 0$ (the portion of domain above the lowly reflective sea bottom, $\tau = 0.8$) the interaction between incident and reflected waves is significantly smaller because the incident waves are mostly absorbed by the sea bottom. Finally, the positive seawater absorption produces a decrease in the SPL values as the distance from the sources increases. Therefore, the values of the SPL in Figure 6.11(b) are smaller than in Figure 6.11(a).

6.5 Concluding remarks

In this chapter we have successfully developed a new numerical tool to simulate the underwater noise propagation in three dimensions. Similarly to the 2D version of the tool, the hypothesis of time-harmonic solution is assumed and the Helmholtz equation governs the problem. Therefore, it inherits the ability of the 2D model to include most relevant physical phenomena, such as seawater absorption, and reflective surface and sea bottom.

The tool is based on the Partition of Unity Method enriched with plane waves. This allows using of much coarser meshes compared to the ones used when classical linear finite elements are used, reducing the number of degrees of freedom at the associated linear systems, and mitigating the pollution effect. To determine the 3D directions of the plane waves we select the algorithm proposed by Leopardi (2006). It divides the unit sphere into regions of equal area, and plane waves with similar directions of propagation are avoided. This improves the condition number of the system matrices and increases the accuracy of the simulation.

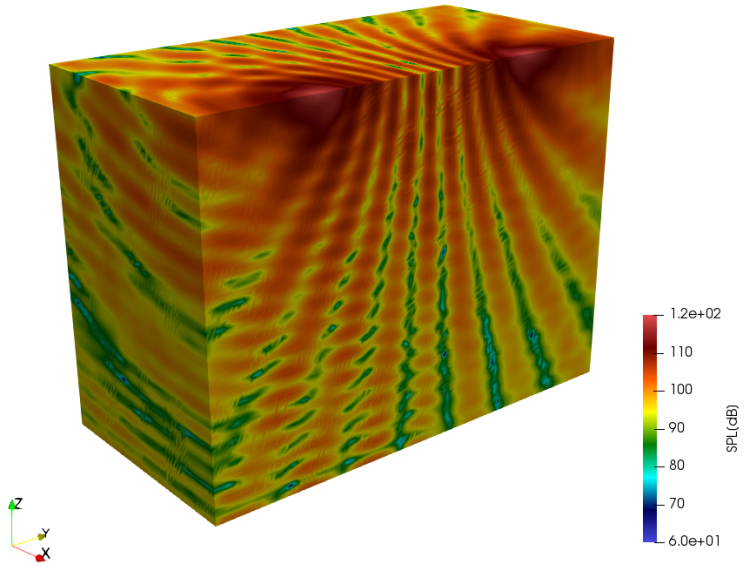

(a)

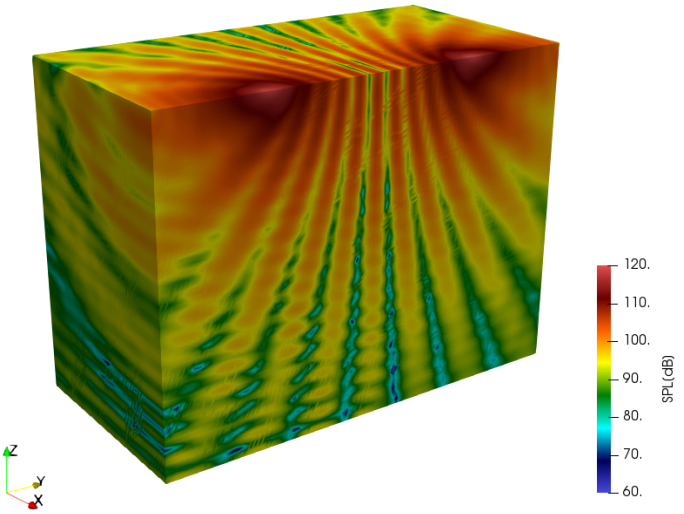

(b)

Figure 6.11: SPL field in Example 3, for $q = 400$. Case a) null absorption $\alpha = 0$ dB/km, case b) $\alpha = 100$ dB/km. The plots are clipped at plane x=0.

To increase the efficiency of the 3D tool, the elemental contributions to the system matrix have been computed according to the semi-analytical integration procedure for tetrahedra, presented in Chapter 5. Moreover, to further speed up the integration process, a two-step meshing strategy has been implemented. First, the domain is divided into a set of layers composed of hexahedral elements. The elements in the upper layers have to have the same shape and size. Second, each hexahedron is subdivided into six tetrahedra, leading to subsets of equal elements. This way, and if the sound speed is uniform along horizontal planes (the sound speed only varies along the vertical profile), the elemental matrices of each tetrahedron can be reused among all the tetrahedra of the same layer with the same shape and size.

Similar to the approach developed for the 2D tool, we have paid special attention to the boundary conditions prescribed over the lateral domain boundaries. In order to avoid spurious numerical reflections, artificial boundary conditions have been considered by means of Perfectly Matched Layers.

Finally, several examples have been presented to illustrate and assess the capabilities of the 3D simulation tool. The first example analyzes the q-convergence of the method in the case of a single traveling wave that propagates through media with and without seawater absorption. The accuracy of the solution improves with increasing the number of plain waves until it stagnates above q=400. This behavior is observed in both media. In the second example we have illustrated that the 3D tool is able to compute the SPL field generated by a single source in media both with uniform and non-uniform vertical sound speed profiles. In addition, the tool is able to consider the effect of seabeds with different transmission coefficients. In the last example, we showed that the numerical tool can simultaneously deal with several sound sources. Again, we have considered media with and without seawater absorption and seabed with different transmission coefficients. The results show that the simulation tool is able to capture the interference patterns between each of the generated pressure fields.

Chapter 7

Summary and future work

7.1 Summary

This thesis presents three main contributions. They are devised as steps towards a 3D numerical tool assessing the environmental impact of underwater noise, produced by multiple non-impulsive sources at medium and high frequencies (from hundreds of Hz to a few kHz). These contributions are summarized below:

1. **Development of a 2D version of the simulation tool**. After reviewing the most relevant aspects involved in the environmental underwater acoustics, see Chapter 2, and the currently available underwater noise propagation simulation techniques, see Chapter 3, a novel 2D model for simulating the sound propagation in an undersea domain has been successfully developed, see Chapter 4. The model includes the most relevant physical phenomena. The selection of the Helmholtz equation as governing equation automatically incorporates wave interference, reflection, refraction and diffraction. Seawater absorption has been modeled via the imaginary part of a complex wavenumber. To avoid numerical reflections at the lateral artificial boundaries, fully absorbing boundary conditions have been implemented using Perfectly Matched Layers.

   Helmholtz equation is solved using the Partition of the Unity Method enriched with plane waves. The fact that the plane waves contain *a priori* knowledge of the solution is crucial in order to mitigate the pollution effect and allows employing of coarser meshes with element size equal to several wavelengths. This

redounds to an increase in the accuracy of the solution and a significant saving in the computational costs. To improve the robustness of the numerical model, and thanks to the high uniformity degree of the meshes, we have developed a new procedure to reduce the condition number of the elemental and global matrices. It is based on the Singular Value Decomposition (SVD) technique in order to obtain a low-rank approximation of the local enrichment basis associated to the central node of a reference patch. This way, we have reduced the size of the global matrix while preserving the accuracy of the approximation. In the integration step, the enriching plane waves lead to highly oscillatory integrands. We have overcome this drawback by using a state-of-the-art semi-analytical rule for quadrilateral elements.

Several examples have been presented to illustrate and assess the capabilities of the 2D tool. They show it properly handles absorbing medium, sea bottom composed of different materials, non-planar sea bottom and multiple sources. This contribution is published in the ISI indexed journal *Computational Mechanics* Hospital-Bravo et al. (2016).

2. **Development of an efficient rule to integrate highly oscillatory functions over tetrahedra**. In Chapter 5, a novel semi-analytical rule for integrating high-oscillatory functions over tetrahedra elements is presented, by extending an existing approach for 2D integrals. The rule is devised to integrate functions that can be split into a non-oscillatory part and a complex exponential.

   The non-oscillatory part is approximated by Lagrange polynomials. The key point is to rewrite the three-dimensional integral as the summation of highly-oscillatory one-dimensional integrals, by properly splitting the resulting Lagrange monomials along the different spatial directions. The integration procedure states how to accurate and efficiently compute those 1D integrals.

   The scheme involves the calculation of computationally expensive integration weights but provides a large reduction in the number of integration points. As a result, significant reduction in the computational cost is obtained compared to conventional high-order Gauss-Legendre quadratures if at least one of the following conditions is met: *1.* the integrand oscillates more than 10 times in the integration domain; *2.* the evaluation of the integrand is particularly expensive;

3. integrals with the same oscillatory part must be evaluated multiple times. The latter is the exact case of the PUM enriched with plane waves and, thus, the rule becomes a pillar for the 3D version of the simulation tool, the third contribution.

We present several examples assessing the accuracy of the developed integration rule and its computational efficiency, compared to standard high-order Gauss-Legendre quadratures. In particular, we show that the new semi-analytical integration rule is successfully applied to compute the integrals involved in 3D sound propagation problems solved by using the PUM enriched with plane waves.

This contribution is published in the ISI indexed journal *International Journal for Numerical Methods in Engineering* Hospital-Bravo et al. (2017).

3. **Development of a 3D tool to simulate the undersea acoustic propagation**. A new version of the tool is produced that prevails over the specific challenges associated to the 3D simulation of underwater sound propagation. The tool is based on the same physical basis and a similar numerical approach as its 2D counterpart. Chapter 6 presents in detail its main ingredients. To determine the 3D plane wave directions of the enriched Partition of the Unity Method, we have followed the method proposed by Leopardi (2006) which improves the uniformity of the set of directions given by other approaches, and has no limitation in the number of plane waves per node.

   The tool discretizes the seawater domain using tetrahedral elements. In order to efficiently perform the integration of the highly-oscillatory functions that appear in the elemental matrices, we employ the semi-analytical rule presented in Chapter 5. To further increase the computational efficiency, a specific meshing approach has been developed, that allows reusing the elemental matrix of a given tetrahedron on other tetrahedra with the same shape and size, and with the same sound speed profile. Perfectly Matched Layers have been placed in the artificial lateral boundaries of the domain to avoid spurious numerical reflections.

   Finally, we have illustrated the capabilities of the 3D simulation tool by successfully applying it to several examples, including: absorbing and non-absorbing

seawater, uniform and non-uniform vertical profiles for the sound velocity, sea bottom composed of different materials, and multiple source points.

7.2 Research dissemination

We have published the three contributions summarized in the previous section in two indexed journals:

- R. Hospital-Bravo, J. Sarrate and P. Díez, Numerical modeling of undersea acoustics using a partition of unity method with plane waves enrichment, *Computational Mechanics*, May 2016, Volume 57, Issue 5, pp 717-732.

- R. Hospital-Bravo, J. Sarrate and P. Díez, A semi-analytical scheme for highly oscillatory integrals over tetrahedra, *International Journal for Numerical Methods in Engineering*, August 2017, Volume 111, Issue 8, pp 703-723.

The most relevant results obtained during this thesis have been presented in the following national and international conferences:

- R. Hospital-Bravo, J. Sarrate and P. Díez, Underwater sound propagation using the Generalized Finite Element Method (GFEM) applied to the Helmholtz equation. *Numerical Methods in Applied Sciences and Engineering*. Laboratori de Càlcul Numèric (UPC). Castelldefels, Spain. January 21-24, 2013.

- P. Díez, J. Sarrate and R. Hospital-Bravo, Assessing the subsea acoustic impact of offshore power stations using GFEM. *Advances in Computational Mechanics*. San Diego, California (USA). February 24-27, 2013.

- A. Moura, D. Lopes, E. Cruz, R. Hospital-Bravo, J. Sarrate and P. Díez, Integrated tool for the acoustic assessment and monitoring of marine activities and operations, *2nd International Conference and Exhibition on Underwater Acoustics*. Rhodes, Greece. June 22-27, 2014.

- R. Hospital-Bravo, J. Sarrate and P. Díez, Assessing the subsea acoustic impact of offshore power stations using GFEM, *11th World Congress on Computational Mechanics*. Barcelona, Spain. July 20-25, 2014.

- P. Díez, R. Hospital-Bravo and J. Sarrate, Modeling subsea acoustic impact of offshore power stations: assessment of the environmental impact, *3rd International Workshops on Advances in Computational Mechanics, IWACOM III*. Tokyo, Japan. October 12-14, 2015.

- J. Sarrate, R. Hospital-Bravo and P. Díez, A numerical model to assess the subsea acoustic impact of offshore power stations, *Congress on Numerical Methods in Engineering, CMN2017*. Valencia, Spain. July, 2017.

In addition, this research has also been presented in the following seminar:

- R. Hospital-Bravo, J. Sarrate and P. Díez, Numerical modeling of undersea acoustics using a partition of unity method with plane waves enrichment, *Computational Mechanics seminar*. Laboratori de Càlcul Numèric (UPC). October 2, 2015.

7.3 Future work

During the development of this thesis new questions have been posed leading to several extensions and new ideas that can be further investigated. Next, we discuss some of them and suggest some alternatives that could be explored in the near future.

1. **Input noise generation.** In our model, we introduce the input noise by integrating the independent term of the Robin condition over the boundary entities that belong to the set of elements near the noise source. This strategy increases the error in the regions near the surface, below the boundary entities where the Robin independent term is not integrated. We suggest to explore alternative ways of introducing the input noise, for instance, via the independent term of the Helmholtz equation, using a Dirac delta function.

2. **Plane wave directions.** In our implementation, we have set the plane wave directions at each node according to the algorithm proposed by Leopardi (2006). However, other spatial distributions can be used. We propose to analyze the influence of these distributions on the ill-conditioning of the elemental and global matrices, and the impact on the accuracy of the final result. For example, we

suggest the Coulumb Force Method in Peake et al. (2014), where the directions are obtained as the electrostatic equilibrium of a set charges over the unit sphere.

3. **PMLs with non-horizontal bottom.** The current implementation of the 3D tool requires that the elements located on the seabed and next to the PML boundaries have a planar bottom. To overcome this constraint, a geometrical artifact meeting the basic PML requirements (the physical properties of the medium must be uniform in the direction of the PML attenuation) should be developed.

4. **Integration strategies.** We have used a set of evenly spaced points in our implementation of the semi-analytical rule to interpolate the non-oscillatory part of the integrals. However, other distribution of points providing better interpolation properties could be analyzed. In addition, it could also be fruitful to compare the performance of the proposed rule against the promising integration methods presented in Gabard (2009) and Yang et al. (2018).

5. **Low-rank approximation of the reduced basis.** First, the low rank approximation developed for the 2D tool should be extended to the 3D case. Instead of 2D patches with quadrilateral shape, the approximation functions will be integrated over a convex polyhedron. Second, instead of a basis reduction posed at a nodal level, a procedure focused on an elemental level could be explored. The current approach is based on the integration of the approximation functions associated to a given node over the patch around it. We claim that the reduction in the condition number of the global system matrix can be improved by developing a criterion based on a low-rank approximation space at the element level, that considers the interaction between the approximation functions associated to the remaining nodes of the element. Thus, a better conditioning will be obtained with a lower computational cost (both in terms of CPU time and memory footprint) for the same accuracy.

6. **Iterative solvers.** Iterative solvers could be considered in order to increase the computational efficiency of the simulation tool. Even though the PUM reduces the global number of unknowns, the fact that each node is linked to multiple degrees of freedom leads to the assembly of large elemental matrices

that dramatically reduce the sparsity of the system matrix, compared to the sparsity associated to standard Finite Element approaches. Thus, the fill-in generated by direct solvers leads to large memory requirements, and the CPU time involved in the solver step may be prohibitive (specially if the full set of initial plane wave directions is considered). Therefore, the development of an iterative solver, adapted to the particular *a priori* structure of the system matrix, will improve the efficiency of the numerical method and reduce the CPU time demand.

7. **Error assessment and q-adaptivity.** The efficiency and the accuracy of the method could be improved by using an adaptive strategy. To this end, an *a posteriori* error estimation framework should be developed. From this error estimates, an adaptive process could be deduced to determine the optimal number q of planes waves to be pasted at each node (q-adaptivity).

8. **Benchmarking.** Other enriched methods have been recently developed, see 3.2.4.4. Although some of them are developed for other specific applications, it could be of interest to compare them with the method proposed in this thesis, in terms of performance and accuracy.

Appendix A

Estimation of the sound speed in seawater

The UNESCO equation provides an estimation of the value of the speed of sound c (m/s) through seawater, from the values of salinity S (in ppt), temperature T (in °C) and hydrostatic pressure p_h (in bars):

$$c(S,T,p_h) = C_w(T,p_h) + A(T,p_h)S + B(T,p_h)S^{3/2} + D(T,p_h)S^2, \tag{A.1}$$

where

$$\begin{aligned}
C_w(T,p_h) &= (C_{00} + C_{01}T + C_{02}T^2 + C_{03}T^3 + C_{04}T^4 + C_{05}T^5) + \\
&\quad (C_{10} + C_{11}T + C_{12}T^2 + C_{13}T^3 + C_{14}T^4)p_h + \\
&\quad (C_{20} + C_{21}T + C_{22}T^2 + C_{23}T^3 + C_{24}T^4)p_h^2 + \\
&\quad (C_{30} + C_{31}T + C_{32}T^2)p_h^3, \\
A(T,p_h) &= (A_{00} + A_{01}T + A_{02}T^2 + A_{03}T^3 + A_{04}T^4) + \\
&\quad (A_{10} + A_{11}T + A_{12}T^2 + A_{13}T^3 + A_{14}T^4)p_h + \\
&\quad (A_{20} + A_{21}T + A_{22}T^2 + A_{23}T^3)p_h^2 + \\
&\quad (A_{30} + A_{31}T + A_{32}T^2)p_h^3, \\
B(T,p_h) &= B_{00} + B_{01}T + (B_{10} + B_{11}T)p_h, \\
D(T,p_h) &= D_{00} + D_{10}p_h,
\end{aligned}$$

and the rest of the coefficients are given in Table A.1.

Table of Coefficients

Coefficients	Numerical values	Coefficients	Numerical values
C_{00}	1402.388	A_{02}	7.166E-5
C_{01}	5.03830	A_{03}	2.008E-6
C_{02}	-5.81090E-2	A_{04}	-3.21E-8
C_{03}	3.3432E-4	A_{10}	9.4742E-5
C_{04}	-1.47797E-6	A_{11}	-1.2583E-5
C_{05}	3.1419E-9	A_{12}	-6.4928E-8
C_{10}	0.153563	A_{13}	1.0515E-8
C_{11}	6.8999E-4	A_{14}	-2.0142E-10
C_{12}	-8.1829E-6	A_{20}	-3.9064E-7
C_{13}	1.3632E-7	A_{21}	9.1061E-9
C_{14}	-6.1260E-10	A_{22}	-1.6009E-10
C_{20}	3.1260E-5	A_{23}	7.994E-12
C_{21}	-1.7111E-6	A_{30}	1.100E-10
C_{22}	2.5986E-8	A_{31}	6.651E-12
C_{23}	-2.5353E-10	A_{32}	-3.391E-13
C_{24}	1.0415E-12	B_{00}	-1.922E-2
C_{30}	-9.7729E-9	B_{01}	-4.42E-5
C_{31}	3.8513E-10	B_{10}	7.3637E-5
C_{32}	-2.3654E-12	B_{11}	1.7950E-7
A_{00}	1.389	D_{00}	1.727E-3
A_{01}	-1.262E-2	D_{10}	-7.9836E-6

Table A.1: Coefficients of the UNESCO equation for estimating the sound speed in seawater.

In our model, the hydrostatic pressure p_h, in MPa, is obtained from the depth d, in meters, and the latitude ϕ, using the formula proposed in Leroy and Parthiot (1998):

$$p_h(d, \phi) = p_h(d, 45)\kappa(d, \phi) + \delta p_{h0}(d), \tag{A.2}$$

where

$$
\begin{aligned}
p_h(d,45) &= 1.00818\times10^{-2}d + 2.465\times10^{-8}d^2 - 1.25\times10^{-13}d^3 + 2.8\times10^{-19}d^4,\\
\kappa(d,\phi) &= \frac{g(\phi) - 2\times10^{-5}d}{9.80612 - 2\times10^{-5}d},\\
\delta p_{h0}(d) &= \frac{1.0\times10^{-2}d}{d+100} + 6.2\times10^{-6}d,
\end{aligned}
$$

being

$$g(\phi) = 9.7803(1 + 5.3\times10^{-3}\sin^2\phi).$$

Note that the value of the pressure obtained by evaluating Equation (A.2) must be converted from MPa to bars before entering into Equation (A.1).

Appendix B

Estimation of the boundary transmission coefficient

In this appendix we relate the transmission coefficient τ appearing in the Robin boundary condition (4.1) with several material properties of the surrounding media (air and sea bottom). According to Berkhoff (1976), the transmission coefficient can be written as:

$$\tau = \tau_1 + i\tau_2,$$

where $i = \sqrt{-1}$ is the imaginary unit,

$$\tau_1 = \frac{2K_r \sin\beta \cos\gamma}{1 + K_r^2 + 2K_r \cos\beta}$$

and

$$\tau_2 = \frac{(1 - K_r^2)\cos\gamma}{1 + K_r^2 + 2K_r \cos\beta},$$

being K_r the reflection coefficient, which is the ratio between the reflected and the incident wave amplitudes $K_r = |p_r|/|p_i|$, β the reflection phase angle, and γ the incident wave direction relative to the normal at the boundary.

The reflection phase angle β is set to zero, considering that the position of the numerical boundary agrees with its actual position. Thus, the complex transmission coefficient is purely imaginary. In addition, the incident wave direction γ cannot be unambiguously specified since the full-wave approach implies multiple reflections with different wave incident directions angles. In our model we conservatively assume

normal incidence ($\gamma = 0$). This is conservative in the sense that the produced noise level is going to be larger than the actual one. Thus,

$$\tau = i\,\frac{1 - K_r}{1 + K_r}. \tag{B.1}$$

The value of the transmission coefficient K_r can be obtained either from the value of the transmission loss at the interface TL_i, measured in dB, or from the acoustic impedance $Z_b = \rho_b c_b$ of the boundary, being ρ_b the density of the boundary material, depending on the availability of empirical measurements. In the first case, we have

$$K_r = 10^{-\mathrm{TL}_i/20}. \tag{B.2}$$

In the second case, assuming normal incidence, we have

$$K_r = \frac{Z_b/Z_{sw} - 1}{Z_b/Z_{sw} + 1}, \tag{B.3}$$

where $Z_{sw} \approx 1.54 \times 10^6$ kg/(m^{2}s) is the acoustic impedance of the seawater. Substituting Equation (B.2) and Equation (B.3) in Equation (B.1) we obtain expression (4.6) and (4.7), respectively.

Appendix C

Expansion of Lagrange polynomials into sets of monomials

This appendix details a procedure to compute the coefficients of the Lagrange polynomials decomposition into monomials. Our goal is to find the set of coefficients $\lambda_{d,\mathbf{a}}$ such that

$$L_d(\xi) = \sum_{|\mathbf{a}|\leq p} \lambda_{d,\mathbf{a}}\, \xi^a \eta^b \zeta^c, \qquad \text{for } d = 1, \ldots, n_p, \tag{C.1}$$

where $\mathbf{a} = (a, b, c)$, a, b, c being nonnegative integers and $|\mathbf{a}| := a + b + c \leq p$. Let

$$\mathbf{m}(\xi) = \begin{pmatrix} 1 \\ \xi \\ \eta \\ \vdots \\ \zeta^p \end{pmatrix} \quad \text{that corresponds to} \quad \begin{cases} \mathbf{a} = (0,0,0) \\ \mathbf{a} = (1,0,0) \\ \mathbf{a} = (0,1,0) \\ \vdots \\ \mathbf{a} = (0,0,p) \end{cases},$$

be the column vector containing the values of the n_p monomials at point ξ, and let

$$\mathbf{l}(\xi) = \begin{pmatrix} L_1(\xi) \\ L_2(\xi) \\ \vdots \\ L_{n_p}(\xi) \end{pmatrix}$$

be the column vector containing the values of the n_p Lagrange polynomials at point ξ. Therefore, the n_p equations in (C.1) can be written using a matrix notation as

$$\mathbf{l}(\xi) = \mathbf{\Lambda}\mathbf{m}(\xi), \tag{C.2}$$

where $\mathbf{\Lambda}$ is a square matrix collecting the $n_p \times n_p$ unknown coefficients $\Lambda_{(p,m(\mathbf{a}))} = \lambda_{p,\mathbf{a}}$, $m(\mathbf{a}) \in \{1, \ldots, n_p\}$ being a scalar that assigns a given order to each monomial with multi-index $\mathbf{a}$ satisfying $|\mathbf{a}| \leq p$.

Enforcing Equation (C.2) at the n_p interpolation points we have

$$\mathbf{L} = \mathbf{\Lambda}\mathbf{M},$$

where

$$\mathbf{L} = \begin{pmatrix} \vdots & & \vdots \\ \mathbf{l}(\xi_1) & \ldots & \mathbf{l}(\xi_{n_p}) \\ \vdots & & \vdots \end{pmatrix}, \quad \text{and} \quad \mathrm{M} = \begin{pmatrix} \vdots & & \vdots \\ \mathbf{m}(\xi_1) & \ldots & \mathbf{m}(\xi_{n_p}) \\ \vdots & & \vdots \end{pmatrix}$$

Taking into account that

$$L_n(\xi_d) = \begin{cases} 0 & \text{if } n \neq d \\ 1 & \text{if } n = d \end{cases} \quad \text{for } n, d = 1, \ldots, n_p,$$

we obtain

$$\mathrm{Id}_{n_p} = \mathbf{\Lambda}\mathbf{M},$$

where Id_{n_p} is the identity matrix of order n_p. Hence, matrix $\mathbf{\Lambda}$ can be obtained as

$$\mathbf{\Lambda} = \mathbf{M}^{-1}.$$

Note that matrix $\mathbf{\Lambda}$ only depends on the set of interpolation points that are defined on the reference element. Thus, it is evaluated once for a given set of integration points.

Finally, it is important to point out that Equation (C.2) allows writing the integration weights from Equation (5.9) in a compact vectorial notation:

$$\begin{aligned} \mathbf{w} &= \mathbf{\Lambda} \int_{\Omega^{\mathrm{ref}}} \mathbf{m}(\xi) \exp\left(i\mathbf{v} \cdot \mathbf{x}(\xi)\right) \, \mathrm{d}\xi \\ &= \mathbf{\Lambda} \exp\left(iD\right) \int_{\Omega^{\mathrm{ref}}} \mathbf{m}(\xi) \exp\left(iA\xi\right) \exp\left(iB\eta\right) \exp\left(iC\zeta\right) \, \mathrm{d}\xi. \end{aligned}$$

Appendix D

Integration of definite 1D highly oscillatory functions

The computation of highly oscillatory integrals over a tetrahedron using the proposed semi-analytical method involves the computation of a considerable number of 1D highly oscillatory integrals with the following form (Section 5.4):

$$I_{(0,1)} = \int_0^1 s^\nu \exp\left(i\mu s\right) \, \mathrm{d}s, \tag{D.1}$$

where ν is a nonnegative integer and and μ a complex coefficient.

There are several methods to compute these integrals, either analytical or numerical. The accuracy and computational efficiency of some of them depend on the combination of both parameters μ and ν. In this appendix we present a heuristic procedure to select a method for each combination of these parameters. Our objective is to reduce the CPU cost while keeping the relative error of these 1D integrals below 10^{-12}. This will allow us computing the integral over the tetrahedron with an acceptable accuracy.

Bakhvalov and Vasil'eva (1968) proposed an accurate and robust method to compute integral (D.1). It gives an analytical expression when the non-oscillatory part of the integral is a polynomial function, as in Equation (D.1), provided that at least $\nu + 1$ points are used. However, in 3D real simulations involving medium or high frequencies the computational cost of the method becomes too expensive due to the high number of evaluations of Bessel functions.

To overcome this shortcoming, we propose to use equations (5.12) and (5.13) for combinations of μ and ν that allows achieving the desired accuracy. Note that the most expensive function involved in these expressions is the factorial function of natural numbers, that in fact, are precomputed.

From our experience, for values of μ whose modulus are not close to 0, $|\mu| \nrightarrow 0$, the most efficient method in terms of CPU time is obtained by applying Equation (5.12):

$$\int_0^1 s^\nu \exp(i\mu s)\, \mathrm{d}s = \nu! \sum_{r=0}^{\nu} \frac{i^{r-1}(\exp(i\mu) - \lim_{s\to 0} s^{\nu-r})}{(\nu-r)!\mu^{r+1}}. \tag{D.2}$$

Unfortunately, expression (D.2) loses accuracy when the modulus of μ is small, $|\mu| \to 0$, as stated by Bettess et al. (2003); Sugimoto et al. (2003). In addition, we highlight that when using PUM in 3D applications the value of ν is much more higher than in 2D applications. Therefore, the modulus of each one of the addends in Equation (D.2) may differ by several orders of magnitude. This lead to inaccurate results because it implies the subtraction of similar terms whose modulus are much higher than the result of this operation. Therefore, the criterion for using Equation (D.2) depends on the combination of both values μ and ν. For this reason, we use Equation (D.2) when the following relations are satisfied:

$$\begin{aligned}
|\mu| &> \mathrm{tol}_1 \\
\frac{\nu!}{|\mu|^\nu} &> \mathrm{tol}_2 \\
\frac{|\mu|^\nu}{\nu!} &> \mathrm{tol}_3 \\
\frac{[(1-a)\nu]!}{|\mu|^{(1-a)\nu}} &> \mathrm{tol}_4 \\
\frac{[(1-a)\nu]!|\mu|^{a\nu}}{\nu!} &> \mathrm{tol}_5,
\end{aligned}$$

where $a \in [0,1]$. Based in our numerical experiments, we set $a = 0.6$ and $\mathrm{tol}_i = 10^{-1}$ for $i = 1, \ldots, 5$ in order to obtain the desired accuracy while reducing the CPU time.

When any of the earlier conditions is not satisfied, and at the same time the modulus of μ is moderate, $|\mu| < \mu_{\mathrm{th}}$, we apply Equation (5.13). Thus:

$$\int_0^1 s^\nu \exp(i\mu s)\, \mathrm{d}s = \sum_{r=0}^{r_{\max}} \frac{(i\mu)^r}{r!} \frac{(1 - \lim_{s\to 0} s^{\nu+r+1})}{\nu+r+1}\ . \tag{D.3}$$

As stated in Section 5.3, the value of $r_{\max}$ is adjusted so that the truncation error in the series is of the order of the machine accuracy ϵ. Our numerical experiments

show that the number of addends in the truncated series, $r_{\max}$, depends on the value of μ_{th}. Therefore, in order to limit it, and to reduce the computational cost of the integration step, we set $\mu_{\text{th}} = 4$.

When the values of μ and ν do not satisfy the conditions to use Equation (D.2) nor Equation (D.3), our implementation resorts to the method by Bakhvalov and Vasil'eva (1968) due to its accuracy and robustness. This method is more expensive from the computational point of view than the previous analytical methods, equations (D.2) and (D.3), but it provides more accurate results. Next we summarize the BV method for completeness, and we also detail an alternative expression to preserve the accuracy while reducing the CPU cost when the modulus of μ is small.

The BV method is based on an extension of the Gauss-Legendre rule to the highly oscillatory case. It is designed to compute efficiently the following type of definite integral:

$$I_{\text{BV}}(f, \Omega) = \int_{-1}^{+1} f(x) \exp(i\Omega x)\, \mathrm{d}x,$$

where $f(x)$ is a non-oscillatory (smooth) function. This function is approximated by a set of $n_L + 1$ Legendre polynomials:

$$f(x) \approx \sum_{d=0}^{n_L} c_d P_d(x), \tag{D.4}$$

where $P_d(x)$ is the Legendre polynomial of degree d in [-1,+1]. The coefficient c_d is obtained as

$$c_d = \left(\frac{2d+1}{2}\right) \sum_{m=0}^{\nu} w_m P_d(x_m) f(x_m),$$

where x_m and w_m are the m-th point and weight of the Gauss-Legendre quadrature of $(n_L + 1)$ points, respectively. Taking into account that

$$\int_{-1}^{+1} P_d(x) \exp(i\Omega x)\, dx = i^d \left(\frac{2\pi}{\Omega}\right) J_{d+1/2}(\Omega),$$

where $J_d(\Omega)$ is the Bessel function of the first kind and order d, we have

$$\int_{-1}^{+1} f(x) \exp(i\Omega x)\, \mathrm{d}x \approx \sum_{d=0}^{n_L} i^d (2d+1) \left(\frac{\pi}{2\Omega}\right)^{1/2} J_{d+1/2}(\Omega) \left(\sum_{m=0}^{n_L} w_m P_d(x_m) f(x_m)\right). \tag{D.5}$$

The main drawback of Equation (D.5) is that its accuracy is reduced when the value of Ω is small, $|\Omega| \to 0$. To mitigate this issue, we consider the Taylor expansion of

the Bessel function for small values of Ω. In this case we have

$$\frac{J_{d+1/2}(\Omega)}{\Omega^{1/2}} \approx \frac{1}{\Gamma(d+3/2)} \frac{\Omega^d}{2^{d+1/2}}, \tag{D.6}$$

where $\Gamma(\cdot)$ is the Gamma function. Note that in Equation (D.6) the Gamma function depends on a natural number. Therefore, their values can be precomputed, reducing the computational cost of Equation (D.5) when $|\Omega| \to 0$. Based on our experience we consider the threshold value $\Omega_{\text{th}} = 10^{-7}$.

In order to apply the BV method to compute Equation (D.1) we consider the transformation $s(x) = (x+1)/2$, giving

$$I_{(0,1)} = \frac{1}{2} \exp(i\mu/2)\, I_{\text{BV}}(s^\nu(x), \mu/2).$$

Finally, note that when $f(x)$ is a polynomial of degree n_L, the expansion in (D.4) is exact. Thus, the BV method with $n_L + 1$ points is analytical and provides the exact value of the integral up to round-off errors.

Appendix E

Semi-analytical rule for triangular elements

In Section 5.4.1, the analytical development of cases 1–11, $A \nrightarrow 0$, leads to Equation (5.16), which includes the following 2D integral

$$I_{\mathrm{TRI}} = \int_0^1 \int_0^{1-\zeta} \eta^b \zeta^c \exp\left(iB\eta\right) \exp\left(iC\zeta\right) \, \mathrm{d}\eta \, \mathrm{d}\zeta. \tag{E.1}$$

Bettess et al. (2003) developed a semi-analytical rule to compute this type of integrals. For the sake of consistency, we summarize it here detailing our implementation and preserving the notation used in our work. They identify 5 cases (Table E.1) depending on the values of B, C and $C - B$.

Table E.1: Possible combinations of the values of coefficients B and C in the semi-analytical rule for triangles, generating 5 special cases.

Case	B	C	$C - B$
1	$\nrightarrow 0$	$\nrightarrow 0$	$\nrightarrow 0$
2	$\nrightarrow 0$	$\nrightarrow 0$	$\rightarrow 0$
3	$\nrightarrow 0$	$\rightarrow 0$	—
4	$\rightarrow 0$	$\nrightarrow 0$	—
5	$\rightarrow 0$	$\rightarrow 0$	—

E.1 Cases from 1 to 3 ($B \nrightarrow 0$)

If $B \nrightarrow 0$, Equation (5.12) is introduced into Equation (E.1) leading to

$$I_{\mathrm{TRI}} = b!\left(\exp(iB) \sum_{u=0}^{b} \left(\frac{i^{u-1}}{(b-u)!B^{u+1}} \int_0^1 \zeta^c (1-\zeta)^{b-u} \exp(i(C-B)\zeta)\, \mathrm{d}\zeta \right) - \frac{i^{b-1}}{B^{b+1}} \int_0^1 \zeta^c \exp(iC\zeta)\, \mathrm{d}\zeta \right).$$

The binomial theorem, Equation (5.14), is used to develop the first integral. Then, we apply the procedure presented in Appendix D to the resulting expression, depending on the values of the resulting monomial exponents and $C-B$. Similarly, for the second integral we use the procedure detailed in Appendix D depending on the values of c and C.

E.2 Cases 4 and 5 ($B \to 0$)

If $B \to 0$, Equation (5.13) is introduced into Equation (E.1), leading to

$$I_{\mathrm{TRI}} \approx \sum_{u=0}^{u_{\max}} \frac{(iB)^u}{u!(b+u+1)} \int_0^1 \zeta^c (1-\zeta)^{b+u+1} \exp(iC\zeta)\, \mathrm{d}\zeta.$$

The binomial theorem, Equation (5.14), is used again to develop this integral. Then, the procedure presented in Appendix D is applied depending on the values of the monomial exponents and C.

Bibliography

Ainslie, M. A., C. A. F. de Jong, H. S. Dol, G. Blaquière, and C. Marasini (2009, February). Assessment of natural and anthropogenic sound sources and acoustic propagation in the North Sea. Technical Report TNO-DV 2009 C085, TNO, The Hague, Nederlands.

Ainslie, M. A. and J. G. McColm (1998). A simplified formula for viscous and chemical absorption in sea water. *The Journal of the Acoustical Society of America 103*(3), 1671–1672.

Anderson, E. and M. Pedersen (1956). Application of computer techniques to the prediction of underwater sound propagation. Technical report, DTIC Document.

Arapogianni, A., A. Genachte, R. M. Ochagavia, J. Vergara, C. Castell, A. R. Tsouroukdissian, J. Korbijn, N. Bolleman, F. Huera-Huarte, F. Schuon, et al. (2013, July). Deep water—the next step for offshore wind energy. *European Wind Energy Association (EWEA), Brussels, Belgium, ISBN*, 978–2.

Babuška, I., F. Ihlenburg, E. T. Paik, and S. A. Sauter (1995). A Generalized Finite Element Method for solving the Helmholtz equation in two dimensions with minimal pollution. *Computer Methods in Applied Mechanics and Engineering 128*, 325–359.

Babuška, I. and J. M. Melenk (1997). The partition of unity method. *International Journal for Numerical Methods in Engineering 40*(4), 727–758.

Babuška, I. M. and S. A. Sauter (1997). Is the pollution effect of the fem avoidable for the helmholtz equation considering high wave numbers? *SIAM Journal on Numerical Analysis 34*(6), 2392–2423.

Bakhvalov, N. S. and L. Vasil'eva (1968). Evaluation of the integrals of oscillating functions by interpolation at nodes of gaussian quadratures. *USSR Computational Mathematics and Mathematical Physics 8*(1), 241–249.

Berenger, J.-P. (1994). A perfectly matched layer for the absorption of electromagnetic waves. *Journal of Computational Physics 114*(2), 185–200.

Berkhoff, J. C. W. (1976, April). *Mathematical models for simple harmonic linear water waves. Wave diffraction and refraction.* PhD thesis, TU Delft, Delft, Nederlands.

Bettess, P., J. Shirron, O. Laghrouche, B. Peseux, R. Sugimoto, and J. Trevelyan (2003). A numerical integration scheme for special finite elements for the helmholtz equation. *International Journal for Numerical Methods in Engineering 56*(4), 531–552.

Boyles, C. A. (1984). *Acoustic waveguides: Applications to oceanic science.* John Wiley and Sons Inc., New York, NY.

Burdic, W. S. (1983). *Underwater Acoustic System Analysis.* Prentice-Hall signal processing series. London: Prentice-Hall, Inc.

Červenỳ, V., M. M. Popov, and I. Pšenčík (1982). Computation of wave fields in inhomogeneous media—gaussian beam approach. *Geophysical Journal International 70*(1), 109–128.

Cessenat, O. and B. Després (1998). Application of an ultra weak variational formulation of elliptic pdes to the two-dimensional helmholtz problem. *SIAM Journal on Numerical Analysis 35*(1), 255–299.

Chen, C. T. and F. J. Millero (1977). Speed of sound in seawater at high pressures. *The Journal of the Acoustical Society of America 62*(5), 1129–1135.

Collins, M. D. (1993). A split-step Padé solution for the parabolic equation method. *The Journal of the Acoustical Society of America 93*(4), 1736–1742.

Commission, O. (2008). Assessment of the environmental impact of offshore windfarms. Technical Report 385, OSPAR Commission, London, United Kingdom.

Cox, T. M., T. J. Ragen, A. J. Read, E. Vos, R. W. Baird, K. Balcomb, J. Barlow, J. Caldwell, T. Cranford, L. Crum, A. D'Amico, G. D'Spain, A. Fernández, J. Finneran, R. Gentry, W. Gerth, F. Gulland, J. Hildebrand, D. Houser, T. Hullar, P. D. Jepson, D. Ketten, C. D. Macleod, P. Miller, S. Moore, D. C. Mountain, D. Palka, P. Ponganis, S. Rommel, T. Rowles, B. Taylor, P. Tyack, D. Wartzok, R. Gisiner, J. Mead, and L. Benner (2006). Understanding the impacts of anthropogenic sound on beaked whales. *Journal of Cetacean Research and Management 7*(3), 177–187.

Davis, P. J. and P. Rabinowitz (1984). *Methods of numerical integration* (Second ed.)., Chapter 2.10.2, pp. 151–155. Computer Science and Applied Mathematics. San Diego, California, USA: Academic Press, Inc.

De Bel, E., P. Villon, and P. Bouillard (2005). Forced vibrations in the medium frequency range solved by a partition of unity method with local information. *International Journal for Numerical Methods in Engineering 62*(9), 1105–1126.

Dekeling, R. P. A., M. L. Tasker, M. A. Ainslie, M. Andersson, M. André, M. Castellote, J. F. Borsani, J. Dalen, T. Folegot, R. Leaper, A. Liebschner, J. Pajala, S. P. Robinson, P. Sigray, G. Sutton, F. Thomsen, A. J. Van der Graaf, S. Werner, D. Wittekind, and J. V. Young (2013, May). Monitoring Guidance for Underwater Noise in European Seas. *Second Report of the Technical Subgroup on Underwater Noise (TSG Noise)*.

Deraemaeker, A., I. Babuška, and P. Bouillard (1999). Dispersion and pollution of the fem solution for the helmholtz equation in one, two and three dimensions. *International Journal for Numerical Methods in Engineering 462*(4), 471–499.

Dompierre, J., P. Labbé, M.-G. Vallet, and R. Camarero (1999, August). How to subdivide pyramids, prisms, and hexahedra into tetrahedra. In *IMR*, École Polytechnique de Montréal, pp. 195–204.

Dufault, S. (2005, October). Assessment of the effects of underwater noise from the proposed Neptune LNG project. Report TA4200-3, LGL Limited and JASCO Research Limited.

Evans, G. and J. Webster (1999). A comparison of some methods for the evaluation of highly oscillatory integrals. *Journal of Computational and Applied Mathematics 112*(1—2), 55–69.

Farhat, C., I. Harari, and L. P. Franca (2001). The discontinuous enrichment method. *Computer Methods in Applied Mechanics and Engineering 190*(48), 6455–6479.

Farhat, C., I. Harari, and U. Hetmaniuk (2003). A discontinuous galerkin method with lagrange multipliers for the solution of helmholtz problems in the mid-frequency regime. *Computer Methods in Applied Mechanics and Engineering 192*(11), 1389–1419.

Farhat, C., R. Tezaur, and P. Weidemann-Goiran (2004). Higher-order extensions of a discontinuous galerkin method for mid-frequency helmholtz problems. *International Journal for Numerical Methods in Engineering 61*(11), 1938–1956.

Gabard, G. (2009). Exact integration of polynomial–exponential products with application to wave-based numerical methods. *Communications in Numerical Methods in Engineering 25*(3), 237–246.

Gerstoft, P. (2002, August). CABRILLO 1.0: Acoustic, elastic and poroelastic finite difference modelling. Technical report, Marine Physical Laboratory, University of California at San Diego, La Jolla CA-92093-0701 USA.

Graber, G., A. Rubin, and R. Seymour (1961). Underwater acoustic ray analysis. *The Journal of the Acoustical Society of America 33*(6), 840–840.

Gragg, R. (1985). The broadband normal mode model proteus. Technical report, DTIC Document.

Hazelwood, R. A. and J. Connelly (2005). Estimation of underwater noise – a simplified method. *International Journal of the Society for Underwater Technology 26*(3), 51–57.

Herrera, I. and F. J. Sabina (1978). Connectivity as an alternative to boundary integral equations: Construction of bases. *Proceedings of the National Academy of Sciences 75*(5), 2059–2063.

Hildebrand, J. (2004). Sources of anthropogenic sound in the marine environment. In *Report to the Policy on Sound and Marine Mammals: An International Workshop. US Marine Mammal Commission and Joint Nature Conservation Committee, UK. London, England*. Citeseer.

Hiptmair, R., A. Moiola, and I. Perugia (2011). Plane wave discontinuous galerkin methods for the 2d helmholtz equation: analysis of the p-version. *SIAM Journal on Numerical Analysis 49*(1), 264–284.

Hospital-Bravo, R., J. Sarrate, and P. Díez (2016). Numerical modeling of undersea acoustics using a partition of unity method with plane waves enrichment. *Computational Mechanics 57*(5), 717–732.

Hospital-Bravo, R., J. Sarrate, and P. Díez (2017). A semi-analytical scheme for highly oscillatory integrals over tetrahedra. *International Journal for Numerical Methods in Engineering 111*(8), 703–723.

Huttunen, T., J. P. Kaipio, and P. Monk (2004). The Perfectly Matched Layer for the Ultra Weak Variational Formulation of the 3D Helmholtz equation. *International Journal for Numerical Methods in Engineering 61*, 1072–1092.

Huttunen, T., P. Monk, and J. P. Kaipio (2002). Computational Aspects of the Ultra-Weak Variational Formulation. *Journal of Computational Physics 182*(1), 27–46.

Huybrechs, D. and S. Vandewalle (2006). On the evaluation of highly oscillatory integrals by analytic continuation. *SIAM Journal on Numerical Analysis 44*(3), 1026–1048.

Ihlenburg, F. (1998). *Finite Element Analysis of Acoustic Scattering* (1st ed.), Volume 132 of *Applied Mathematical Sciences*. New York: Springer-Verlag.

Isaacson, M. and S. Qu (1990). Waves in a harbour with partially reflecting boundaries. *Coastal Engineering 14*(3), 193–214.

Iserles, A. and S. P. Nørsett (2005). Efficient quadrature of highly oscillatory integrals using derivatives. *Proceedings of the Royal Society of London A: Mathematical, Physical and Engineering Sciences 461*(2057), 1383–1399.

Johnson, S. G. (2007). Notes on Perfectly Matched Layers (PMLs). Notes for MIT courses 18.369 and 18.336.

Kinsler, L. E., A. R. Frey, A. B. Coppens, and J. V. Sanders (1999). *Fundamentals of acoustics* (Fourth ed.). New York, USA: John Wiley & Sons.

Kuperman, W. A. and J. F. Lynch (2004). Shallow-Water Acoustics. *Physics Today 57*(10), 55–61.

Laghrouche, O. and P. Bettess (2000). Short wave modelling using special finite elements. *Journal of Computational Acoustics 8*(01), 189–210.

Laghrouche, O., P. Bettess, and R. J. Astley (2002). Modelling of short wave diffraction problems using approximating systems of plane waves. *International Journal for Numerical Methods in Engineering 54*, 1501–1533.

Laghrouche, O., P. Bettess, E. Perrey-Debain, and J. Trevelyan (2003). Plane wave basis finite-elements for wave scattering in three dimensions. *Communications in Numerical Methods in Engineering 19*, 715–723.

Laghrouche, O., P. Bettess, E. Perrey-Debain, and J. Trevelyan (2005). Wave interpolation finite elements for Helmholtz problems with jumps in the wave speed. *Computer Methods in Applied Mechanics and Engineering 194*, 367–381.

Leopardi, P. (2006). A partition of the unity sphere into regions of equal area and small diameter. *Electronic Transactions on Numerical Analysis 25*, 309–327.

Leroy, C. C. and F. Parthiot (1998). Depth-pressure relationships in the oceans and seas. *The Journal of the Acoustical Society of America 103*(3), 1346–1352.

Levinson, S. J., E. K. Westwood, R. A. Koch, S. K. Mitchell, and C. V. Sheppard (1995). An efficient and robust method for underwater acoustic normal-mode computations. *The Journal of the Acoustical Society of America 97*(3), 1576–1585.

Lichte, H. (1919). Uber den einfluss horizontaler temperaturschicht ung des seewasser s auf die reichweite von unterwasserschallsignalen. *Physikalische Zeitschrift 17*, 385–389.

Mahmood, M., O. Laghrouche, J. Trevelyan, and A. El Kacimi (2017). Implementation and computational aspects of a 3d elastic wave modelling by pufem. *Applied Mathematical Modelling 49*, 568–586.

Marine Mammal Commission (2007). The Marine Mammal Protection Act of 1972 as Amended.

Massimi, P., R. Tezaur, and C. Farhat (2008). A discontinuous enrichment method for three-dimensional multiscale harmonic wave propagation problems in multi-fluid and fluid–solid media. *International Journal for Numerical Methods in Engineering 76*(3), 400–425.

Mayer, P. and J. Mandel (1997). The finite ray element method for the Helmholtz equation of scattering: first numerical experiments. Technical report, University of Colorado at Denver, Denver, CO, USA.

McDonald, B. E. and W. A. Kuperman (1984). Time Domain Solution of Nonlinear Pulse Propagation. In L. B. Felsen (Ed.), *Hybrid Formulation of Wave Propagation and Scattering*, Volume 86 of *NATO Science Series*, Chapter 4, pp. 395–407. Springer Netherlands.

Melenk, J. M. (1995). *On generalized finite element methods*. Ph. D. thesis, The University of Maryland.

Melenk, J. M. and I. Babuška (1996). The partition of unity finite element method: Basic theory and applications. *Computer Methods in Applied Mechanics and Engineering 139*(1–4), 289 – 314.

Modesto, D., S. Zlotnik, and A. Huerta (2015). Proper generalized decomposition for parameterized helmholtz problems in heterogeneous and unbounded domains: application to harbor agitation. *Computer Methods in Applied Mechanics and Engineering 295*, 127–149.

National Research Council (2003). *Ocean Noise and Marine Mammals*. Washington DC, USA: The National Academies Press.

Nedwell, J. R., B. Edwards, A. W. H. Turnpenny, and J. Gordon (2004, September). Fish and marine mammal audiograms: a summary of available information. Technical Report 534R0214, Subacoustech Ltd, Hampshire, United Kingdom.

Nedwell, J. R., J. Langworthy, and D. Howell (2003, May). Assessment of sub-sea acoustic noise and vibration from offshore wind turbines and its impact on marine wildlife; initial measurements of underwater noise during construction of offshore windfarms, and comparison with background noise. Report 544 R 0424, COWRIE Ltd, United Kingdom.

Oliva-Elorza, D. (2005). *Room acoustics modeling using the raytracing method: implementation and evaluation*. Licentiate Thesis. University of Turku, Department of Physics.

Ortiz, P. (2004). Finite elements using a plane-wave basis for scatering of surface water waves. *Philosofical Transactions of the Royal Society A 362*, 525–540.

Ortiz, P. and E. Sanchez (2001). An improved partition of unity finite element model for diffraction problems. *International Journal for Numerical Methods in Engineering 50*(12), 2727–2740.

OSPAR Commission and others (2005). Convention for the protection of the marine environment of the north-east atlantic. In *Oslo-Paris Convention. London, UK*.

Peake, M., J. Trevelyan, and G. Coates (2014). The equal spacing of n points on a sphere with application to partition-of-unity wave diffraction problems. *Engineering Analysis with Boundary Elements 40*, 114–122.

Pekeris, C. L. (1948). Theory of propagation of explosive sound in shallow water. *Geological Society of America Memoirs 27*, 1–116.

Pekeris, C. L. and I. M. Longman (1958). Ray-theory solution of the problem of propagation of explosive sound in a layered liquid. *The Journal of the Acoustical Society of America 30*(4), 323–328.

Perrey-Debain, E., O. Laghrouche, P. Bettess, and J. Trevelyan (2004). Plane-wave basis finite elements and boundary elements for three-dimensional wave scattering. *Philosofical Transactions of the Royal Society A 362*(1816), 561–577.

Pierce, A. D. (1965). Extension of the Method of Normal Modes to Sound Propagation in an Almost-Stratified Medium. *The Journal of the Acoustical Society of America 37*(1), 19–27.

Porter, M. B. (1990). The time-marched fast-field program (FFP) for modeling acoustic pulse propagation. *The Journal of the Acoustical Society of America 87*(5), 2013–2023.

Porter, M. B. (1992). The kraken normal mode program. Technical report, DTIC Document.

Porter, M. B. and H. P. Bucker (1987). Gaussian beam tracing for computing ocean acoustic fields. *The Journal of the Acoustical Society of America 82*(4), 1349–1359.

Porter, M. B. and Y.-C. Liu (1994). Finite-Element Ray Tracing. In D. Lee and M. H. Schultz (Eds.), *Theoretical and Computational Acoustics*, Volume 2, pp. 947–956. International Conference on the Theoretical and Computational Acoustics: World Scientific Publishing Co.

Protocol, K. (1997). Kyoto protocol. *UNFCCC Website. Available online: http://unfccc. int/kyoto_protocol/items/2830. php (accessed on 1 January 2011)*.

Rappaport, C. M. (1995). Perfectly matched absorbing boundary conditions based on anisotropic lossy mapping of space. *IEEE Microw Guided Wave Letters 5*(3), 90–92.

Richardson, W. J., C. R. G. Jr., C. I. Malme, and D. H. Thomson (1995). *Marine Mammals and Noise*. Academic Press.

Rodriguez, O. C. (2008). General description of the bellhop ray tracing program. Technical report, Signal Processing Laboratory, Physics Department, Faculdade de Ciências e Tecnologia.

Simpson, S. D., A. N. Radford, S. L. Nedelec, M. C. Ferrari, D. P. Chivers, M. I. McCormick, and M. G. Meekan (2016). Anthropogenic noise increases fish mortality by predation. *Nature communications 7*(10544).

Southall, B. L., A. E. Bowles, W. T. Ellison, J. J. Finneran, R. L. Gentry, C. L. Greene Jr., D. Kastak, D. R. Ketten, J. H. Miller, P. E. Nachtigall, W. J. Richardson, J. A. Thomas, and P. L. Tyack (2007). Marine mammal noise exposure criteria: initial scientific recommendations. *Aquatic Mammals 33*(4), 411–521.

Strouboulis, T., I. Babuška, and R. Hidajat (2006). The generalized finite element method for Helmholtz equation: Theory, computation, and open problems. *Computer Methods in Applied Mechanics and Engineering 195*, 4711–4731.

Strouboulis, T. and R. Hidajat (2006). Partition of unity method for Helmholtz equation: q-convergence for plane waves and wave-band local bases. *Applications of Mathematics 51*(2), 181–204.

Strouboulis, T., R. Hidajat, and I. Babuška (2008). The generalized finite element method for Helmholtz equation. Part II: Effect of choice of handbook functions, error due to absorbing boundary conditions and its assessment. *Computer Methods in Applied Mechanics and Engineering 197*, 364–380.

Sugimoto, R., P. Bettess, and J. Trevelyan (2003). A numerical integration scheme for special quadrilateral finite elements for the helmholtz equation. *Communications in Numerical Methods in Engineering 19*(3), 233–245.

Svensson, P. and A. Krokstad (2008). *The early history of ray tracing in room acoustics*. Norwegian University of Science and Technology.

Tappert, F. D. (1977). *The parabolic approximation method*, Volume 70 of *Lecture Notes in Physics*, Chapter 5, pp. 224–287. Courant Institute of Mathematical Sciences, New York University: Springer.

Tezaur, R. and C. Farhat (2006). Three-dimensional discontinuous Galerkin elements with plane waves and Lagrange multipliers for the solution of mid-frequency

Helmholtz problems. *International Journal for Numerical Methods in Engineering 66*, 796–815.

Tezaur, R., I. Kalashnikova, and C. Farhat (2014). The Discontinuous Enrichment Method for medium-frequency Helmholtz problems with a spatially variable wavenumber. *Computer Methods in Applied Mechanics and Engineering 268*, 126–140.

The 92nd United States Congress (1972). Coastal Zone Management Act of 1972.

The European Commission (2008, June). Directive 2008/56/EC establishing a framework for community action in the field of marine environmental policy (Marine Strategy Framework Directive).

The European Commission (2009, April). Directive 2009/28/EC of the European Parliament and of the Council of 23 April 2009 on the promotion of the use of energy from renewable sources and amending and subsequently repealing Directives 2001/77/EC and 2003/30/EC. Official Journal of the European Union.

The European Commission (2010, September). Commission Decision of 1 September 2010 on criteria and methodological standards on good environmental status of marine waters. Official Journal of the European Union.

Thomsen, F. (2009). Assessment of the environmental impact of underwater noise. Technical Report 436, OSPAR Commission, London, United Kingdom.

Thomsen, F., K. Lüdemann, R. Kafemann, and W. Piper (2006, July). Effects of offshore wind farm noise on marine mammals and fish. Technical report, COWRIE Ltd.

United States Congress (2005, August). Energy policy act of 2005.

Urick, R. J. (1983). *Principles of Underwater Sound* (Third ed.). Los Altos, California: Peninsula Publishing.

Wang, D., R. Tezaur, J. Toivanen, and C. Farhat (2012). Overview of the Discontinuous Enrichment Method, the Ultra-Weak Variational Formulation, and the Partition of Unity Method for acoustic scattering in the medium frequency regime and performance comparisons. *International Journal for Numerical Methods in Engineering 89*, 403–417.

Wenz, G. M. (1962). Acoustic ambient noise in the ocean: spectra and sources. *The Journal of the Acoustical Society of America 34*(12), 1936–1956.

Westwood, E. K., C. Tindle, and N. Chapman (1996). A normal mode model for acousto-elastic ocean environments. *The Journal of the Acoustical Society of America 100*(6), 3631–3645.

Williams, R., A. J. Wright, E. Ashe, L. Blight, R. Bruintjes, R. Canessa, C. Clark, S. Cullis-Suzuki, D. Dakin, C. Erbe, et al. (2015). Impacts of anthropogenic noise on marine life: Publication patterns, new discoveries, and future directions in research and management. *Ocean & Coastal Management 115*, 17–24.

Wong, G. S. K. and S. Zhu (1995). Speed of sound in seawater as a function of salinity, temperature, and pressure. *The Journal of the Acoustical Society of America 97*(3), 1732–1736.

Yang, M., E. Perrey-Debain, and J.-D. Chazot (2015). Development of the partition of unity finite element method for the 3D analysis of interior sound fields. In *EuroNoise 2015*, pp. 1161–1165. EAA-NAG-ABAV.

Yang, M., E. Perrey-Debain, B. Nennig, and J.-D. Chazot (2018). Development of 3d pufem with linear tetrahedral elements for the simulation of acoustic waves in enclosed cavities. *Computer Methods in Applied Mechanics and Engineering 335*, 403–418.

Zykov, M., M.-N. R. Matthews, and N. E. Chorney (2013, March). Underwater Noise Assessment. Technical report, Central Coastal California Seismic Imaging Project, JASCO Applied Sciences, Suite 202, 32 Troop Ave., Dartmouth, NS, B3B 1Z1, Canada.